ABSTRACT

Title of dissertation: THE DYNAMICS OF PLUNGING BREAKERS AND THE GENERATION OF SPRAY DROPLETS

Martin A. Erinin
Doctor of Philosophy, 2020

Dissertation directed by: Professor James H. Duncan
Department of Mechanical Engineering

In this dissertation, drop generation by plunging breaking waves is studied in laboratory-scale experiments. The breaking waves are generated by a programmable wavemaker that is set to produce a dispersively focused wave packet. Breaker profile and drop measurements are obtained for three breaking waves of increasing intensity, called herein the, weak, moderate, and strong plunging breakers, respectively. Drops, with radius ≥ 50 μm, are measured using a cinematic in-line holographic system positioned at 28 streamwise measurement locations, arranged in a horizontal plane, called herein the measurement plane, positioned 1 cm above the maximum wave crest height, during many repeated breaking events. From the holograms, the radius, three-dimensional location, and velocity of the drops is determined. The evolution of the breaker profile is measured at the center plane of the tank using a cinematic laser-induced fluorescence (LIF) technique. Drop and breaker profile movies are taken simultaneously and recorded at 650 frames per second.

The breaker profile and drop measurements from the weak breaker are used to identify and quantify spray generation processes in plunging breakers. Two spatially

and temporally separated regions of drop production are found. The first region (I) of drop production is associated with the active phase of wave breaking and begins with jet impact. In this region, drops are produced by jet impact, large bubble bursting events, and splashing. The second region (II) of drop production occurs after the active phase of wave breaking, approximately one wave period after jet impact. In this region, drops are generated by small air bubbles, initially entrained by the breaker, that rise to the free-surface and burst.

Various features of the breaker profiles and drop production are compared and contrasted between the three waves. The temporal evolution of the breaker profile is measured in 10 unique realizations for each of the three breakers. At every instant in time, the phase averaged mean breaker profile and the distribution of standard deviation (SD) in breaker height along the streamwise direction of the mean profile is computed. Using the mean profiles, the three breakers are physically characterized based on their wave crest and jet impact speed. When aligned to the plunging jet impact location in space and time, the breaker profiles are found to be highly repeatable throughout the non-linear wave breaking process. Profile regions with high SD in height correspond to regions of high drop production. The number of drops generated per breaking event is found to scale exponentially with jet impact speed. The drop probability distribution from each of the three waves follows a power law scaling where large and small drop regions obey power laws with different coefficients.

THE DYNAMICS OF PLUNGING BREAKERS AND THE GENERATION OF SPRAY DROPLETS

by

Martin A. Erinin

Dissertation submitted to the Faculty of the Graduate School of the
University of Maryland, College Park in partial fulfillment
of the requirements for the degree of
Doctor of Philosophy
2020

Advisory Committee:
Professor James H. Duncan, Chair/Advisor
Professor Kenneth Kiger
Associate Professor Johan Larsson
Emeritus Professor Peter Bernard
Associate Professor Anya Jones, Dean's Representative

Acknowledgments

This section is dedicated to the people who helped me throughout my PhD. First and foremost, I would like to thank my advisor, Professor James Duncan, for giving me the opportunity to pursuit a PhD and being a great mentor. You are truly the embodiment of a rigorous scientist, the lessons I have learned from you will be with me for the rest of my life.

I would also like to thank my lab mates and Professor Liu from whom I have learned much from and without whom I would not have been able to achieve nearly as much in my academic career. To Nate, Naeem, and An, who have taught me how to get around the lab from the early days when I was an undergraduate, I would like to give my sincerest gratitude.

I also want to thank all the undergraduates who have worked with me over the years. It has been a pleasure to work with you such young and talented people and I wish you all success in the future. I would especially like to thank Benjamin Schaefer for helping me with the tedious task of processing countless wave surface profiles during the last few months of my PhD.

Thank you to my committee members, Professor Kiger, Professor Larsson, Professor Bernard, and Professor Jones for generously giving their time, attention, and insightful comments on this dissertation.

Last but not least, I would like to thank my close family and friends. The love, care, and support I have received from you has made this journey easier.

Contents

List of Tables

List of Figures

Chapter 1: Introduction

1.1 Background and Motivation

Sea spray consists of water drops that are typically generated by breaking wind water waves. The transfer of mass, momentum, and heat between the ocean and the atmosphere is greatly influenced by sea spray [Veron, 2015, Wu, 1973, Veron et al., 2012, O'Dowd and de Leeuw, 2007, Andreas, 2011, Bao et al., 2011, Bianco et al., 2011, Mueller and Veron, 2014a,b, Anguelova et al., 1999a, Koga, 1981]. Sea spray has the potential to dramatically increase the intensity of tropical cyclones, see Andreas and Emanuel [2001] and Wang et al. [2001]. Sea spray is also known to enhance some chemical reactions that occur near the air-sea interface. Finally, sea spray aerosol can act as reactive medium in the atmosphere, transforming chemical reactions [Blanchard and Syzdek, 1972, Ravishankara, 1997].

Extensive efforts have been devoted to studying drop generation by breaking waves. Previous investigations have reported measurements of the temporally averaged droplet size distributions and fluxes at fixed heights in wind-wave systems at sea and in laboratory-scale experiments. It is commonly accepted that droplets are primarily produced by three breaking subprocesses: wind shear (primarily at the wave crest), splashing, and the popping of breaker-entrained air bubbles that rise

to the free surface [Veron, 2015]. However, there is little experimental data that quantitatively link the relationship between breaking events and droplet production by these subprocesses.

1.2 Overview of Previous Research

Comprehensive reviews of spray generated by breaking waves have been published recently by Veron [2015] and de Leeuw et al. [2011]. According to the review article by Veron [2015] there are two dominant mechanism by which drops are generated by a breaking wave. The first drop production mechanism is by bubbles, initially entrained by the breaking wave, rising to the free surface and bursting. When a bubble bursts it creates two types of drops, film drops, generated by the rupturing of the bubble film, and jet drops, formed by the collapse of the bubble cavity. The second primary mechanism of drop production identified by Veron [2015] is when the wind shear stress is sufficiently large to tear off globules of water from the wave crest. Both of these drop generation mechanisms are shown in an artistic rendering in Veron [2015]'s Figure 1, which is reproduced here as Figure 1.1. Recent studies have been carried out in the field (see for example, Monahan et al. [1986], Wu et al. [1984], de Leeuw [1986], Smith et al. [1993], and Reid et al. [2001]) and in the lab (see for example, Wu [1973] and Veron et al. [2012]), which are discussed in more detail in the sections below. In these studies drop production is parameterized with wind speed rather than the sea state characteristics. It should be noted that our knowledge of the relationship between breaking events and drop production is

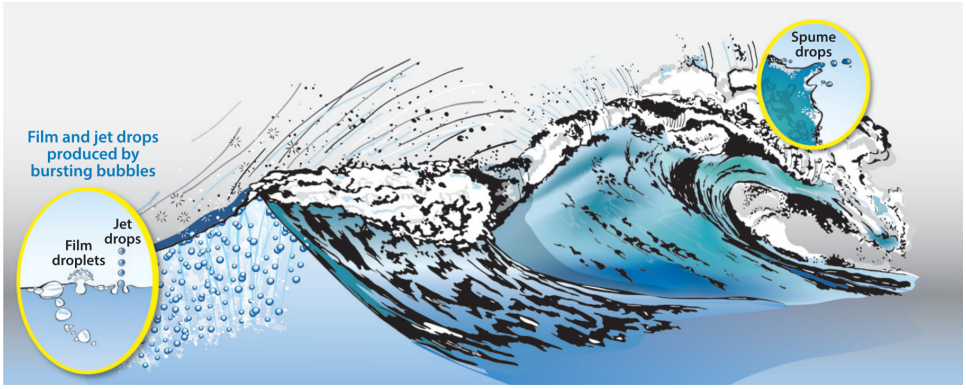

Figure 1.1: Drop production mechanisms as envisioned by an artist in Veron [2015] (originally Figure 1 in that review article). Spume drops, which are globules of water sheared off from the wave crest, can be seen on the top right of the image. Entrained bubbles can be seen behind the wave crest as they rise to the free surface and pop, creating film and jet drops.

still quite limited [Veron, 2015, de Leeuw et al., 2011].

In an effort to study the relationship between breaking and drop production, some investigators have explored drop production by bubble bursting. As mentioned previously, when a bubble bursts two types of drops are produced, film drops, which tend to be relatively small (drop radius r between 0.01 μm and 5 μm) and jet drops, which can be considerably larger, $r \approxeq 400$ μm [Veron, 2015, Andreas, 1998]. One of the earliest photographic measurements on the jet drops were described in Kientzler et al. [1954]. Other notable works on bubble popping include Spiel [1995, 1998], Resch [1986], Resch and Afeti [1991] and Cipriano and Blanchard [1981]. Recently, the size and ejection speed of jet drops as a function of the bubble radius have been extensively studied by a number of investigators using theory and numerical simulation (see Gañán Calvo [2017], Deike et al. [2018] and Brasz et al. [2018]).

These recent studies have attempted to establish some universal scaling laws for drops produced by bursting bubbles. Additionally, the role of surfactants have been studied in laboratory experiments by Sellegri et al. [2006] where the effects of surfactants (sodium dodecyl sulphate, SDS) on the production of sub-micron marine aerosols by bubble bursting were investigated. The authors showed that in the presence of SDS, the size distribution of drops shifts toward smaller sizes and the relative importance of larger drops increases dramatically. In a laboratory breaking wave analog, Modini et al. [2013] and Callaghan et al. [2014] demonstrated the effects of soluble surfactants on the persistence of bubbles and the production of aerosol particles upon bursting in salt water.

Many of the above-mentioned studies were conducted under ideal conditions with a calm free surface and single bubbles, which is presumably different from the surface conditions found in a breaking wave. In plunging breakers, the surface experiences a dramatic topographical change as the jet is formed at the wave crest and plunges onto the front of the wave face. A large pocket of air is trapped during a breaking event as the jet impact takes place. Additionally, after jet impact there is more air entrainment due to the violent splash of the free surface caused by the jet impact. Both laboratory experiments by Lamarre and Melville [1991], Deane and Stokes [2002] and numerical simulations by Deike et al. [2016], Lubin and Glockner [2015] have shown that the total volume of air entrained and the size distribution of bubbles can be physically scaled to the energy dissipated due to breaking and to the characteristic wave slope at breaking.

Various studies have shown that salt and surfactants strongly affect the pro-

duction of drops by bursting bubbles. However, the precise connections between surfactant concentration, water salinity, and drop production is poorly understood. At moderate wind speeds, air entrainment and drop production are probably associated with whitecaps. However, our knowledge of the relationship between breaking events and drop production is limited, Veron [2015] and de Leeuw et al. [2011]. The processes of drop generation by breaking waves are also modified by the wind. At high wind speeds, spume drops are produced as foam is ripped off the wave crests by the wind. At moderate wind speeds, air entrainment and drop production are probably associated with whitecaps.

A number of studies have attempted to model the drop production in the ocean. A model accounting for the variation of the drop production rate with wind speed was first proposed by Monahan et al. [1986]. In this time-dependent model the aerosol population is modeled in the open-ocean in terms of the drop radius. The model accounts for aerosol production coming from the bursting of bubbles from whitecaps at moderate wind speed close to the water surface. A number of refinements to this model have been proposed, first by de Leeuw [1986] who modeled the distribution of particle sizes in the region from the free surface to a height of 11 m. Wu [1990] combined data and models from previous researchers and found that drop concentration increases exponentially with wind velocity. Additional refinements to Monahan et al. [1986]'s model were proposed by Andreas [1992] and Andreas et al. [1995]. Despite the extensive efforts to model the sea spray in the ocean, a review by Andreas [1998] points out that estimates of the production rate of drops can vary over six orders of magnitude.

1.2.1 Review of Some Laboratory and Field Experiments on Drop Generation

A number of laboratory and field experiments have attempted to investigate the relationship between wave breaking and sea spray generation. Some of these studies were summarized briefly in this paragraph, while a few selected studies are reported in the preceding two paragraphs. Lai and Shemdin [1974] measured the wave height distribution and the vertical distribution of spray in a wind-wave tank. Monahan et al. [1982, 1983] correlated the decay of whitecaps with the number of drops in both a laboratory tank and the field. Koga [1981, 1984] measured the vertical distribution and velocity (along the wave profile) of giant drops (diameter $>$ 0.81 mm) produced directly from breaking wind waves. Anguelova et al. [1999b] and Veron et al. [2012] measured spume drops, which are generated by wind tearing, in the laboratory while Fairall et al. [2009] investigated large spume drops production by breaking wind waves in laboratory. Stokes et al. [2013] built a reference tank system as a breaking wave analogue to study the production of foam and sea-spray aerosols. Near-surface measurements of sea-spray aerosol production by individual breaking wave events in the open ocean have been given by Norris et al. [2013]. In this work, an aerosol spectrometer probe was placed approximately 1 m above the breaker whitecaps.

Wu [1973] used a laser and a photoresistor to measure drop size distribution in a laboratory wind wave tank. The measurements were taken at three wind speeds ($U = 10.72$ m/s, 12.62 m/s, 13.43 m/s) and two heights above the water surface. One

of his primary results are shown in Figure 1.2 where he shows the drop diameter distributions at the different wind speeds and different heights above the water surface. Wu [1973] observed a power-law relationship in the drop size distribution and a notable difference in the slope between the small and large drops occurring at a drop of diameter $D > 200$ μm.

Wu et al. [1984] conducted field measurements using a similar measurement technique described in the previous paragraph (from Wu [1973]). Drop size distribution data was collected at different wind speeds and at different height above the water surface. Figure 1.3 shows two drop size distributions, the left subplot shows data at three wind speeds ($U = 6.4$ m/s, 7.5 m/s, 8.0 m/s) while the right subplot shows data at the same wind speed ($U_0 = 7.5$ m/s) at two different heights, $z =$ 13 cm and 18 cm. Again, Wu et al. [1984] observed a power-law relationship in the distribution of drop sizes and a significant change in slope between large and small drops occurring between 200 μm $< D <$ 400 μm.

Veron et al. [2012] conducted experiments in a wind-wave tank at high wind speeds (up to $U = 47.1$ m/s) to obtain spume drop size distributions and compared his results to modern spray distribution models by Mueller and Veron [2009] and Fairall et al. [1995]. He used a shadowgraph technique to image drops (with $D > 140$ μm) and measured their radius using image processing techniques. Figure 1.4 shows the spume drop size distributions at three different wind speeds ($U =$ 31.3 m/s, 41.2 m/s, 47.1 m/s). Similar to the lab and field experiments of Wu [1973] and Wu et al. [1984], a power-law relationship is apparent in the drop size distribution with a difference in slope between large and small drops with a break

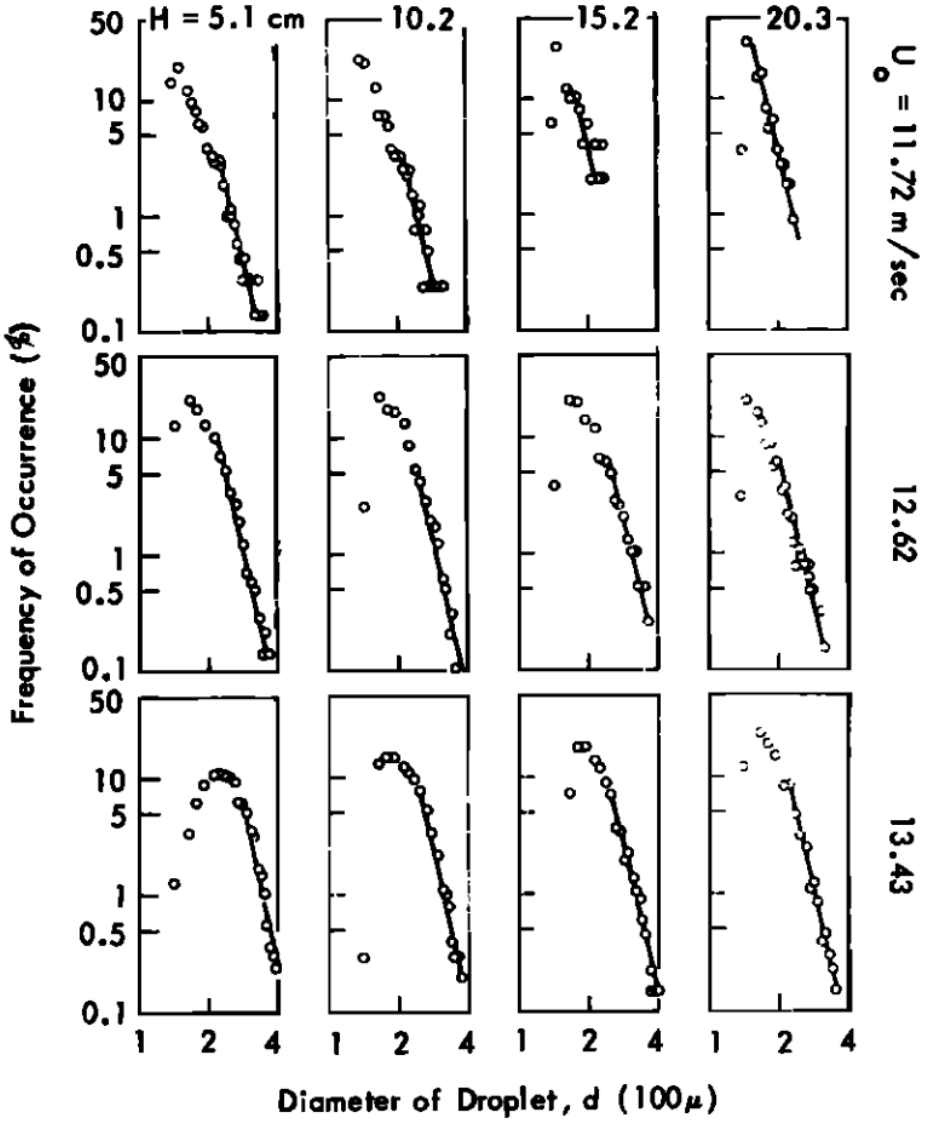

Figure 1.2: Drop size distributions from laboratory generated wind-waves at various wind speeds (vertical plots) and height above water surface (horizontal plots) from Wu [1973].

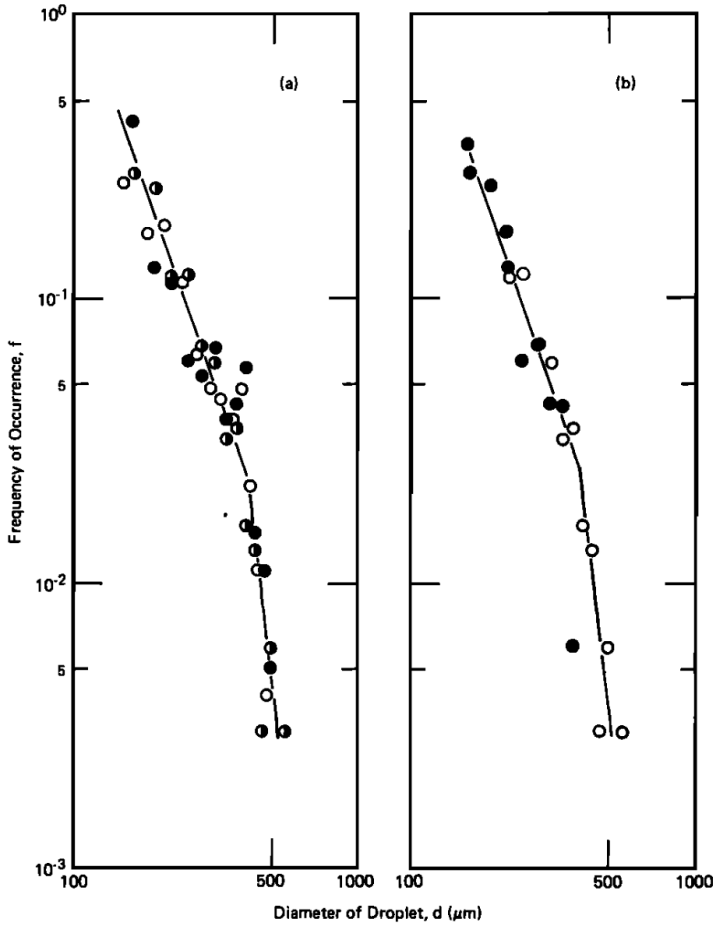

Figure 1.3: Drop size distributions 13 cm above the water surface at various wind speeds (left plot, where $U = 6.4$ m/s (open circles), $U = 7.5$ m/s (filled circles), $U = 8.0$ m/s (solid circles)) and at the same wind speed ($U = 7.5$ m/s) but different height above water surface($z = 13$ cm (open circles) and $z = 18$ cm (solid circles)) from Wu et al. [1984].

in slope around $D = 1000$ μm.

1.2.2 Review of Recent Numerical Simulations of Bubbles and Drop Generated by Breaking Waves

Numerical simulations of drops generated by breaking waves have recently become available through improvements in numerical schemes and increases in computational capacity. By using a high resolution simulation, Wang et al. [2016] investigated the bubbles and drops generated by plunging breakers using a direct numerical simulation (DNS). Figure 1.5 shows a side view of a breaking wave from Wang et al. [2016] just after the jet impact, where the air-water interface is identified by the blue colored isosurface . A tube of entrained air can be seen in the middle of image, while bubbles are seen below the free surface and drops are seen above the air-water interface. A power law scaling is measured for the large drops with a slope of -4.5. It should be noted that these simulations do not resolve small drops, therefore the difference in power law scaling found in field measurements and experiments is not observed in the DNS.

Deike et al. [2016] studied bubble entrainment during wave breaking using direct numerical simulations. For bubbles smaller than the Hinze scale, they developed an improved scaling model for the bubble size distributions which is given by:

$$N(r,t) = B(V_0/2\pi)(\epsilon(t-\Delta\tau)Wg)r^{-10/3}r_m^{-2/3}$$

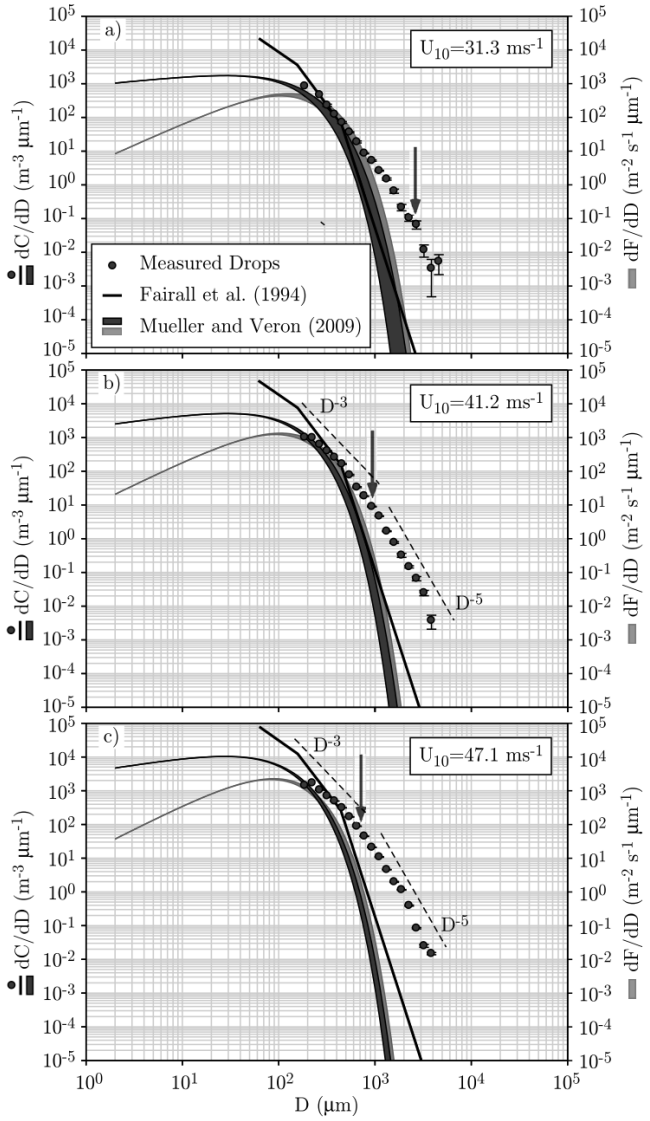

Figure 1.4: Spume drop size distributions from laboratory generated wind-waves at various wind speeds (U = 31.3 m/s, 41.2 m/s, 47.1 m/s, solid black dots) from Veron et al. [2012] plotted along with models from Fairall et al. [1995] and Mueller and Veron [2009] also shown.

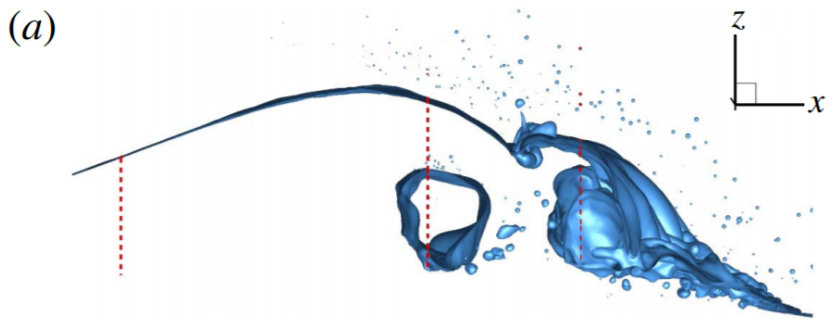

Figure 1.5: A side view of a numerical simulation from Wang et al. [2016] of a breaking wave just after jet impact. An air cavity and bubbles are present below the free surface, while drops can be seen suspended up above.

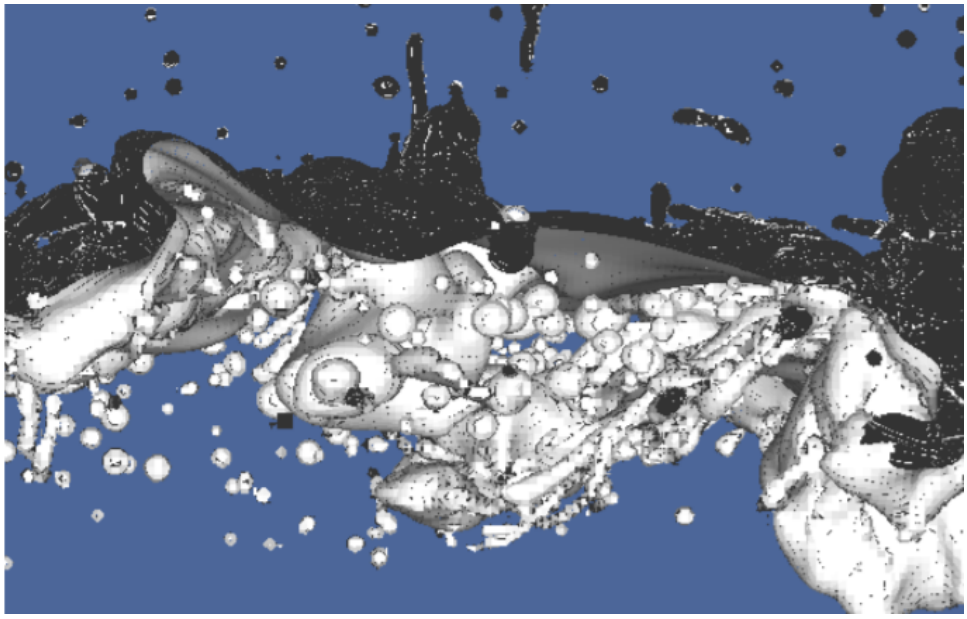

Figure 1.6: A visualization of the air-water interface from direct numerical simulations just after wave breaking from Deike et al. [2016]. Numerous drops and bubbles are visible in the water and air.

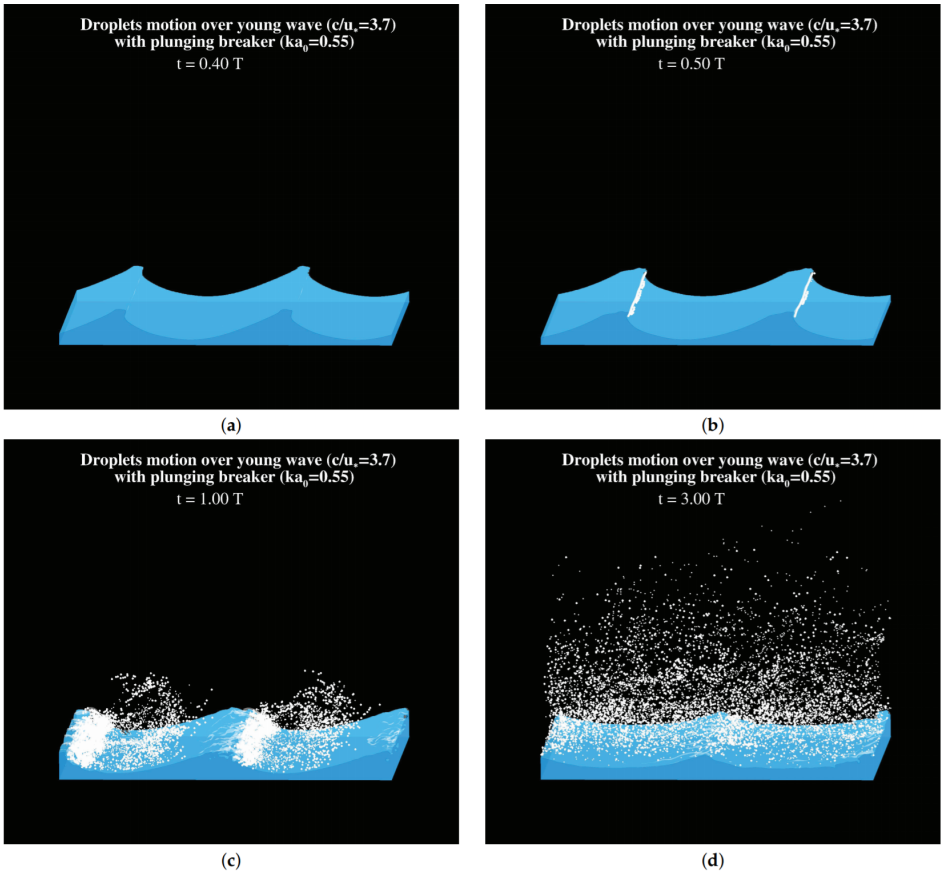

Figure 1.7: A series of snapshots from a numerical simulation of breaking waves with wind above from Tang et al. [2017].

where $\epsilon(t - \Delta\tau)$ is the time-dependent turbulent dissipation rate, $\Delta\tau$ is the time scale of the collapse of the air pocket initially entrained by the wave, W is a weighted velocity for the raising bubbles, r_m is the maximum bubble radius, g gravity, V_0 is the initial volume of entrained air, B is a dimensionless constant, and r the bubble radius. Additionally, they found scaling laws for the total volume of entrained air during a breaking event. Figure 1.6 shows a visualization of the air-water interface after the wave breaking where bubbles and drops can be seen.

Tang et al. [2017] developed a direct numerical simulation scheme to study the generation and transportation of spume drops by wind blowing over breaking waves. They found that drops are generated near the wave crest for young wave ages and near and behind the wave crest for old wave ages. Additionally, they found that plunging breakers generated more drops than spilling breakers. Figure 1.7 shows four snapshots from their direct numerical simulations where drops are shown in white and time advances from (a) to (d).

Chapter 2: Experimental Details

This chapter describes the facilities and methods used in the present experiments to study drop production mechanisms in breaking waves. In these experiments, three mechanically generated breakers, all with the same average wave packet frequency but with varying breaking intensity, were selected for study. In this dissertation, the three breakers are referred to as weak, moderate, and strong. Simultaneous measurements of drops, at many streamwise positions above each breaker, and surface profile histories were conducted during many repeated breaking events for each wave condition. In the following chapter, the first section is a brief overview of the research objectives of these experiments. The second section discusses the experimental facilities and methods used to generate the breakers, while the third section discusses the techniques used to measure the drops and breaker surface profiles.

2.1 Overview and Research Objective

The previous chapter highlighted recent field and laboratory experiments that have studied spray generation by breaking water waves. However, the precise physical mechanisms that generated drops during wave breaking are still poorly understood. The objective of the experimental study in this dissertation is to explore

the physics of the wave breaking and drop generation processes and determine how they relate to breaker intensity. Breaker profile histories are used to measure wave parameters, such as jet impact speed, that can be used as quantitative measured of breaker intensity. Measurements of drops generated by a breaking wave are used to obtain drop statistics like the number, size, and spatio-temporal distribution of drops.

2.2 Experimental Facilities

All of the data analyzed in this dissertation was collected in the wind-wave facility in the Hydrodynamics Laboratory at the University of Maryland. This includes droplet measurements for the weak and strong plunging breakers, which were originally performed by Sophie D. Wang Wang [2012], and similar data for the droplet measurements for the moderate plunging breaker and surface profile measurements for weak, moderate, and strong breakers, which were performed by the author. The wind-wave facility and wave generation technique is described in this section.

2.2.1 Water Wave Tank

The following description of the wave tank, wave maker, and wave maker motion applies to the experiments for all three breakers. Experiments are performed in a wind-wave tank that is 14.8 m long, 1.15 m wide, 2.2 m tall, with and a water depth of 0.91 m, as shown in Figure 2.1. The tank includes a programmable

wavemaker, a beach located on the opposite end of the tank from the wave maker, a programmable instrument carriage, an open return wind tunnel, and a water filtration system. Finally, a beach, which dampens the wave energy after the experiment has concluded, is located on the opposite end of the tank from the programmable wave make.

The programmable wavemaker consists of a wedge spanning the width of the tank and is located at one end. The side of the wedge closest to the end of the tank is vertical and the opposite side (facing the tank) is inclined at 30° from the vertical. The wedge is driven by an electric servo motor via a ball screw and rides on two parallel vertically oriented linear bearings. A feedback control system is used in conjunction with a position sensor and tachometer to control the motion of the wedge. Repeated measurements indicate that the RMS variation of the position of the wedge at the time of the peak amplitude of the wave maker motion is only 0.5 %.

The programmable instrument carriage runs along the length of the wave tank and is supported by two linear tracks that are mounted on top of the tank. The carriage rides on hydraulic oil bearings, which provide low vibration during carriage motion, and is driven by an electric motor. A feedback control system, working in tandem with a position sensor, is used to create highly repeatable carriage motions. Most of the optical and camera systems used in this study are directly attached to the instrument carriage. With this mounting system, the optical measurement equipment can be moved to various locations along the tank without realignment. Using the carriage control system, it can be positioned with and accuracy of ±

0.025 mm.

The wind tunnel is powered by two 7.5 HP fans and is open to the atmosphere at the inlet and outlet, see Figure 2.1. Air enters the wind tunnel through the fans and the flow coming from the fan outlets passes through a system of turning vanes, screens, and flow straighteners in order to condition the flow. The outlet spans the 1.15 m width of the tank and is 0.76 m high. The bottom of the outlet is 5 cm from the still water level when the water depth in the tank is 0.91 m. The wind tunnel is capable of generating wind speeds up to 10 m/s. Waves in the tank can be generated by the wind tunnel alone, by the mechanical wave maker or both systems can be used in conjunction. In the present study, waves were generated by the wave maker alone and the wind tunnel was only used to clean the water surface between measurement runs, see below.

A water skimmer and filtration system is used to fill the tank and periodically clean the water in the tank. The filling procedure for the tank start by filling a holding tank with tap water, which is filtered through a series of two 20, 10, and 5 μm filters. Hypochlorite is added and mixed to the water in the holding tank at a concentration of 10 ppm in order to neutralize and prevent organic material from growing in the water. The hypochlorinated water is transferred to the wave tank and is filtered through a diatomaceous earth filter for two days. Just before the breaking wave experiments the free chlorine level in the tank is reduced by the addition of Hydrogen Peroxide (H_2O_2) and a sufficient amount of Fluorescein dye is added and mixed into the tank for wave profile measurements, elaborated upon in a later section. The reduction of free chlorine is necessary since chlorine bleaches the

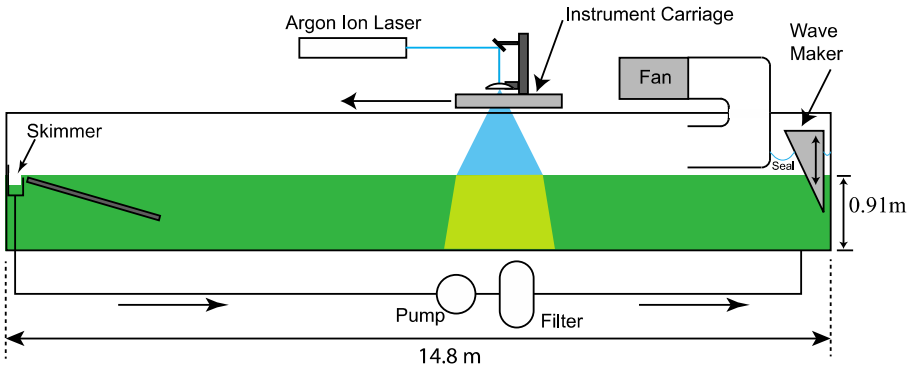

Figure 2.1: A side view schematic of the wave tank. The tank is 14.8 m long, 1.15 m wide, and has a water depth of 0.91 m. The wedge (seen on the right) is part of the wavemaker control system and is typically partially submerged in the water. Most laser, optical, and camera equipment is attached to the instrument carriage. The instrument carriage is shown here configured for wave profile measurements. At the end opposite to the wavemaker is an artificial beach, a sloped panel of plexiglas spanning the width of the tank, used to dissipate wave energy after the experiment has been conducted.

Flurescein dye. Between each experimental run, the water skimming, wind tunnel, and filtration systems are turned on periodically to maintain a low level of naturally occurring surfactants on the water surface.

2.2.2 Wave Generation Method

The waves in this study are generated via a dispersively focused wave packet technique as described in Duncan et al. [1999] and Wang et al. [2018]. The wave generation method, first proposed by Rapp and Melville [1990] and Longuet-Higgins [1976], produces a packet of linear deep-water waves with varying frequencies such that the packet converges as it travels down the length of the tank. The convergence

of the packet causes the amplitudes of each component to constructively interfere. If the initial amplitudes of the waves are sufficiently large, the largest wave in the converged packet will reach a critical amplitude and form a highly nonlinear breaking wave.

Linear deep-water wave theory is used to compute a suitable motion for the wavemaker. The packet consists of N sinusoidal components where the vertical wavemaker motion is given by:

$$z_w = w(t)\frac{2\pi}{N}\sum_{i=1}^{N}\frac{1}{k_i}cos\Big(x_b\Big(\frac{\omega_i}{\bar{c}} - k_i\Big) - \omega_i t + \frac{\pi}{2}\Big) \tag{2.1}$$

where A is the overall wavemaker amplitude, N is the number of wave components, k_i and ω_i are the wave number and frequency of each wave component, $\bar{c}$ is the average wave group velocity of all N components ($\bar{c}_i = 1/2(\omega_i/k_i)$). The frequencies of each wave component are equally space, $\omega_{i+1} = \omega_i + \Delta\omega$ where $\Delta\omega$ is a constant. The variable x_b determines the breaking position, measured from the back of the wedge, along the length of the tank as predicted by linear wave theory. The window function $w(t)$ gives the wedge zero motion when the sum of all N components results in very small wavemaker motion and is chosen as:

$$w(t) = \frac{1}{4}\Big(\tanh(\beta\bar{\omega}(t-t_1)) + 1\Big)\Big(1 - \tanh(\beta\bar{\omega}(t-t_2))\Big) \tag{2.2}$$

where β determines the rate rise of the window function and $\overline{\omega} = 1/N\sum_{i=1}^{i=N}\omega_i$. Except for the rise and fall time regions close to t_1 and t_2, the window function is equal to 1 for the time interval $t_1 < t < t_2$ and zero at all other times. The times t_1

Table 2.1: Table of wavemaker parameters for the three waves studied in this dissertation, the weak, moderate and strong plunging breakers. All three waves have the same average wave packet frequency of $f_0 = 1.15$ Hz.

x_b/λ_0	A/λ_0	Breaker Type	Date collected
6.20	0.076	Strong Plunging Breaker	Winter 2012
6.20	0.074	Moderate Plunging Breaker	Summer 2019 (new holographic setup)
6.17	0.070	Weak Plunging Breaker	Winter 2012

and t_2 were chosen to allow the highest and lowest frequency wave components to be generated and travel to x_b, the breaking position, and are given by:

$$t_1 = x_b(\frac{1}{\bar{c}} - \frac{1}{c_N}), \tag{2.3}$$

$$t_2 = x_b(\frac{1}{\bar{c}} - \frac{1}{c_1}) + 10. \tag{2.4}$$

Three plunging breaking waves of different intensities, a weak, moderate, and strong plunging breaker, were generated using the technique described above. For all three breakers the wave generation parameters were $N = 32$, $h/\lambda_0 = 0.35792$ (where h is the distance between the mean water level and the vertex of the wedge and $\lambda_0 = 2\pi g/\bar{\omega}^2$, where g is the gravitational acceleration constant), $H/\lambda_0 = 0.7458$ (where H is the mean water depth in the tank), $N\Delta\omega/\bar{\omega} = 0.77$, and $f_0 = \bar{\omega}/2\pi = 1.15$ Hz (where f_0 is the average wave packet frequency in hertz). The wave maker motions for the three breakers differ in the values chosen for the breaking distance, x_b/λ_0, and the overall wavemaker amplitude, A/λ_0. Important wave generating parameters for the three breakers are given in Table 2.1. Plots of the wedge motion (height verses time) for the three breakers are shown in Figure 2.2.

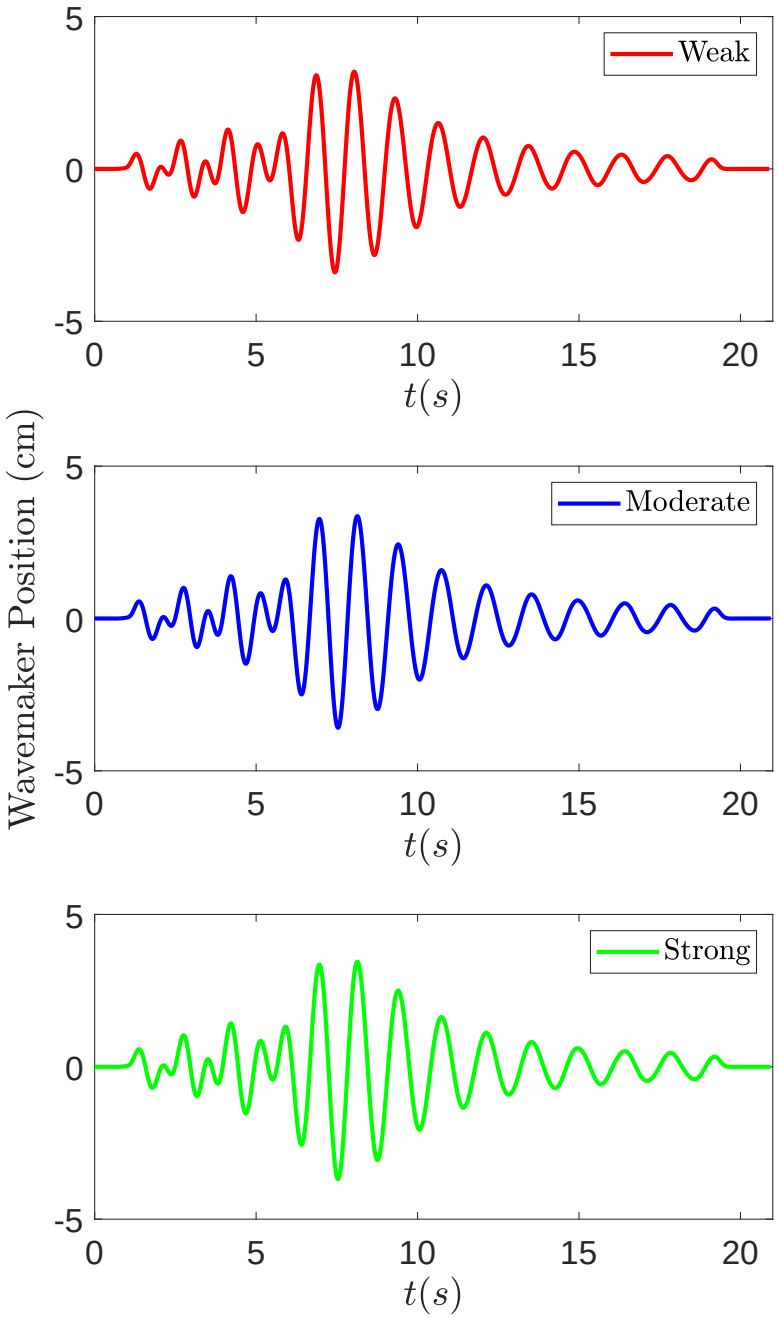

Figure 2.2: The wave maker motion (position vs. time) for the weak, moderate, and strong breakers.

2.3 Experimental Measurement Techniques

In this section, the measurement techniques used to obtain drop and breaker profile measurements are presented and discussed. In subsection 2.3.1, the in-line holographic system, which is used to measure drops, and an associated custom drop tracking code are discussed. Then, in subsection 2.3.3, the laser induced fluorescence technique, which is used to measure the breaker surface profiles, is described. Finally, techniques for measuring the humidity and surface tension, which are monitored during the experiments, are discussed.

2.3.1 Drop Measurements Using In-line Holography

In-line holography uses a coherent and collimated laser beam as a light source to illuminate a camera whose line of sight is coincident with the optical axis of the collimated laser beam. An object, in the case of these experiments a drop, that is in the path of the collimated laser beam is recorded as a hologram by the camera sensor. A hologram is a record of the interference formed by the collimated and coherent laser beam and the light diffracted by the drop. The recorded interference pattern contains the phase and amplitude of the diffracted waves [Katz and Sheng, 2010]. This information contained in the interference pattern is used to reconstruct the hologram via image processing and computational techniques.

The holographic image sequence for the weak and strong intensity plunging breakers were collected in the Winter of 2012 by Sophie D. Wang, who used a different illumination and optical setup than was used in the measurements for the

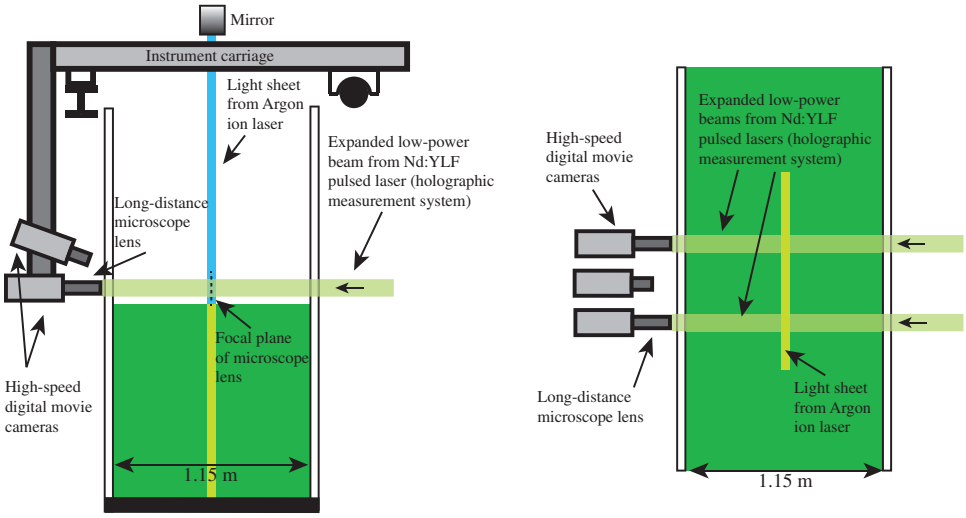

Figure 2.3: An end (left) and plan (right) schematic drawings of the wave wave tank with the drop and surface profile measurement system components shown. The end view schematic shows the laser light sheet, used to illuminate the water surface and measure breaker profiles, attached to the instrument carriage. Also attached to the instrument carriage are two high speed cameras for the drop measurements (one behind the other, bottom camera in the end view) and a camera used to measure the free surface profiles (top camera in the end view). The plan view (right schematic) shows the two cameras used for drop measurements along with two separated collimated laser beams directed into the two cameras.

moderate intensity breaker (see Table 2.1). The two optical setups and illumination light sources are described in two separate paragraphs below.

2.3.1.1 Winter 2012 Collimated Laser Beam Optical Setup

The illumination in the holographic system employed to capture drop data for the weak and strong breakers is provided by a high-energy pulsed Nd:YLF laser (Photonics Industries, DM50-527, 50 mJ/pulse at repetition rates of up to 1 kHz, pulse width 120 ns). Most of the beam power is dumped using a series of half-wave plates, thin-film beam splitters, and beam dumps. The remainder of the beam (on the order of about 40 μJoules/pulse) is spatially filtered and expanded to a diameter of about 50 mm. In the final conditioning stage, the beam is split and projected horizontally across the 1.15 m width of the wave tank. This optical setup is depicted in Figure 2.4.

2.3.1.2 Summer 2019 Collimated Laser Beam Optical Setup

The optical system employed to generate the collimated laser beam for the weak and strong breakers used a laser that was intended for more demanding applications (such as high speed PIV). The laser was too powerful (up to 99.9 percent of the laser power was dumped), had a high pulse to pulse intensity variation, and was large and cumbersome. Therefore, a simpler optical system for the in-line holographic drop measurements was designed and used to record drop data from the moderate breaker.

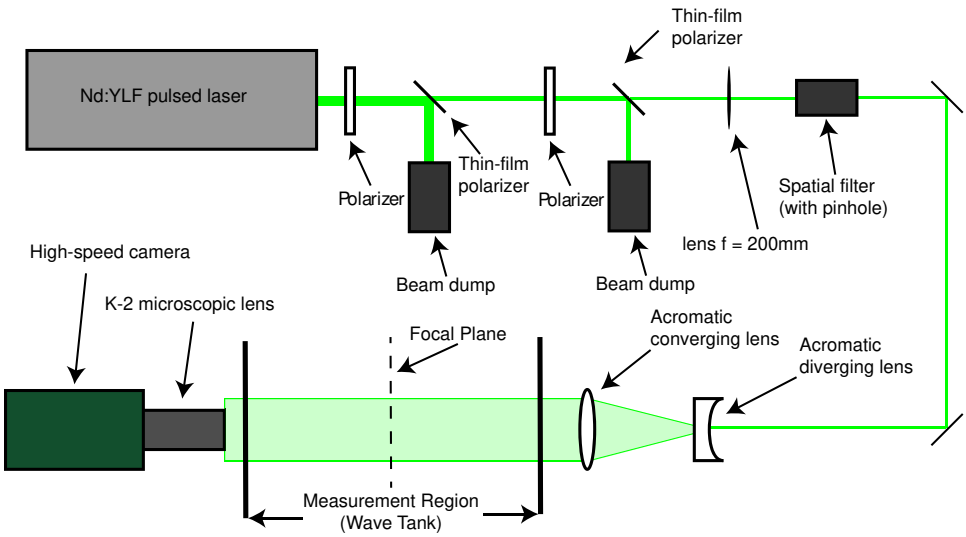

Figure 2.4: The optical setup used to generate a collimated laser beam approximately 50 mm in diameter used to collect drop in-line holographic data for the weak and strong plunging breakers. A high-energy Nd:YLF laser (50 mJ/pulse) is used as the light source. The light coming out of the laser is polarized and most of the energy from the pulse is dumped. The light is then passed through a spatial filter, collimated, and expanded through a series of two achromatic lenses (one converging one diverging) are used to create the collimated laser beam. The beam is then directed horizontally across the width of the tank (1.15 m) and into a camera on the other side of the tank.

The new system, shown in Figure 2.5, uses a low-powered Nd:YLF laser (CrystalLaser, QL527-200, 80 μJ/pulse at repetition rates of 1 kHz, with a pulse width of 20-30 ns) as the illumination source. The beam is spatially filtered to improve beam quality, passed through neutral density (ND) filters to reduce the intensity output by approximately half, and collimated by a single 50.8 mm achromatic converging lens, whose focal point is located at the pinhole. The collimation of the resulting 50 mm diameter laser beam is checked with a shear plate interferometer (Newport Optics, model 20QS20). The collimated laser beam is projected horizontally across the 1.15 m width of the wave tank.

The spatial filter consists of a pinhole, objective, and a position platform. Selection of the optimal pinhole (and objective) is dependent on input beam parameters and is given by the equation:

$$D_{opt} = \frac{f_{efl}\lambda}{a_{in}}, \tag{2.5}$$

where D_{opt} is the optimal pinhole diameter, f is the effective focal length of the microscope objective, λ is the wavelength of the laser, and a_{in} is the radius of the input beam. A 20x objective (Newport Optics, model M-20X) with an effective focal length $f = 9$ mm was chosen. The wavelength of the laser is $\lambda = 527$ nm and the input beam radius is measured to be 0.77 mm. The input beam radius can be measured by using the divergence angle of the beam (3 mrad) and the radius of the beam at a known distance (0.54 mm in radius 25.4 cm away from laser). Plugging these number into Equation 2.5, the optimal pinhole diameter was found

to be approximately 5 μm.

After the beam passes through the spatial filter it has divergence angle given by:

$$\theta = \tan^{-1}\left(\frac{D_{in}}{2f_{efl}}\right), \tag{2.6}$$

where θ is the divergence angle measured from the centerline of the beam, D_{in} is the diameter of the input beam, and f_{efl} is the effective focal length of the microscope objective used. Using $D_{in} = 1.54$ mm and $f_{efl} = 9$ mm the divergence angle is found to be 9.71 deg. The resulting collimated laser beam diameter is calculated to be 64 mm when using a 200 mm collimating lens.

The new optical setup is significantly better than the one used for the strong and weak breakers because it uses a low-powered laser, which has a lower signal to noise ratio, smaller pulse to pulse energy variation, and lower pulse duration. Additionally, the low laser power results in a much simpler optical setup, as evident by comparing Figures 2.4 and 2.5, and a more compact optical system that can be easily moved to a new experimental setup. A comparison of typical recorded holograms of drops using the old ((a), Winter 2012) and new ((b), Summer 2019) collimated laser beam optical setups is shown in Figure 2.6.

2.3.1.3 Camera Setup Used to Record Holograms

On the opposite side of the tank from the light source, a high-speed digital movie camera (Phantom V640, 4 Megapixel 12 bit images) fitted with a long-distance

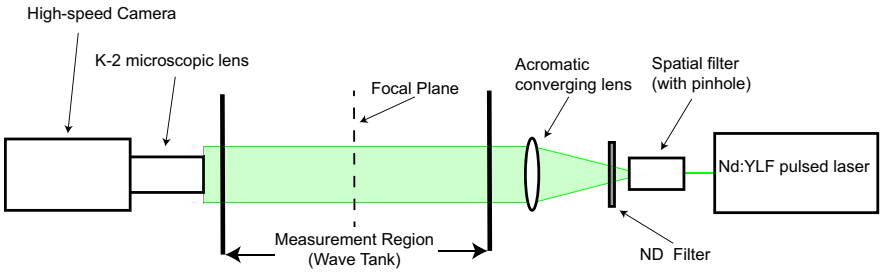

Figure 2.5: The new and improved optical setup used to generate a collimated laser beam approximately 50 mm in diameter that was used to collect drop in-line holographic data for the moderate plunging breakers. A low-powered Nd:YLF laser (50 μJ/pulse) is used as the light source. The light is passed through a spatial filter and a neutral density filter, and is then collimated by a single achromatic converging lens. The collimated laser beam is then directed horizontally across the width of the tank (1.15 m) and into a camera on the other side of the tank.

microscope lens (model K2 by Infinity, Inc.) is aligned so that the face of the sensor and the optical axis of the lens is coincident with the collimated laser beam. The laser pulse and camera are synchronized to take holographic image sequences at a rate of 650 Hz with the bottom edge of the images located 12 mm above the maximum wave crest height. The horizontal surface 12 mm above the maximum wave crest height is referred to as the measurement plane in this dissertation. Holographic image sequences are taken at 28 streamwise locations above the breaking wave and the results are interpolated to cover regions between adjacent locations where there are no measurements. The streamwise drop measurement locations cover a streamwise region from just before the jet impact to approximately 1 meter downstream from the (farther from the wave maker) jet impact site. At each location, at least

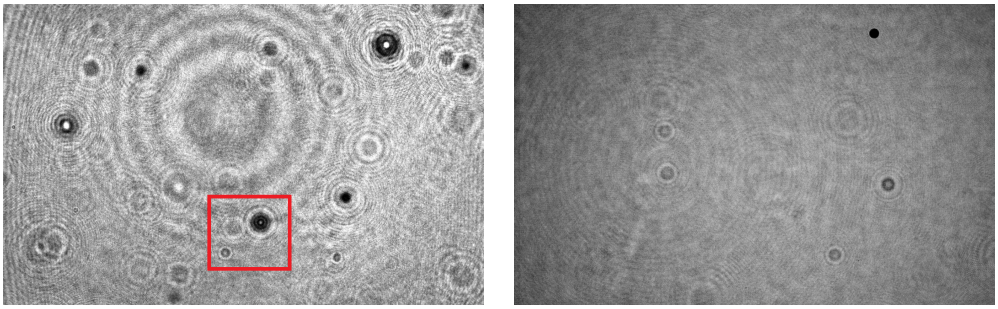

(a) (b)

Figure 2.6: Two sample images of drop holograms where (a) was recorded with the hologram illumination system used for the weak and strong breakers collected in the winter 2012, while the hologram in (b) was recorded with an improved illumination system used for the moderate breaker. Holograms of drops show up as either black dots surrounded by interference rings or just as interference rings. Both images are approximately 25.6 mm x 16 mm with spatial resolution of 10 μm per pixel and are able to reconstruct drops with diameter of $d > 50\mu$m over the entire width of the tank, 1150 mm. The red box is referenced in the next section and in Figure 2.7.

10 experimental runs were performed for a total of at least 140 unique realizations of each breaking wave.

2.3.1.4 Hologram Image Processing

Holography is a three-dimensional (3D) imaging technique where interference patterns formed by the interaction of a reference beam and light diffracted at object boundaries are recorded by a camera. With recent advanced in digital cameras and computing power, holography has been widely adapted to measure the 3D position, tracks, and size of bubbles and drops Katz and Sheng [2010]. In the present experiments a form of holography in which the reference beam and the recorded image are parallel, called inline holography, is used.

The basic principles of hologram reconstruction is shown in Figure 2.7. The image shown in Figure 2.7 (a) is a cropped image inside the red box in the hologram

shown in Figure 2.6 (a). In this cropped region, the holograms of three water drops, labeled A, B, and C, generated by a breaking water wave, can be seen. The hologram of each drop consists of a characteristic circular pattern caused interference of the reference beam and diffracted light from the drop. This image can be digitally reconstructed at any position in the depth direction, z, along the axis of the collimated beam (where $z = 0$ is the location of the focal plane of the camera lens) using a model for the propagation of diffracted light Katz and Sheng [2010]. When the hologram is reconstructed at the actual location of the drop, the reconstructed image of the drop is typically a solid black circle with a sharp edge. As the location of the reconstruction is moved away from the z location of the drop, circular interference patterns start to appear inside and around the edges of the drop.

Figure 2.7 (b) shows the recorded hologram in (a) reconstructed at a depth of $z = 133$ mm away from the focal plane. In this image drop B becomes sharp and in focus while drops A and C are not. Because B is sharp in Figure 2.7 (b), it indicates that the plane of best focus for drop B is close to $z = 133$ mm, which is also close to its physical position in depth. Similarly, Figure 2.7 (c) and (d) show the hologram reconstructed at $z = 268$ mm and $z = 331$ mm away from the focal plane, where drops C and A come into focus, respectively. Figure 2.7 (d) specifically highlights the power of holography in measuring the size and position of a drop. In the original recorded hologram, drop A appeared only as a faint, barely distinguishable interference pattern, yet in Figure 2.7 (d) the same drop appears sharp and in focus.

A recently developed GPU compatible MATLAB hologram reconstruction al-

gorithm, used in the image processing of holograms, was provided to us by Professor Joseph Katz form Johns Hopkins University. We gratefully acknowledge Professor Katz and his research group, because this reconstruction algorithm significantly decreased the computational time required to reconstruct holograms.

The image processing and the determination of the plane of best focus code for drop hologram processing was developed in-house and is loosely based on the Hybrid method proposed by Guildenbecher et al. [2013]. The process involves the following image processing steps for each hologram image:

1. Pre-process hologram image by subtracting background (Figure 2.8 (b)).

2. Reconstruct hologram at a coarsely spaced array in the depth direction, z, over the entire width of the wave tank (Figure 2.8 (c)).

3. Collapse the reconstructed image array into a single 2D (x-y) image and detect the drops by thresholding (Figure 2.8 (d)).

4. Reconstruct the holographic image in the depth direction, z, spaced every 500 μm in the vicinity of each detected drop. (Figure 2.9 (a)).

    - Calculate a mean sharpness criteria at each reconstructed plane (Figure 2.9 (b)).

5. Find plane of best focus by calculating a mean drop sharpness in the depth direction, z (Figure 2.9 (c)).

6. Reconstruct the drop at the plane of best focus (Figure 2.9 (d)).

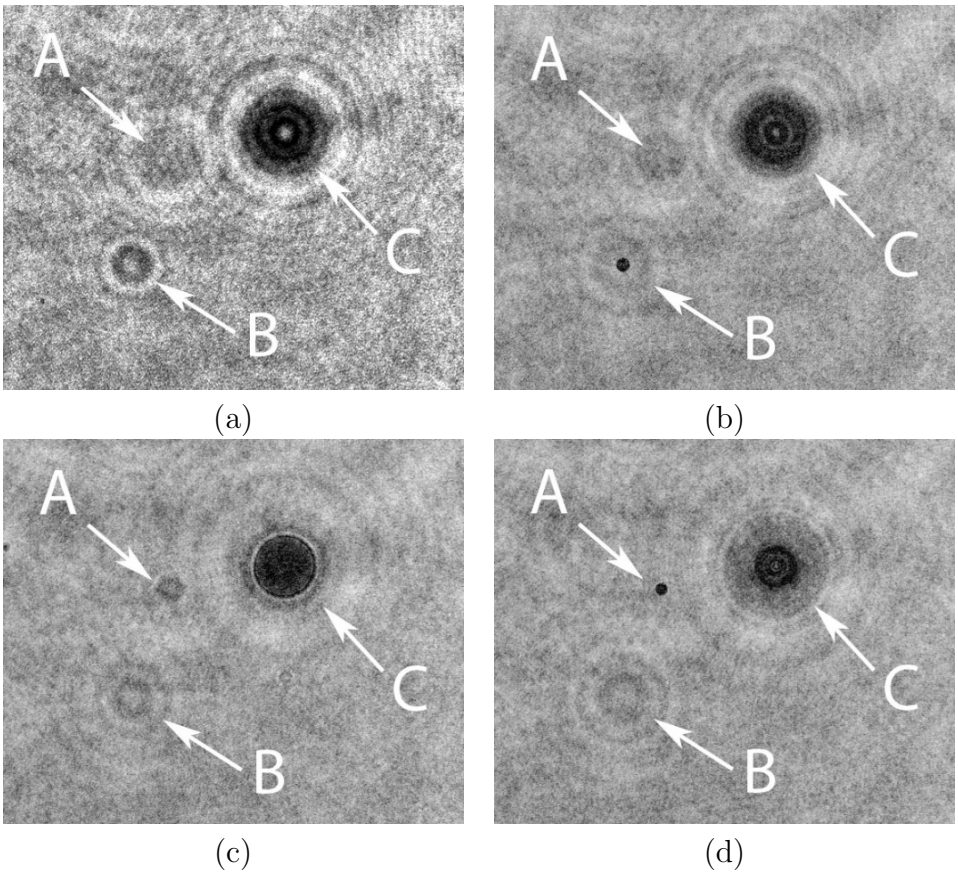

Figure 2.7: Original recorded hologram is shown in (a) (originally cropped from the red box from the hologram in Figure 2.6 (a)). Three distinct interference patterns, indicating that three drops are present, can be seen, labeled by the letters A, B, and C. In (b), the original image in (a) is reconstructed at a distance of $z = 133$ mm away from the focal plane where drop B is in focus. Image (c) shows the raw hologram in (a) reconstructed at $z = 268$ mm where drop C comes into focus. Finally, image (d) shows the image in (a) reconstructed at $z = 331$ mm where drop A comes into focus.

The results of the above hologram image processing steps are depicted in Figures 2.8 and 2.9. Figure 2.8 (a) shows the original recorded hologram as it was captured by the laser-optical-camera system (hence forth referred to as the hologram). The first processing step is to homogenize the intensity distribution of each hologram and remove any drops that may be on the tank wall or imperfections from the manufacturing process of the tank's plastic walls. This is accomplished by calculating a time series (typically 50 images) averaged hologram from holograms recorded before drops are generated by the breaking wave. The original hologram is subtracted from the background averaged hologram and referred to herein as the enhanced hologram, seen in Figure 2.8 (b). The only pronounced features in the enhanced hologram are interference patterns of drops generated by the breaking wave. Note that there are many interference patterns in Figure 2.8 (a) that do not change in time and are filtered out by this pre-processing.

In step 2, the background-subtracted hologram, shown in Figure 2.8 (b), is digitally reconstructed every 5 mm in the depth (z) direction. The 3D reconstructed volume is collapsed into a single image containing the minimum intensity at each x-y image location overall all the images in the depth direction, referred to as the collapsed hologram and shown in Figure 2.8 (c). The approximate location and size of a drop is measured by thresholding the collapsed hologram, shown in Figure 2.8 (d).

The steps outlined in the previous two paragraphs were solely for the purpose of detecting the approximate 3D location and approximate size of drops in each hologram image. The plane of best focus cannot be obtained accurately from the

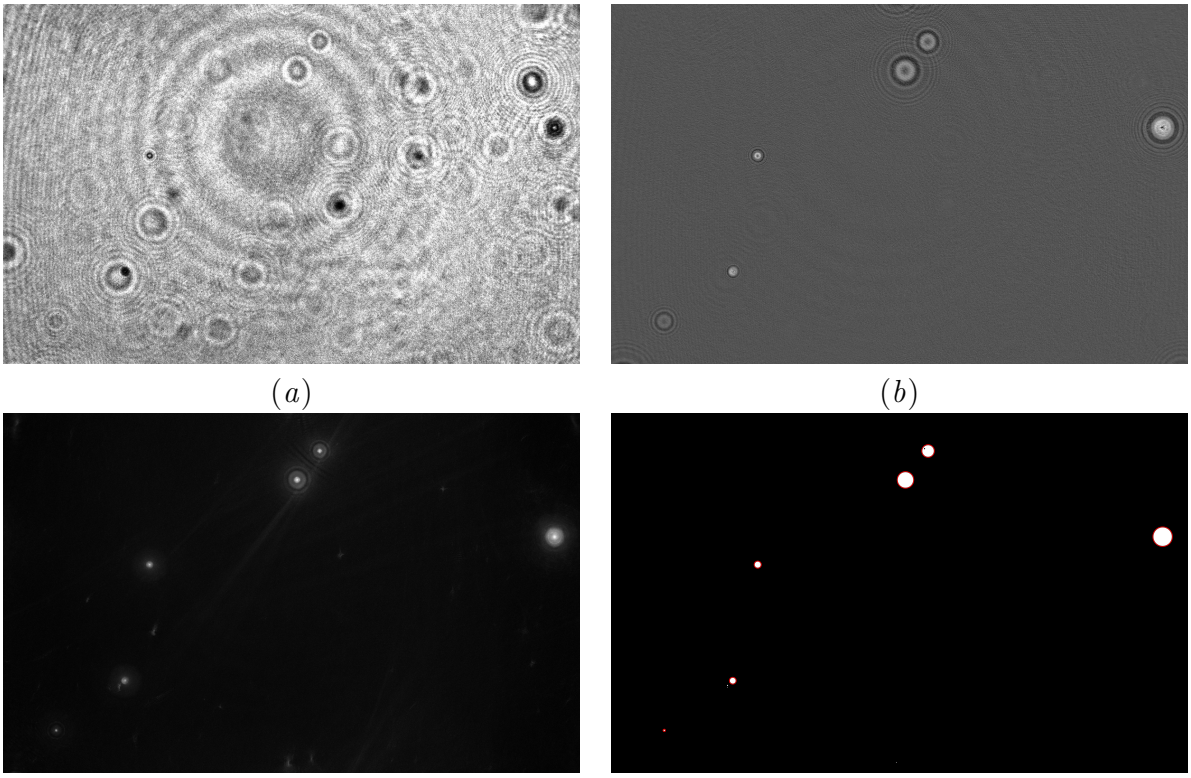

Figure 2.8: Series of images showing the first stage of the reconstruction process, where drop location and approximate radius is measured. The original recorded hologram is shown in (a). A time-averaged background is subtracted from (a) and is shown in (b). This background subtracted hologram is reconstructed every 5 mm in depth and the resulting 3D reconstructed hologram volume is collapsed by taking the minimum intensity of each pixel in depth. The resulting collapsed hologram is shown in (c). Finally, the drops' location and approximate size are measured by thresholding the collapsed hologram, with the result shown in (d).

coarse hologram reconstruction. In order to obtain an accurate measurement of the plane of best focus for each drop, a small 200 by 200 pixel window around each drop is cropped from the raw hologram, shown in 2.9 (a). The extracted hologram is reconstructed using the above described algorithm, at an array z locations spaced every 500 μm around the estimated z location of the drop. A sharpness criteria, based on the Tenengrad operator (see Guildenbecher et al. [2013]), is calculated at each reconstructed plane, see Figure 2.9 (b). The idea behind calculating a sharpness criteria at each plane stems from the idea that the drop image will be sharpest when it is in focus. A mean value for the drop sharpness is calculated at each reconstructed plane and a plot of mean drop sharpness vs. depth is obtained, see for example Figure 2.9 (c). The mean sharpness has a peak at about 74 mm from the lens focal plane for this particular drop, which indicates the plane of best focus. When the hologram is reconstructed at this depth location the image appears sharp and in focus, see 2.9 (d). This process is repeated for all detected drops in each hologram.

2.3.1.5 Drop Radius Measurement

The drop radius is measured by fitting a hyperbolic tangent function by least-squares linear regression to the inverse intensity map of the drop when it is reconstructed in the plane of best focus. The fitting function has the following form:

$$\gamma = \gamma_f \Big[1 - \tanh \Big(\beta_f ((x_{i,j} - x_f)^2 + (y_{i,j} - y_f)^2 - r_f) \Big) \Big], \tag{2.7}$$

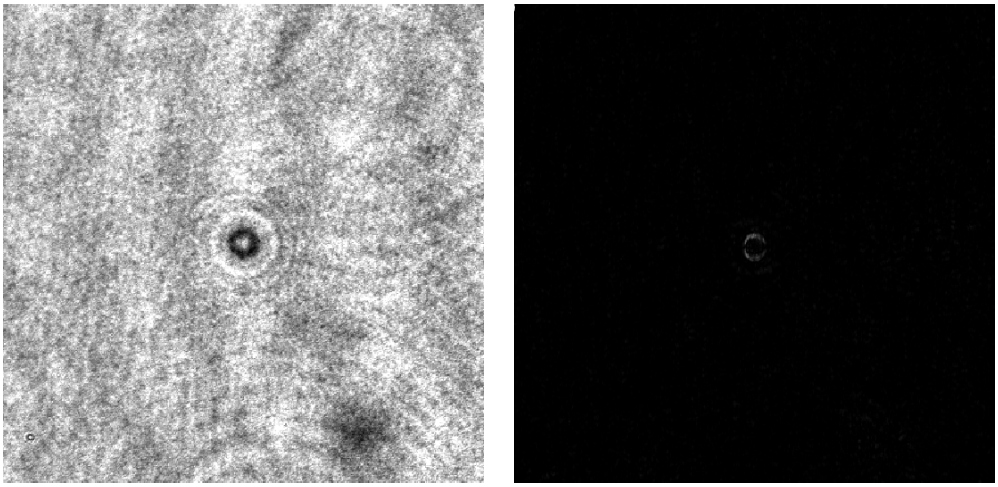

(a)

(b)

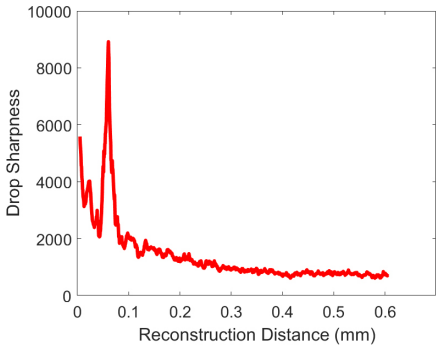

(c)

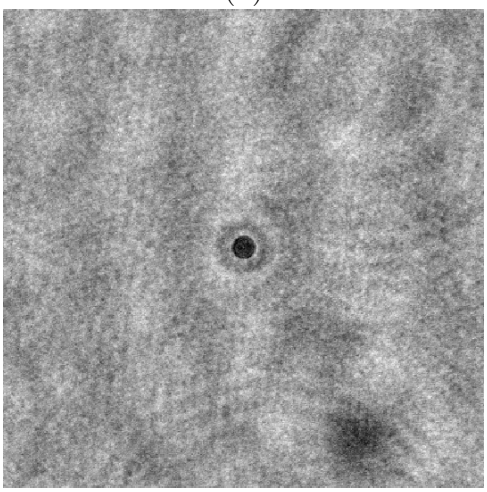

(d)

Figure 2.9: Series of images showing the second stage of the reconstruction process, in which the plane of best focus is calculated for each drop. The raw cropped hologram of a drop is shown in (a). The sharpness criteria, based on the Tenegrad operator, at a single plane is shown in (b). The mean drop sharpness vs. depth is shown in (c) with a defined peak near the plane of best focus for the drop. Finally, the reconstructed drop at the plane of best focus is shown in (d).

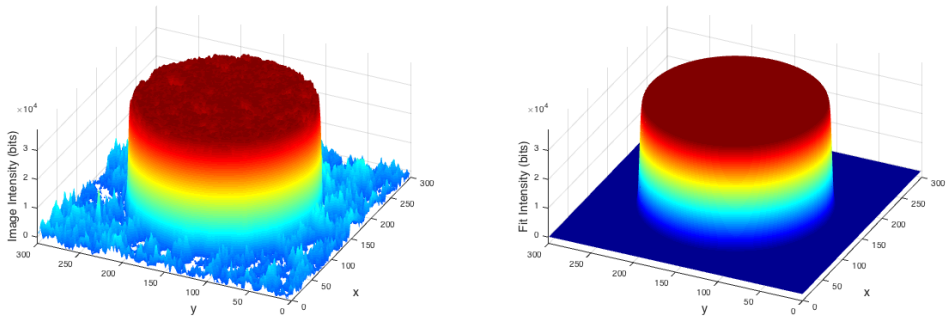

(a) (b)

Figure 2.10: The inverse of the intensity map of a 1000 micron dot from the calibration reticle shown in Figure 2.11 (a) is shown on the left. The image on the right shows the hyperbolic tangent function fit of the same drop.

where γ is the fitted inverse intensity profile, γ_f is the maximum value of the inverse intensity of the drop, β_f is a parameter that characterizes the slope of the function at the boundary between the intensity of the drop and the background, x_f and y_f are the fitted x and y positions of the drop and r_f is the fitted drop radius. The initial guess for the parameters in Equation 2.7 used for least-square fitting comes from the estimate of the position and radius obtained in the above-described coarse analysis, and radius guess from hologram image processing described above. Figure 2.10 shows the inverse intensity map for a 1000 μm circle from the calibration target (see following paragraph) and the resulting hyperbolic tangent fit of the same drop.

2.3.1.6 In-line Holography Calibration

The in-line holographic system is calibrated with a custom calibration target (referred to as the reticle) in order to ensure 1:1 magnification, determine measure-

ment region limits, and quantify drop radius measurement error. The reticle consists of a glass slide with 14 chrome sputter deposited circles with diameters ranging from 3000 μm to 30 μm. In order to ensure 1:1 magnification, the calibration target is placed in the focal plane of the K2 microscope lens (the focal plane is located near the center plane of the tank width). The magnification on the microscope lens is adjusted until it is close to 1:1 or 10 μm/pixel. The recorded hologram of the reticle (positioned near the focal plane of the lens) with the lens set to 1:1 magnification is shown in Figure 2.11 (a).

The second purpose of the calibration reticle is to ensure that the smallest drop considered in this dissertation ($d = 100$ μm) can be measured at the extreme ends of the measurement volume (near either side of the tank wall). In order perform this verification, the calibration target is placed in the furthest in-tank position from the focal plane of the microscopic lens, i.e. next to either tank wall. The hologram of the reticle is recorded and reconstructed at the z location of the reticle to ensure that the drop of $d = 100$ μm can still be measured accurately. The imaged and reconstructed holograms of the reticle near the tank wall are shown in Figure 2.11 (b) and (c). Note that in the reconstructed image the $d = 100$ μm drop appears sharp and in focus.

The final purpose of the calibration reticle is to quantify the drop radius measurement error. In order to achieve this the reticle is attached to a motorized linear traverser (NEAT 310M Programmable Stepping Motor Controller). The reticle is traversed and imaged across the measurement volume at known positions away from the focal plane. The recorded hologram at each known position from the focal plane

is reconstructed and the radius of each of the dots is measured, using the inverse hyperbolic tangent fit described in the previous section. From this data the drop radius measurement error is assessed. This procedure is also used to ensure the expanded laser beam used by in-line holographic system is collimated. The measurement error in drop radius is assessed to be no more than 3 percent of the drop radius over the entire width of the tank.

2.3.2 Drop Tracking Code

A custom MATLAB drop tracking code was written in-house using ideas from existing tracking algorithms and new ideas designed to overcome specific challenges related to tracking the drops generated by the breaking waves. One drop tracking challenge is due to the large variation of drop speeds in hologram movies. For example, in a series of five images there may be drops that are reaching the peak of their trajectories, thereby displacing only 100 pixels in the five frames, while simultaneously there may be a drop traveling much faster in the same set of images and displacing a total of 1600 pixels between the five frames. This variation in speeds makes it difficult to track drops using traditional tracking algorithms like nearest neighbor search.

Having determined the 3D location and size of all drops in each image for each run, the trajectory of the drops, $\rho_i(x, y, z, r, t)$, is determined using a drop tracking algorithms. The tracking algorithm used in this study is composed of two sub routines. The first subroutine of the algorithm is a nearest-neighbor search using

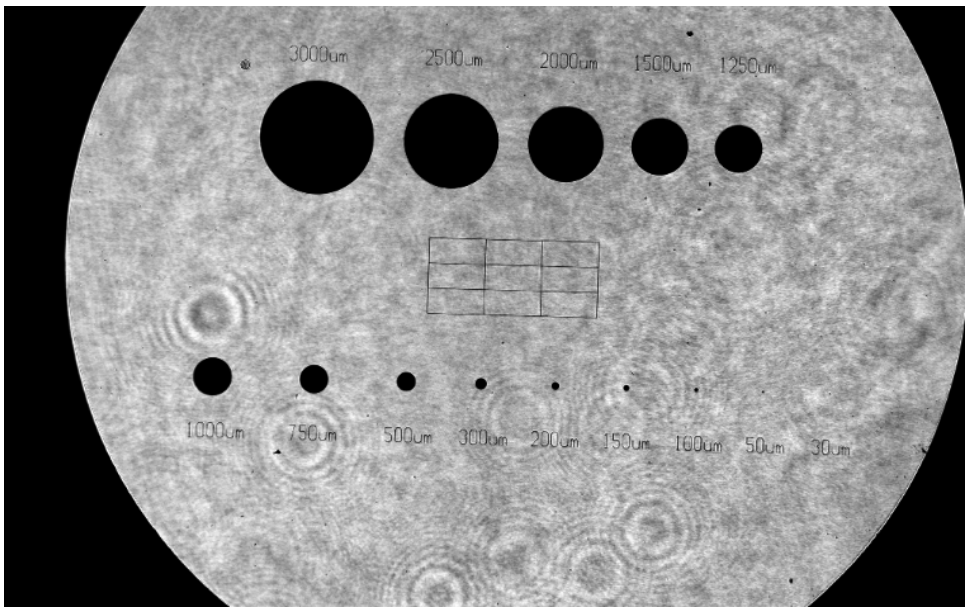

(a)

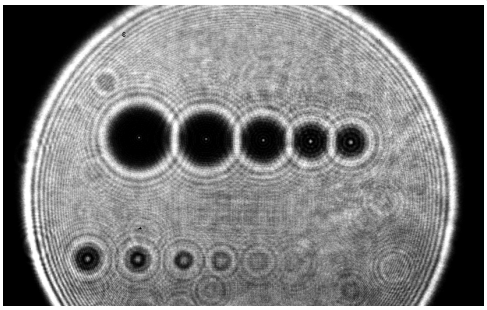

(b)

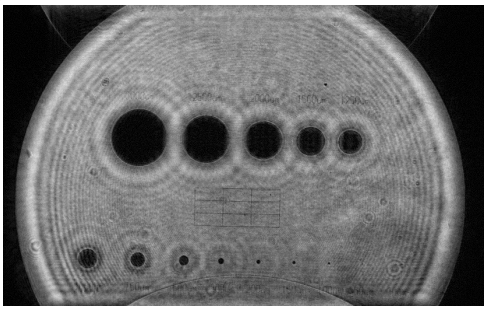

(c)

Figure 2.11: A calibration reticle with 14 chrome sputter deposited circles ranging in size from $d = 3000$ μm down to $d = 30$ μm. Image (a) shows the calibration target imaged by the digital in-line holographic system at the focal point of the camera lens. Hologram (b) shows the same calibration target imaged at the far sidewall of the tank (605 mm away from the focal plane); interference patterns can be seen in the hologram. Image (c) is the digital reconstruction of image (b) at $z = 605$ mm. Note that the original image is 2560 x 1600 pixels in size and that the $d = 100$ μm dot (seventh dot from the left in the bottom row) is visible and in focus in the reconstructed hologram.

the drop's 3D location and size. The second subroutine of the tracking algorithm was developed in-house to uniquely solve the problem of the wide range of drop velocities at each instant. The subroutine uses the tracking algorithm described above to iteratively track drops of increasing speeds, starting with the slowest drops.

The drop tracking algorithm used in this study is based on a modified nearest-neighbor algorithm developed for Brownian particle motion by Crocker and Grier [1996]. The modified code tracks particles based on their 3D position and radius between two consecutive frames by voting on the most likely track link from a set of drop candidates in the next frame. The set of candidates is selected based on the n drops in the next frame nearest to the drop being tracked from the previous frame, henceforth referred to as the tracked drop (typically, $n = 5$). The distance between the tracked and candidate drop is taken to be the 2D euclidean distance between the two based on x and y positions. If a candidate drop is greater than d_{max} away from the tracked drop, it is discarded from the candidate list. The remaining drops in the candidate list are then ranked from least to most likely matching candidate based on the relative x, y, z positions and radius r. Finally, the most likely candidate is required to pass a set of constraints based on the difference in size between the tracked and candidate drop, as well as the displacement in the z direction. Because the measurement of drop position in the z direction is not as accurate as the x and y position, this constraint is applied with loose tolerance.

In this tracking algorithm, linking drop positions into trajectories is only feasible if the typical drop displacement from frame to frame is smaller than the typical drop spacing in each of the same two frames. In other words, if two consecutive

frames contain a dense population of drops, and some of these drops are displacing by a distance greater than the typical drop spacing in one frame, then this tracking algorithm will not be able to link the tracks of the fast moving drops, which have the largest displacements from frame to frame. In order to address this issue an iterative subroutine that tracks slow moving drops first and faster drops later was developed in-house. The subroutine consists of the following steps:

1. Drops are initially tracked using the nearest neighbor algorithm described above with a very conservative maximum drop linking distance, d_{max}.

2. Drop tracks with fewer than three drop links are unlinked.

3. For each trajectory (resulting from the initial tracking algorithm) that is longer than three drop links:

   (a) The drop trajectory is predicted back in time by fitting a first order polynomial to the x and y position vs. time for the three nearest drop positions in time.

   (b) Any unlinked drop in the previous time step that is sufficiently close to the x and y predicted positions (within a given distance threshold) are assigned to the track existing track.

   (c) If no new drop is assigned to the existing track, the previous step is repeated for an additional previous time step (up to 7 times, then the code stops looking for candidate drops)

   (d) If a new drop is assigned to the track, the search is advanced one time

step back in time and step (a) is repeated with the a new set of three nearest drop positions in time.

4. The drops search process above is repeated forward in time.

5. All drops tracks with three or more drop links are removed from the data set of candidate drops for linking

6. The subroutine is repeated for the left over drops using a larger value for d_{max}.

At this point, all the drops with tracks are removed from further tracking consideration and the drops tracking algorithm is used iteratively with ever increasing maximum drops linking distance d_{max} until no drops are left to be tracked. The subroutine introduces physics of the pseudo-ballistic trajectories of the spray drops into the drop tracking method since it tries to predict future and past drops positions based on known information about the drop track.

The trajectory data for each drop is fitted to third order polynomials for $x_d(t)$, $y_d(t)$ and $z_d(t)$. The polynomials are then used to find the time t_0, x_0 and z_0 position, and velocity of each drop as it crosses the measurement plane, which is 1.2 cm above the maximum wave crest height. Only drops that are moving up through the measurement plane are included in the final data set. Drops that are moving downward at the bottom or top of the image space or through the side walls of the image space are assumed to have been accounted for at other measurement positions. In order to be tracked successfully, a drop must appear three times in a sequence of images. This means that the maximum vertical velocity of a drop

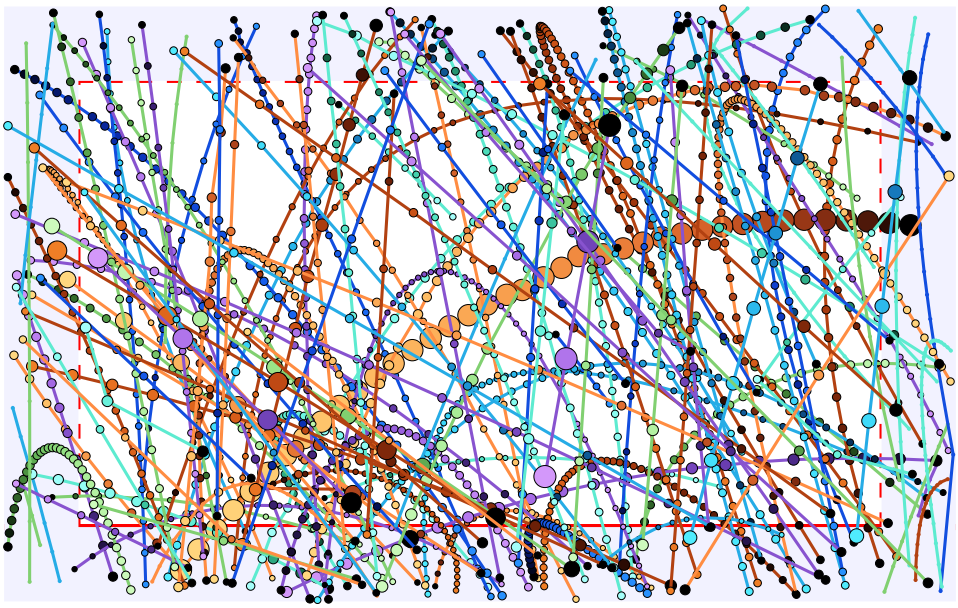

Figure 2.12: A sample plot of drop trajectories from one run spanning approximately 1300 images (2 seconds) with spatial dimensions of 25.6 by 16 mm. The relative drop diameters are indicated by the diameters of the markers shown in the plot. The drop positions are not necessarily equally spaced in time. Because holographic reconstructions of drops near the exterior boundaries of the image are more inaccurate, only drops 200 pixels (2 mm) inside the measurement window (the white region outlined by solid and dashed red lines) are reconstructed and their radius is measured. The measurement plane is indicated by a solid red line 200 pixels above the bottom edge of the frame.

must be below 2.6 m/s. A sample plot of drop trajectories from one run is shown in Figure 2.12.

2.3.3 Surface Profile Measurements

Surface profiles of the waves were measured with a cinematic Laser Induced Fluorescence (LIF) technique that has been used extensively in the Hydrodynamics Laboratory (see for example Duncan et al. [1999] and Wang et al. [2018]). The

method uses a thin (≈1 mm in thickness) vertically oriented light sheet from a 7-Watt Argon ion laser, with the majority of power coming from wavelengths of 488 and 524 nm. The laser light sheet illuminates the water in the longitudinal center plane of the wave tank. The water is mixed with a low concentration of Fluorescein dye which has strong excitation wavelengths of 475 and 490 nm and strong emission wavelengths near 510 and 520 nm. When the laser light sheet from the Argon ion laser (with peak power at $\lambda = 488$ nm, blue-green in color) illuminates the dyed water, it fluoresces a neon-green color ($\lambda = 510 - 520$ nm).

The laser is located on the downstream end of the wave tank. Several mirrors are used to reflect the laser beam so that it is positioned above and along the center plane of the wave tank. The laser beam is directed from the downstream end to the upstream end of the wave tank on top of the instrument carriage (discussed in section 2.2.1). A mirror is used to direct the beam vertically downward from the carriage and through two convex lenses, which are used to focus the laser beam on the water surface. Finally, a mirror directs the beam at an angle of 30 deg up from the horizontal to a rotating mirror that generates a thin laser light sheet that intersects the water surface. The light sheet thickness at the calm water surface is measured to be approximately 1 mm.

This LIF technique is used along with three time-synchronized high-speed cameras with slightly overlapping fields of view to capture a time history of the surface profile evolution during the active phase of wave breaking. Each high-speed digital movie camera (Phantom V640 or V9) views the intersection of the light sheet and free surface looking down at a shallow angle. Any residual laser light is filtered

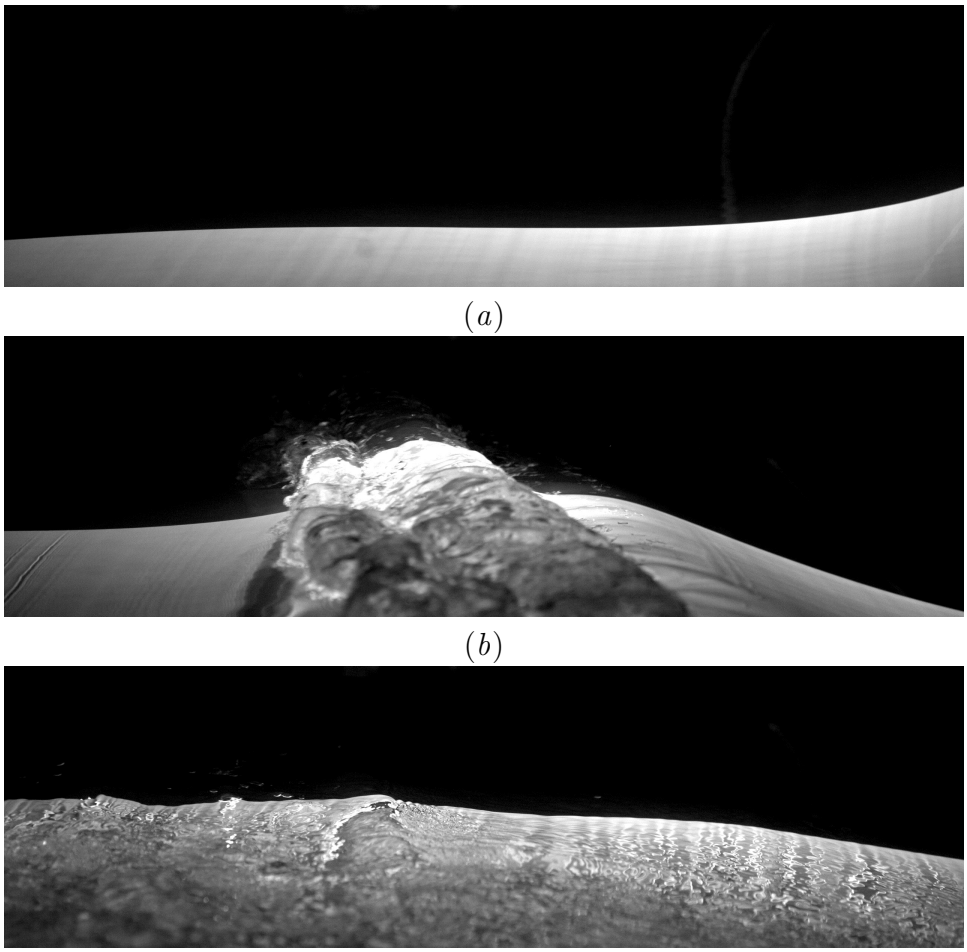

Figure 2.13: A sample sequence of LIF images of a breaking wave. The wave is moving from right to left with time advancing from image (a) to (c). The free surface is initially smooth in image (a), before the wave has broken. In image (b) the wave is breaking and surface roughness can be seen in the middle of the image. The part of the wave closest to the camera can be seen in the foreground of image (b). Finally, in image (c) the wave has passed. The surface profile in (c) looks less uniform due to a number of reasons, such as free surface roughness (causing water to act like a lens) or free surface features in the foreground of the image between the camera and lens.

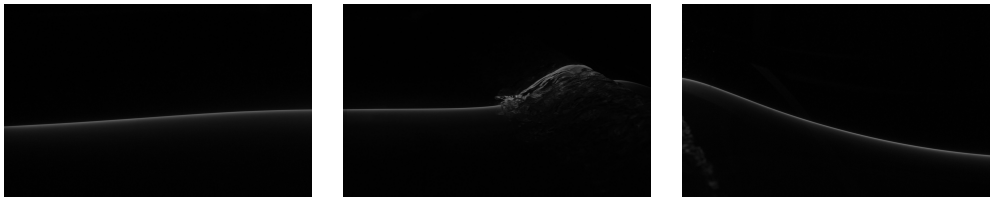

(a) (b) (c)

Figure 2.14: Three time-synchronized surface profile images just after jet impact and at the onset of the initial splash up. The three cameras have slightly overlapping fields of view and the wave is moving right to left.

by a long-wavelength-pass optical filter in front of the camera lens. A sample series of images from a breaking wave are shown in Figure 2.13. The cameras view the intersection of the light sheet and the water surface from a point just above the water level and off to the side of the tank. Movies are recorded at 650 images per second and the cameras have a sensor size of 2560 x 1600, with a combined field of view that covers approximately 1300 cm in the horizontal direction and 300 cm in the vertical direction with a spatial resolution of approximately 180 μm/pixel. The three cameras cover the plunging jet formation, jet impact, and subsequent splash up, capturing a total of 2000 images with a recording time of just over 3 seconds. Sample images recorded by the three cameras are shown in Figure 2.14.

The shape of the water surface at any instant is determined from the images by edge detection techniques implemented in MATLAB. The water surface is located to an accuracy of about ± 1 pixel or approximately ± 180 μm. Each set of three LIF images is captured simultaneously with the two holographic images. It should be kept in mind that the LIF image is captured over an interval of about 1/650 s while the holographic image is captured over the duration of the Nd:YLF laser light pulse,

which is on the order of 100 to 20 ns. Also, the drops are measured over the entire width of the tank while the water surface profile is measured over the thickness of the light sheet, about 1 mm, in the center-plane of the tank.

The image processing to determine the surface profile shape along the intersection of the laser light sheet and the water surface is done by a combination of automatic and manual image processing techniques based on gradient edge detection. First, an automatic edge detection MATLAB code is used to measure the surface profile shape from one side of the image to the other. If a surface profile is not detected from one side of the image to the other by the automatic processing code it is tagged and processed manually with the use of a touch sensitive tablet-pen system (Wacom, model Cintiq 21ux).

Once the surface profiles are processed, they need to be rectified and calibrated since the optical axes of the camera lenses are not perpendicular to the plane of the light sheet. Additionally, a camera calibration process can correct for any spherical abberation from the camera lens, convert the profiles from image coordinates to physical coordinates, and allow the surface profiles from three adjacent cameras to be stitched together. The calibration process is accomplished by placing a calibration grid, which spans the combined width of the fields of view covered by the three cameras, in the plane of the laser light sheet. The calibration board consists of a checkerboard pattern with squares that are 25.4 mm x 25.4 mm attached rigidly to an aluminum frame. The calibration process is carried out after the surface profile experiments were finished. In total, the experiments and calibration process were conducted over three days.

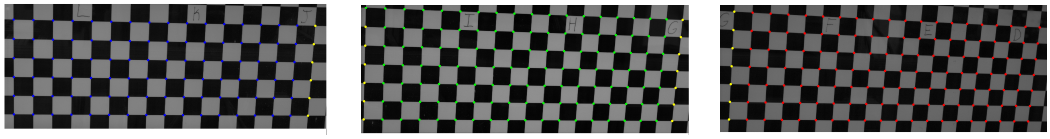

(a) (b) (c)

Figure 2.15: Images of the same calibration checkerboard target from the three cameras with slightly overlapping fields of view of view. The image points, (X_i, Y_i), are detecetd by an image processing code and used to convert from image coordinates to physical coordinates and transform the points to an orthogonal coordinate system. Image (a) is the left most camera, (b) is the middle camera, and (c) is the right camera, with the direction of the wave propagating from right to left. The yellow points seen in (a-c) are shared common points where the camera fields of view overlap, which are used to stitch the images together.

The calibration process for each individual camera is similar to the one described by Wang [2017]. Image processing is used to locate the intersection points between four squares on the checkerboard; these intersection points make up the set of points referred to as the image points (X_i, Y_i). Because the coordinates of these points in physical space is known (X_p, Y_p), two quadvariate quartic functions can be fitted to obtain X_p and Y_p from a set of two image points. This method is used to convert the images and surface profiles from pixel to physical coordinates, rectify the images to an orthogonal coordinate system, and correct for any spherical aberations. A sample of the detected image points for the three cameras is shown in Figure 2.15 and the rectified images resulting from this calibration processes shown in Figure 2.16 (a).

As mentioned previously, the three cameras have slightly overlapping fields of view. The image points shared between each pair of side-by-side cameras is shown in yellow in Figure 2.15. Using the calibration process described in the previous paragraph, the shared image points can be used to stitch the three camera fields of

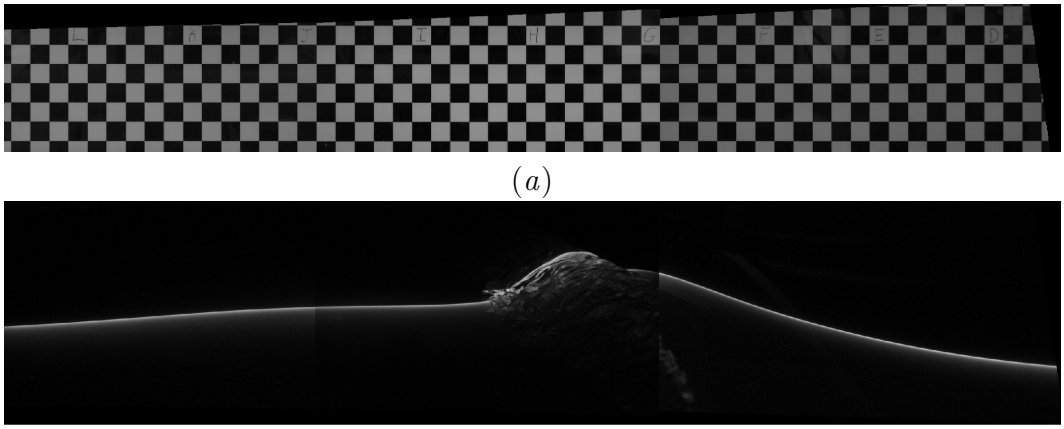

(a)

(b)

Figure 2.16: Stitched images from the three camera fields of view, covering a spanwise distance approximately 1300 cm at a spatial resolution of 180 μm/pixel, of the calibration board shown in Figure 2.15 and surface profile images shown in Figure 2.14.

view together and convert the stitched image to physical coordinates. Figure 2.16 shows stitched images of the calibration board shown in Figure 2.15 and surface profile images shown in Figure 2.14. This calibration and stitching process can be applied to both surface profiles (lines) or images. It should be noted that the stitching process does not always produce a smooth transition from one image or surface profile to another. This is especially noticeable when the free surface becomes rough and 3D structures appear in the foreground. In this case, since the two adjacent cameras have slightly different perspectives, the measured surface profile can create discontinuities in the detected stitched surface profile due to different line of sight blocking in the camera's field of view. Another reason could be errors in making the calibration board parallel to the laser lightsheet, thereby causing a mismatch between image and physical coordinates for adjacent cameras.

2.3.4 Humidity and Drop Evaporation

The relative humidity (measured approximately 25 cm from the water surface) and the ambient temperature in the lab were measured in order to ensure that the smallest measurable drop (d = 100 μm) does not evaporate by a significant amount by the time it reaches the measurement plane. The humidity and temperature measurements were used as input into a drop evaporation model to ensure that drop radius remains relatively constant. It was found that the humidity in the air over the water was no lower than 55 %, with an ambient temperature of approximately 20 °C ± 1 °C.

These measurements were used as input into the drop evaporation model for fresh water that was presented in Andreas [1989]. Figure 2.17 shows the normalized drop radius vs. time on a semi-log plot for three drops of different initial diameter. The red curve is for a drop of d = 100 μm, blue for d = 200 μm, and green d = 400 μm. The plot shows that after 10 seconds, the smallest drop, with an initial diameter of d = 100 μm, decreases about 0.05 percent of its original radius due to evaporation. Therefore it was deemed that the smallest measurable drop, which have a typical speed of 0.65 m/s and reach the measurement plane in 50-90 ms, do not evaporate significantly by the time they reach the measurement plane. Table 2.2 shows the physical parameter inputs used to simulate the drop evaporation.

Table 2.2: List of parameters used as input to the model by Andreas [1989], which simulates drop evaporation.

Parameter	Value	Unit
Water Temperature	°C	18
Air Temperature	°C	20
Atmospheric Pressure	hPa	1013.25
Relative Humidity	-	50
Molecular Weight of Water	kg/mol	18.0160e-3
Molecular Weight of Air	kg/mol	28.9644e-3
Specific Heat of Air (const. pressure)	J/kg/°C	1.006e3

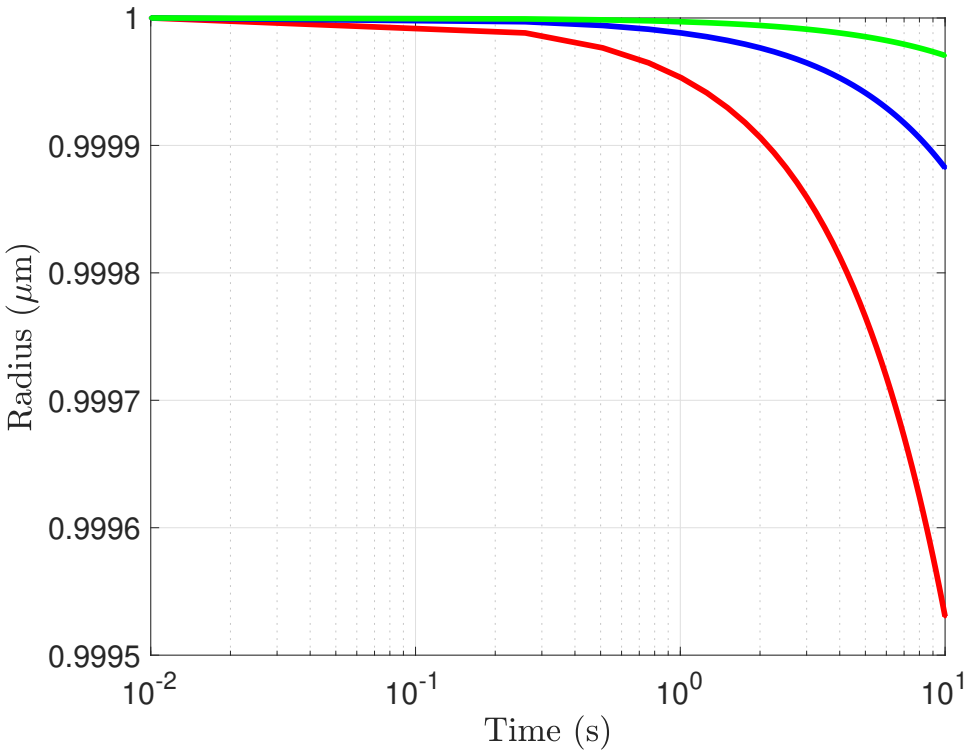

Figure 2.17: Evaporation model for d = 100 micron (red), d = 200 micron (blue), and d = 400 micron (green) for fresh water and 50 percent relative humidity.

2.3.5 Surface Tension Measurements

The static surface tension for the weak and strong plunging breakers were originally measured by Dan Wang in 2012. The static surface tension measurement process is reported in her proposal Wang [2012], but is briefly repeated in this section for completeness. The static surface tension for the weak and strong experiments was measured using a Wilhelmy Plate Tensiometer from NIMA with a 3 L water sample taken from the tank just before the experiment was conducted. Before each measurement the beaker is cleaned and filled with water from the tank. The beaker is skimmed for about 15 minutes by continuously overflowing the beaker with water siphoned from the tank. Just before the measurement, the siphon is stopped and the static surface tension is measured for about 30 minutes.

For the moderate breaker the surface tension isotherm was measured using a Langmuir trough (KSV Nima). Just after the first and last run of each day, a sample of water is collected from the wave tank in a 500 mL beaker and transferred into the Teflon trough. The Teflon trough and barriers were previously thoroughly cleaned with soap and tap water and rinsed with tap water. As a final step to the cleaning process, the trough and barriers are rinsed in the wave tank just before the surface tension isotherm is measured. The surface tension is measured by a platinum Wilhelmy plate that makes contact with the water sample (forming a meniscus) and is suspended on an electronic balance that measures the downward pull (surface tension) of the water sample. The isotherm is measured when two Teflon barriers compress the water surface, thereby causing any surface surfactants

in the water sample to be compressed, in turn lowering the surface tension. A sample plot of seven different surface tension vs. surface compression measurements is shown in Figure 2.18.

The red curves in Figure 2.18 shown the surface tension isotherm for tank water that was not properly filtered (hence forth referred to dirty water) and the blue curves are for properly filtered tank water (referred to as clean water). The static surface tension (the surface tension at 0% compression) for both samples is close to the surface tension of clean water. However, as the surface is compressed, the surface tension for the red curves decreases significantly, up to a 16 mN/m difference, at about 70% compression while the blue curves change at most 1 mN/m at 90% compression. The blue surface tension isotherms are from water samples collected from the wave tank after the water filtration systems (incoming water filters and diatomaceous earth filter) were cleaned.

It was found that certain wave features like wave crest speed, jet impact speed, and jet impact location, for breakers generated in dirty water were not consistent from run to run. Therefore, having relatively clean water was deemed important to experimental repeatability. For the droplet measurements for the moderate breaker and the profile measurements for the three waves, the water quality was maintained as close as possible to the blue curves in Figure 2.18. Although the surface tension isotherms were not measured for the droplet measurements in the weak and strong breakers, the water quality and filtration systems were maintained in a way that's consistent with the clean water quality obtained for the moderate breaker. Additionally, wave features like wave crest speed, jet impact speed, and jet impact

location, from the weak and strong breakers are consistent from run to run and consistent with experiments of the same waves conducted just before the experiments for the moderate breaker. Therefore, it was deemed that the water surface tension quality between the two experiments was similar.

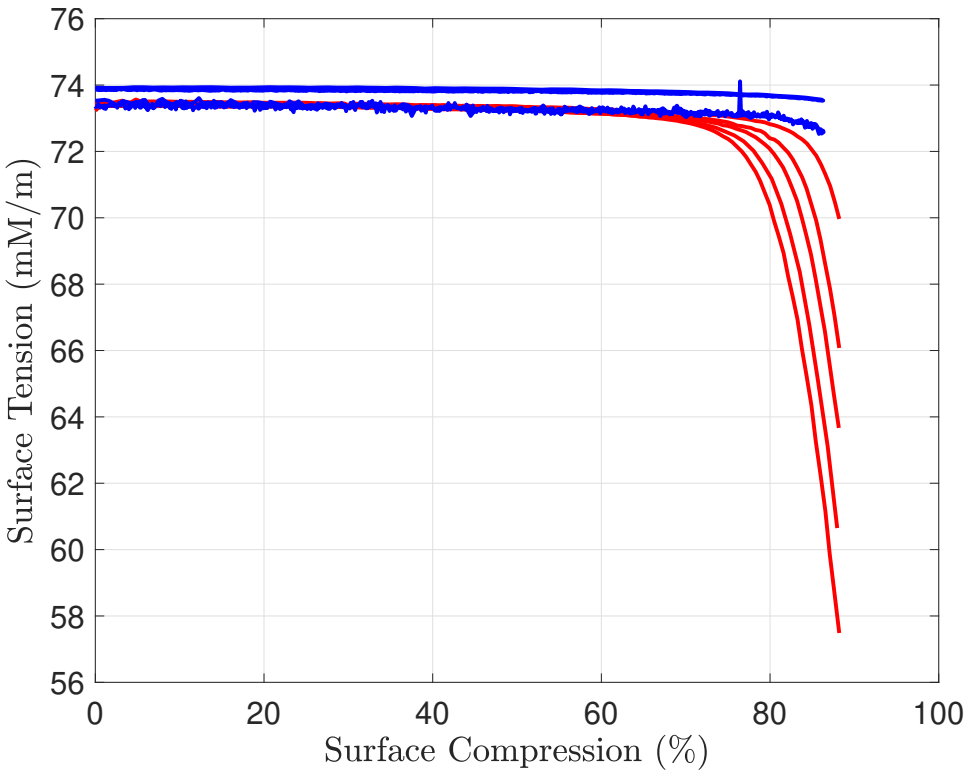

Figure 2.18: Surface tension isotherms of wave tank water from seven measurements from different days. The five red curves show the surface tension isotherms that was deemed dirty because of a significant drop in surface tension after about 70% compression. The blue curves show the water quality in the same wave tank after the filtration system was cleaned. The quality of the water was deemed important for the repeatability of the experiment. Therefore, the surface tension isotherm for the water used in the moderate breaker droplet measurements and all profile measurements was maintained as close as possible to the blue curves.

Chapter 3: Results and Discussion

In this chapter, experimental results of spray produced by mechanically generated breaking waves in laboratory scaled experiments are presented. Simultaneous spatially and temporally resolved measurements of the breaker crest profile evolution and similarly resolved measurements of drops ranging in radius down to 50 μm are reported and discussed for plunging breakers of weak, moderate, and strong intensities.

In the first section of this chapter (section 3.1), spray generation mechanisms by the weak plunging breaker are reported in great detail and linked to wave breaking sub-processes in three distinct spatial and temporal zones of drop production. In the second section (section 3.2.2), drop statistics and mean breaker profiles are compared for the three breakers. The mean surface profiles are found to be highly repeatable and share common features between the three breakers. The relative importance of the three spray generation mechanisms identified in section 3.1 are reported for all three breakers. The droplet probability distribution for the three waves follows a separate power law scaling for large and small drops and varies with breaker intensity.

3.1 Spray Generation Mechanisms by a Plunging Breaking Wave

In this subsection, breaking profile and drop production measurements for the weak breaker are presented and discussed in detail. The measurements are taken simultaneously during many repeated breaking events, and the time, location, and drop characteristics of the various drop generation events during the breaking process are identified from the data. Some of the work presented in this section was published (in a slightly modified form) in Geophysical Research Letters [Erinin et al., 2019]. Figures and text from the paper are cited where appropriate.

During a breaking event, drops are generated by small-scale interfacial motions with length scales on the order of the typical drop size. These motions are in turn generated by the large-scale motions of breaking, for example jet impact, with length scales on the order of the wave height. The waves studied in this research are highly repeatable and nearly two-dimensional up until the instant that the plunging jet collides with the front face of the wave. After this point in time, the flow becomes turbulent and, while the large-scale features found in the profile evolution averaged over an ensemble of repeated breaking events is repeatable and probably two-dimensional, the small-scale features of the flow are three dimensional and vary significantly from run to run. The interfacial features produced during the breaking process that are relevant to drop generation are discussed in the following paragraphs.

The evolution of the breaking process and the small- and large-scale motions are exhibited in the water surface profile sequence and LIF images presented in

Figure 3.1(a) and (b), respectively. The profiles and images were taken from the same high-speed LIF movie and the bold profiles in (a) were obtained from the corresponding images in (b). The images show some drops; however, it is important to keep in mind that for a drops to be visible as a bright spot in the LIF images, it must be relatively large and be positioned within the 1-mm-thick laser light sheet. Instead, drops are measured using in-line holography, which can measure drops with positions across the entire width of the tank (1.15 m wide) and with radii down to 50 μm. Thus, the number of drops seen in the typical holographic image is much larger than the number visible in the 1-mm-thick laser light sheet region of the LIF images coincident with the hologram location.

The surface profiles are first used to characterize the breaker through the measurements of the geometry and speeds of the crest region during jet formation and through the measurements of plunging jet speed and geometry during the time just before jet impact. One significant time during this incipient breaking period is the moment when the plunging jet begins to form. At this point in time, a small region near the crest on the front face of the wave becomes vertical. When this condition is reached, the measured wave crest speed (the horizontal speed of the highest point on the crest region) is 1.37 m/s and the the maximum wave crest height is 10.28 cm above the still water level. A second significant time is the moment just before the plunging jet collides with the front face of the wave. At this moment, the wave crest speed has dropped to 1.29 m/s and the maximum wave crest height has risen to 12.2 cm above the free surface. Also, the jet tip speed is 1.63 m/s just before impact and the location of the jet tip impact point is 4.3 cm horizontally ahead and

5.67 cm vertically down from the wave crest point. Qualitatively speaking, this is a weak energetic plunging breaker since the jet impact point is only about half the distance vertically down from the crest to the still water level. Regarding the small decrease in crest speed while the jet is plunging, it is important to keep in mind that the crest region has a relatively large radius of curvature and is constantly changing in shape. These factors make it difficult to define, measure, and interpret the phase speed.

The sequences of profiles and images in Figure 3.1 (a) and (b), respectively, depict the breaking event as follows. Image (i) was taken a short time after the plunging jet collided with the water surface upstream of the crest and a region of splash has formed upstream (to the left) of the jet impact point. During the period between the plunging jet impact (the first profile in (a)) and the first bolded profile corresponding to image (i)) the leading edge of the splash region advances with a speed of 1.86 m/s, as estimated from the profile sequence. At about the time between images (i) and (ii), the speed of the leading edge of the first splash slows down to 1.07 m/s. As the splash region continues to evolve, the sharp indent at the location of the boundary between the upper surface of the jet and the back surface of the splash remains distinct. In images taken with the camera placed to the right of the camera position for the images shown in Figure 3.1(b), one can see that this indent is actually a narrow crater that extends below the apparent free surface seen in images (ii) and (iii). In Figure 3.1(a), the location of the point of maximum height on each profile is marked by a red triangle. This point is initially the wave crest, but later transfers to the first splash. The speed of the highest profile point is

0.944 m/s when it is on the wave crest during the jet plunging process but is 0.896 m/s when it is on the first splash. Between the images (*ii*) and (*iii*), the leading edge of the splash first slows down and then speeds up. During the speed up period, a second splash springs forward and between images (*iii*) and (*iv*), the highest point on the profiles transfers to this second splash. The motion of the highest point among the various features of the breaking event is consistent with the idea of the wave continuing to propagate through the breaker-generated turbulent vortical flow field. This patch of turbulent flow moves with the surrounding water flow field, which typically has speeds on the order of the wave slope times the phase speed.

Following the indent between the upper surface of the plunging jet and the back face of the first splash, one can see an eruption at about the time of image (*iii*). By the time of image (*iv*), many ligaments and drops appear to issue from this point in the images. These processes are visible in the surface profile plot as well. This eruption involves the appearance of large bubbles and the rupture of their surface films. The process of the crater collapse and film popping is, of course, related to the canonical experiments of single bubbles popping at the surface of a quiescent pool but is much more complicated due to the non-axisymmetric geometry and three-dimensional turbulent free surface flow that accompanies the process [Erinin et al., 2019].

A primary statistic indicating the drop production during the above-described breaking process is $N(x,t)$, the number of drops moving up across the measurement plane per unit time (Δt) per unit streamwise distance (Δx) per meter of crest length per breaking event. This function is measured experimentally and shown as

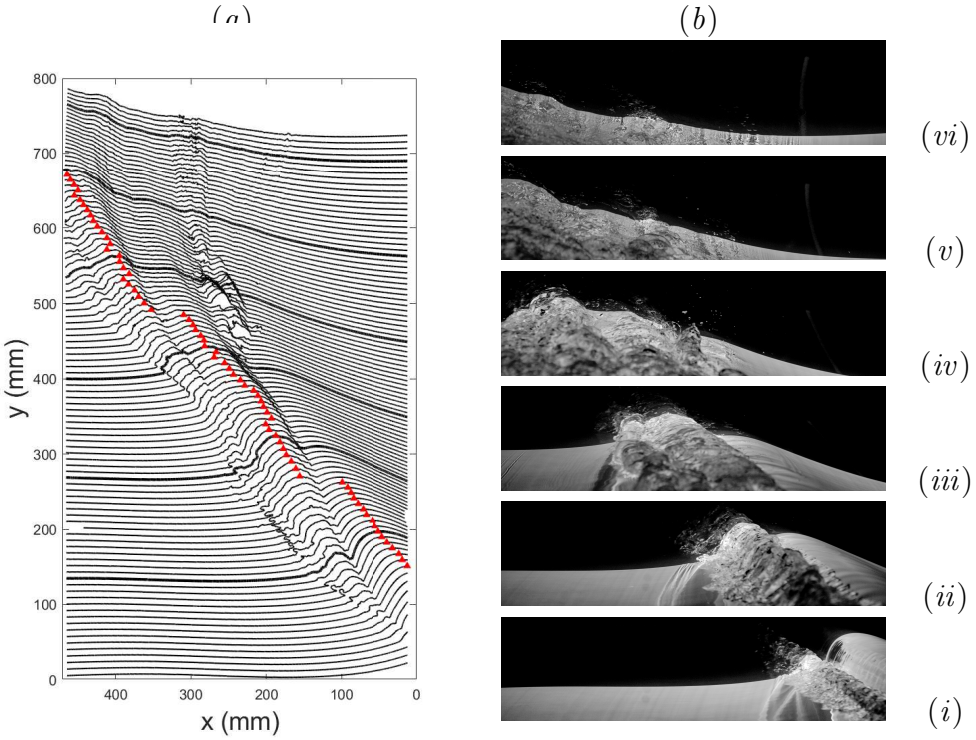

Figure 3.1: Water surface profiles (a) and images (b) from an LIF movie of the breaker used in this study. Each profile in (a) is obtained from one image in the LIF movie. The movie was taken at 650 pps ($\Delta t = 0.00154$ s) but only every fourth profile ($\Delta t = 0.0062$) is shown in (a). Each profile is plotted 8 mm above the previous profile for clarity. The first profile in the sequence was recorded 0.0077 s after the plunging jet hit the front face of the wave, $t = 0$ s, and the last profile was taken at $t = 0.6154$ s. The red filled triangles mark the position of the highest point on each profile. The sequence of bold profiles in (a) corresponds to the sequence of images in (**b**). This figure was originally published in Erinin et al. [2019].

a contour plot on an x-t plane in Figure 3.2. Interpolating the drop data spatially and temporally from at least ten experimental runs at each measurement location, it is estimated that 653 drops per breaking event are produced. There are two large regions of drop production, measuring about 600 mm long and 0.3 s high, (labeled region I and region II). Since the measurement plane is 1.2 cm above the maximum wave crest height, there is a time delay between the moment that a drops is generated and when it is measured. Using the synchronized drop and profile measurements along with a simple drag model for a solid sphere moving in stationary air [Cheng, 2009], the average time of flight between the surface and the measurement plane is estimated to be between 40 and 70 ms. The effect of the air flow induced by the breaker is estimated to be large (particularly for the smaller drops), but, since air flow measurements were not attempted, this effect is not included in the model at this time. The drop radius decrease due to evaporation during the time of flight was estimated via the theory of H.R. Pruppacher [1978]. Using a relative humidity of 50% (estimated as a minimum value from later measurements), it was found that the decrease in drop diameter would be less than 4% after one second for a drop with an initial radius of $r = 50\mu$m, and therefore insignificant for the 70-ms flight time found here.

In region I of the contour plot of $N(x,t)$ in Figure 3.2, there are three prominent local maxima. The first, which is the most intense, is located in the vicinity of the point $(x,t) =$ (140 mm, 0.18 s). By examining the corresponding region below profile (ii) in the profile history plotted in Figure 3.1 (a), it can be seen that this region of high drop number production is associated with the initial jet

impact and resulting splash. The second local maximum occurs at approximately $(x, t) = (325$ mm, 0.275 s) and this point is in the region of the second jet impact and splash, roughly along profile (iii) in Figure 3.1 (a). The peak value of N at this location is about 46 percent of that at the first local maximum. The third local maximum occurs in the vicinity of $(x, t) =$(275 mm, 0.38 s) and is associated with closing of the impact crater and the sudden eruption of large air bubbles, between profiles (iii) & (iv). The large bubbles that come to the surface and pop are probably from the air entrapped under the plunging jet during impact and as the impact crater closes. The drops generated in Region II occur after the main breaking process has subsided. From the LIF profile movies it appears that these drops are generated by small bubbles that rise to the surface and eventually pop [Erinin et al., 2019].

In order to analyze the drop generation data further, the measured function $N(x, t)$ was integrated over all x to obtain the number of drops generated per unit time per unit crest length, $N_x(t)$, and integrated over all t to obtain the number of drops generated per unit x per unit crest length, $N_t(x)$:

$$N_x(t) = \int_0^{1.05 \text{ m}} N(x,t)dx, \tag{3.1}$$

$$N_t(x) = \int_0^{2.0 \text{ s}} N(x,t)dt. \tag{3.2}$$

A plot of $N_x(t)$ is presented in Figure 3.3(a) and to the right of the contour plot in Figure 3.2. This function has three local maxima, found at approximately $t = 0.18$,

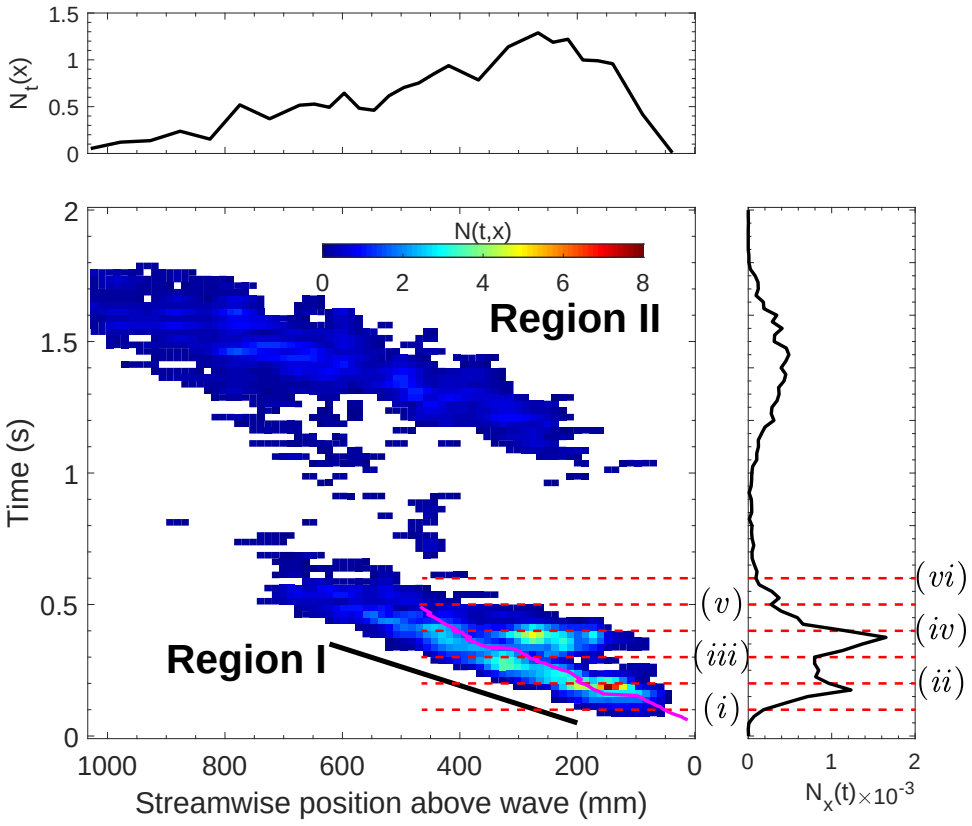

Figure 3.2: Contours of $N(x,t)$, the number of drops with $d \geq 100$ μm generated per breaking event, per $\Delta t = 0.025$ s, per $\Delta x = 13.02$ mm, per crest length, plotted on an x-t plane. The black line is drawn with a slope of 1.7 m/s. The bolded free surface profiles and images in Figure 3.1 (a & b) correspond to the red lines on the lower right corner of the contour plot. The magenta line corresponds to the maximum wave crest height from Figure 3.1. The plot on the right is N_x, the number of drops generated per unit time per crest length, vs time. The plot on top is N_t, the number of drops generated per mm in the streamwise direction per unit crest length, vs steamwise position. This figure was originally published in Erinin et al. [2019].

0.38 and 1.40 s after initial jet impact. The three LIF images in Figure 3.3 of the breaker in each of the columns, (A), (D) and (G), were taken around the times of these local maxima, respectively. From the images, one can see that the first local maximum occurs at the time of the growth of the first splash ahead of the plunging jet impact point. The number of drops produced in the first peak accounts for about 22% of the total number of drops measured. The second local maximum occurs at about the time when the top surface of the jet collides with the back surface of the first splash and results in the impact-crater eruption (from $0.25 < t \leq 1.00s$), this region accounts for 44% of total drops. Finally, the third maximum occurs at later time when the surface is relatively free of breaking crest features and entrained bubbles appear to come to the surface and pop. The number of drops produced in the third peak accounts for 34% of the total drops.

The plot of $N_t(x)$ in Figure 3.3(b) and on top of the contour plot in Figure 3.2, has a simpler structure with one maximum at about $x = 0.2$ m. The position of the maximum corresponds to the general location of the splash and the large bubble eruption along the impact crater. The fact that $N_t(x)$ goes to zero on both ends of the plot is consistent with the observation during the experiments that no drops reach the measurement plane upstream or downstream of this 1.0-meter-long measurement zone.

Figure 3.4 shows the mean drop speed vs. drop radius. The speed of each drop is measured from the x and y velocity components, $u(y)$ and $v(y)$, as the drop passes through the measurement plane. The components u and v are obtained by fitting a second order polynomial to drop tracks where the speed $s = \sqrt{u^2 + v^2}$. In

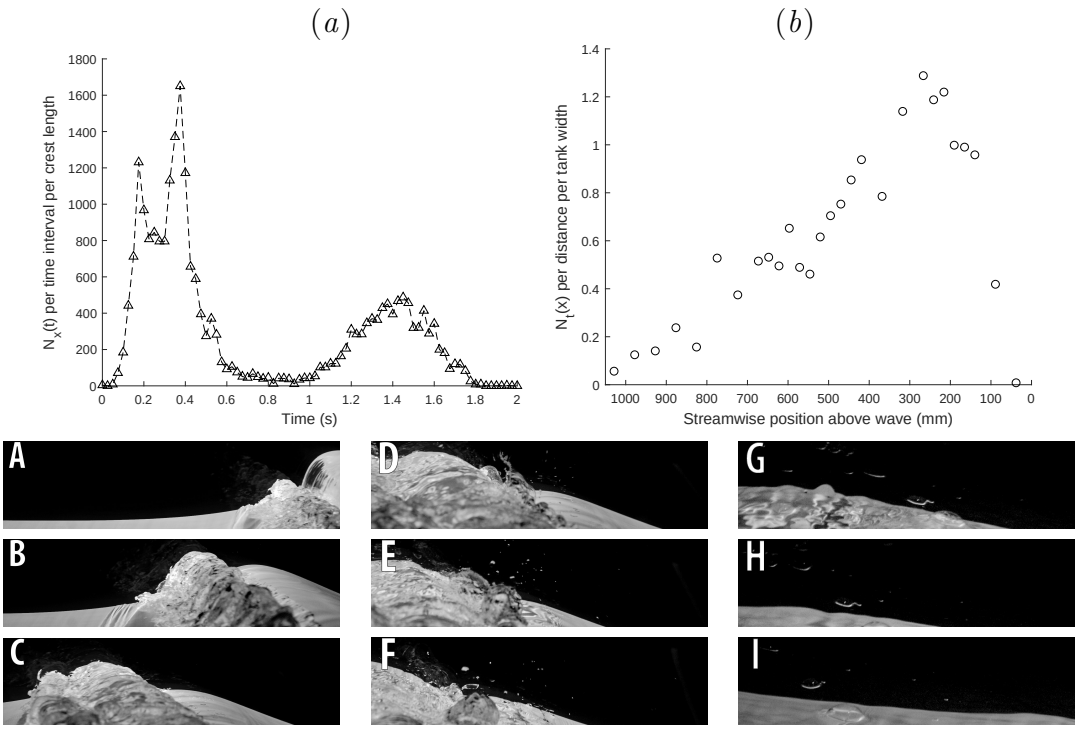

Figure 3.3: (a). Plot of the number of drops generated per breaking event ($N_x(t)$) per time interval $\Delta t = 0.025$ s, per tank width $\Delta y = 1.05$ m. (b). Plot of the number of drops generated per breaking event ($N_t(x)$) per distance interval $\Delta x = 21.6$ mm, per tank width $\Delta y = 1.05$ m. These two plots are the data in Figure 3.2 integrated over x and t, respectively to yield a total of 539 drops per breaking event. (c). Images (a-c) show the free surface from $t = 0.1$ s to 0.3 s with $\Delta t = 0.1$ s between each image. Images (d-f) show the free surface from t = 0.334 s to 0.435 s with Δt = 0.051 s between successive images. Images (g-i) show traces of bubbles on the free surface from t = 1.5 s to 1.7 s with $\delta t = 0.1$ s between successive images.

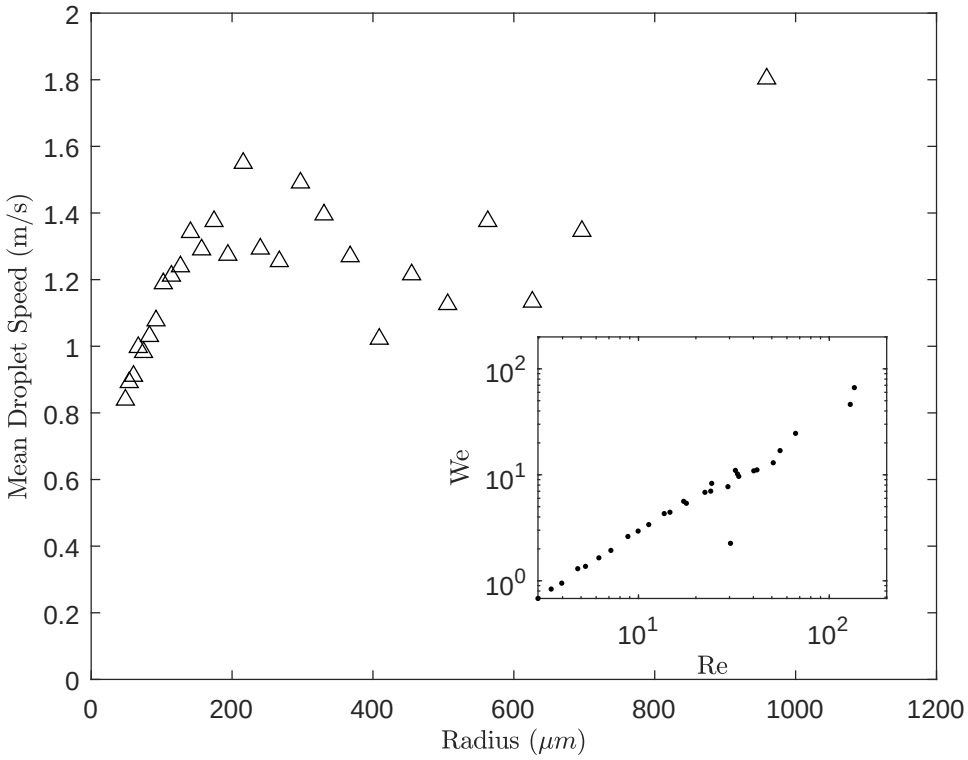

Figure 3.4: Mean drop speed as a function of drop radius plotted on a logarithmically spaced bin ranging from $r = 50$ to 1500 μm with a total of 32 bins. The mean drop speed is calculated from the x and y velocity components as the drop passes through the measurement plane.

the plot, a logarithmic spacing for dr is used with a total of 32 bins ranging from $r = 50$ to 1500 μm.

It was found that the cross stream velocity component, v, was typically $v \leq 15$ percent of the drop speed. The mean drop speed increases from about $s = 0.8$ m/s for $r = 50$ μm to about 1.4 m/s at $r = 250$ μm; from there to higher radii the local average remains fairly constant. The increased variation in mean speed at larger radii is at least partly due the small number of large drops, as mentioned previously. The average speed of all drops is 1.07 m/s.

Figure 3.5 shows the distribution of drop trajectory angles (θ) as measured in

the streamwise-vertical $(x-y)$ plane when a drop passes through the measurement plane. In the following, an angle of 0° indicates a drop is moving horizontally downstream, while an angle of 90° indicates a drop is moving vertically up. Subplot (a) contains the data for all drops measured during the entire breaking event. The mean drop angle is 73.9°, i.e., approximately 26° downstream from vertical, with a standard deviation of 36.4°.

Subplot (b) contains data from drops passing through the measurement plane in the time range $0.325 < t < 0.5$ s and the position range $0 < x < 0.33$ m. This region is intended to capture the drops that are generated by the collapse of the crater between the back face of the first splash and the upper surface of the plunging jet. The average velocity is essentially vertical, $\overline{\theta} = 87.9°$ with a standard deviation of 41.3°.

The drops considered in subplot (c) are the difference between the drops measured from all streamwise positions during the period from $0 < t < 0.8$ s and the drops from $0 < x < 0.33$ m and $0.325 < t < 0.5$ s. This region is intended to capture the drops generated by the turbulent region generated by the plunging jet impact. The average drop velocity was 23.7° downstream from vertical, $\overline{\theta} = 76.3°$, with a standard deviation of 39°.

Finally, subplot (d) includes drops from all streamwise positions appearing after $t > 0.8$ s. This region is intended to capture the drops resulting from the third peak in the drop production curve shown in figure 3.3(a), which is believed to result from late time bubble popping at the free surface. The drop velocities in this region have a mean angle of 71.7° with a standard deviation of 29.6°. It was initially

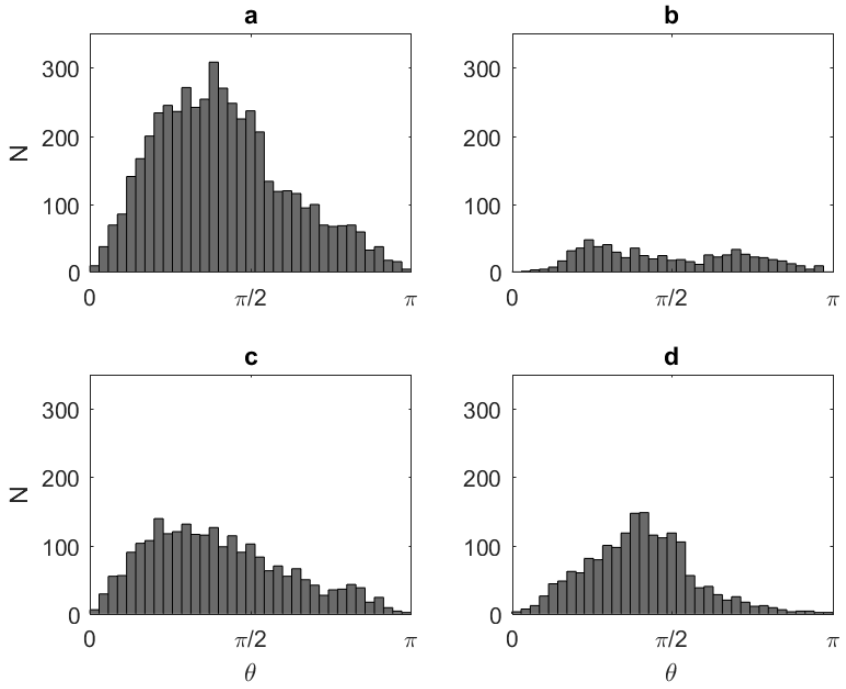

Figure 3.5: Histograms of drop angles (θ, from 0 to π, where 0 is horizontal in the direction of wave motion) for all drops at various stages during the breaking processes as they pass through the plane 1.2 cm above the maximum wave crest height. (a) shows the distribution of drop angles for the whole measurement region. (b) show the distribution of drop angles from $0 \leq x \leq 12.5\,cm$, $0.325 \leq t \leq 0.5\,s$. (c) show drop angles from $0 \leq t \leq 0.8s$ excluding drops from $0 \leq x \leq 12.5\,cm$, $0.325 \leq t \leq 0.5\,s$. Finally, (d) shows all drop angles after $t > 0.8s$.

thought that these drop velocities would be evenly distributed about vertical since their source appears to be small popping bubbles in the latter phase of breaking where the water surface is much smoother than in the earlier phases. The measured angle indicates that motion of the free surface and/or the underling flow must play a role in determining this angle.

Further identification of the breaker features associated with drop production is provided by the plots in Figure 3.6. The plot in subfigure (a) shows the profile of the breaker crest as it evolves in time (the same data shown in Figure 3.1) with

colored dots plotted at the measured position and time when a drop crosses the measurement plane. It should be kept in mind that these drops were measured over a total of 160 unique realizations of the breaker, while the profiles are from a single run, i.e., a single breaking event. The vertical bands with no drops in Figure 3.6(a) appear at locations where drop data was not collected. The plotted drops in subfigure (a) are concentrated in two regions. The first is near the rough region created by the jet impact, advancing from the right to the left and running diagonally on the plot. The second concentration of drops is located in the vicinity of the impact of the back face of the first splash with the upper surface of the plunging jet. As discussed above, drop velocities are primarily up and with a smaller component in the upstream or downstream direction. Thus, the positions and times of the generation of the drops are not those marked in Figure 3.6(a). The distance and direction of the drop generation point on the water surface relative to the marked position of each dot on the plot should vary from drop to drop.

In an effort to get an approximate $x-t$ position of the generation point of each drop, a model of the drop motion was used along with the measured drop velocities and positions at the measurement plane. In this model, the forces of gravity and drag relative to still air are considered and the equations of motion are:

$$m_d \frac{\mathrm{d}^2 X_d}{\mathrm{d}t^2} = C_d \frac{1}{2} \rho_a \left(-\frac{\mathrm{d}X_p}{\mathrm{d}t} \right) \sqrt{\left(-\frac{\mathrm{d}X_p}{\mathrm{d}t} \right)^2 + \left(-\frac{\mathrm{d}Y_p}{\mathrm{d}t} \right)^2} \tag{3.3}$$

$$m_d \frac{\mathrm{d}^2 Y_d}{\mathrm{d}t^2} = C_d \frac{1}{2} \rho_a \left(-\frac{\mathrm{d}Y_p}{\mathrm{d}t} \right) \sqrt{\left(-\frac{\mathrm{d}X_p}{\mathrm{d}t} \right)^2 + \left(-\frac{\mathrm{d}Y_p}{\mathrm{d}t} \right)^2} + m_d g \tag{3.4}$$

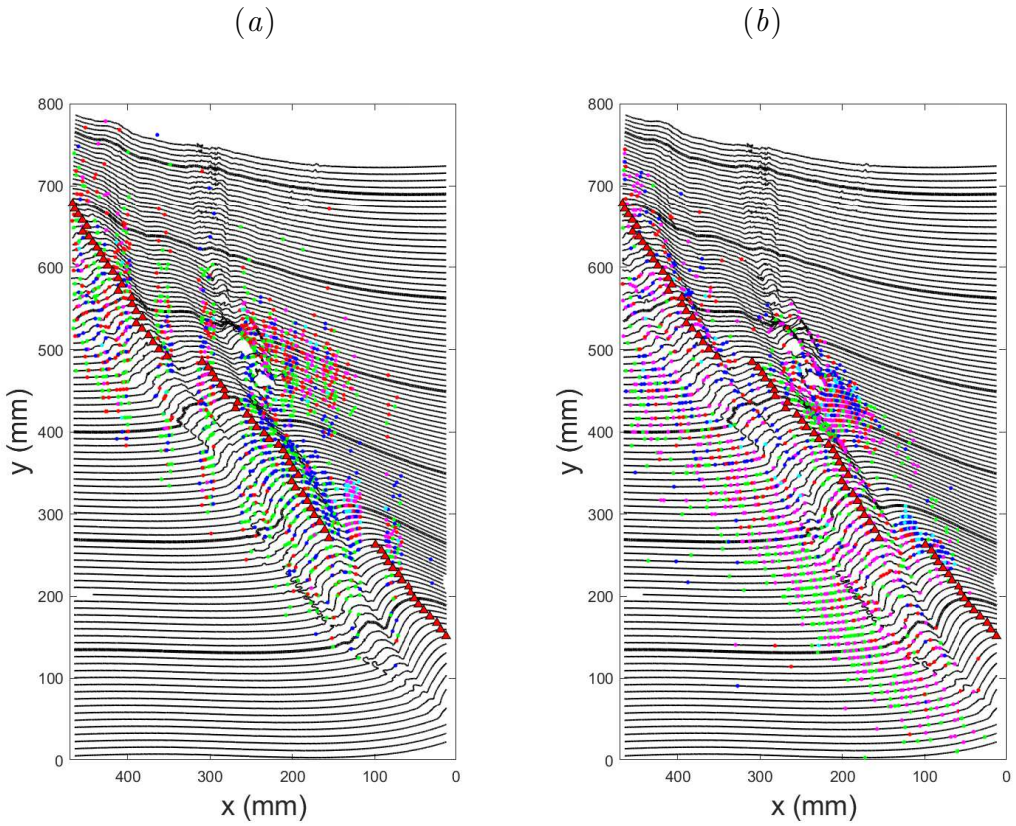

Figure 3.6: Profile history of a breaking event with drop generation locations in time and space. In (a), the dots are located at the x and t where the drops passed through the horizontal plane located 1.2 cm above the highest point reached by the free surface. In (b), the dots are located at the x and t where the drops are calculated to have been generated. This calculation is performed with the data on the drop motion while it is in the measurement window and a ballistic trajectory model for the drop motion. • $800 \leq d$, • $300 \leq d < 800$, • $200 \leq d < 300$, • $125 \leq d < 200$, • $d < 125$ μm.

where

$$Re = \frac{d\sqrt{u_{rel}^2 + v_{rel}^2}}{\nu_a}, \tag{3.5}$$

$$C_d = \frac{24}{Re}(1 + 0.27Re)^{0.43} + 0.47\left[1 - \exp(-0.04Re^{0.38})\right], \tag{3.6}$$

u_{rel} and v_{rel} are x and y components, respectively, of drop velocity relative to the air, d is the drop diameter, ν_a is the kinematic viscosity of air, Re is the Reynolds number of the drop as seen in equation 3.5, C_d is the coefficient of drag (in this case given by Cheng [2009] for a solid spherical particle), ρ_a is the density of the air, m_d is the mass of the drop, and g is the gravitational constant. The assumption of stationary air was used because there were no measurements or calculations of this flow field. This approximation probably causes larger errors for the smaller drops. In the calculations, the drop position is simulated backward in time until it hits the temporally and spatially varying wave profile, which we point out again was measured in a single breaking event and at the center plane of the tank. In spite of the inaccuracies, it seems that the presentation of the results at this stage may be useful. The results are shown in Figure 3.6(b) where the water surface profiles in (a) are repeated but the drop positions are as computed by the backward tracking model. From these simple simulations, it appears that drops are primarily generated from the turbulent region created by the jet impact and from the impact between the back face of the first splash and the top surface of the plunging jet.

The turbulent front region, created by the jet impact and propagating from

right to left, seems to be a major source of drop production since many of the simulated drops project back to the rough surface features created by the jet impact. Meanwhile, the cloud of drops around the impact of the turbulent front region and back face of the wave in subfigure (a) seems to be more concentrated towards the rough surface features when simulated back in time, shown in subfigure (b). As noted above, there are locations in Figure 3.6(a) where drop data was not collected (indicated by the vertical bands where no drops appear). These empty regions undoubtedly have an influence the appearance of Figure 3.6(b). This may be corrected in future work.

The normalized distribution of drop radii for all drops that pass through the measurement plane during a breaking event is shown on a log-log plot in Figure 3.7. The probability distribution was calculated from the data obtained from 10 runs at each of the 28 streamwise measurement locations. In order to obtain this distribution, radius probability distributions are first generated at all 28 measurement locations using the same set of logarithmically spaced radius bins ranging from $r = 50$ μm to $r = 1400$ μm with 26 bins. The number of observed drops in each bin at each location is divided by the number of runs, the width of the bin in microns, the streamwise width of the holographic camera's field of view, and the width of the tank (1.15 m) to obtain the number of drops generated per breaking event per micron of radius per meter of crest length versus streamwise position, x. This function for each bin is then numerically integrated using the trapezoidal rule over the range of x for which measurements were taken. In this way, data at locations where no measurements were taken are approximated by linear interpolation. The verti-

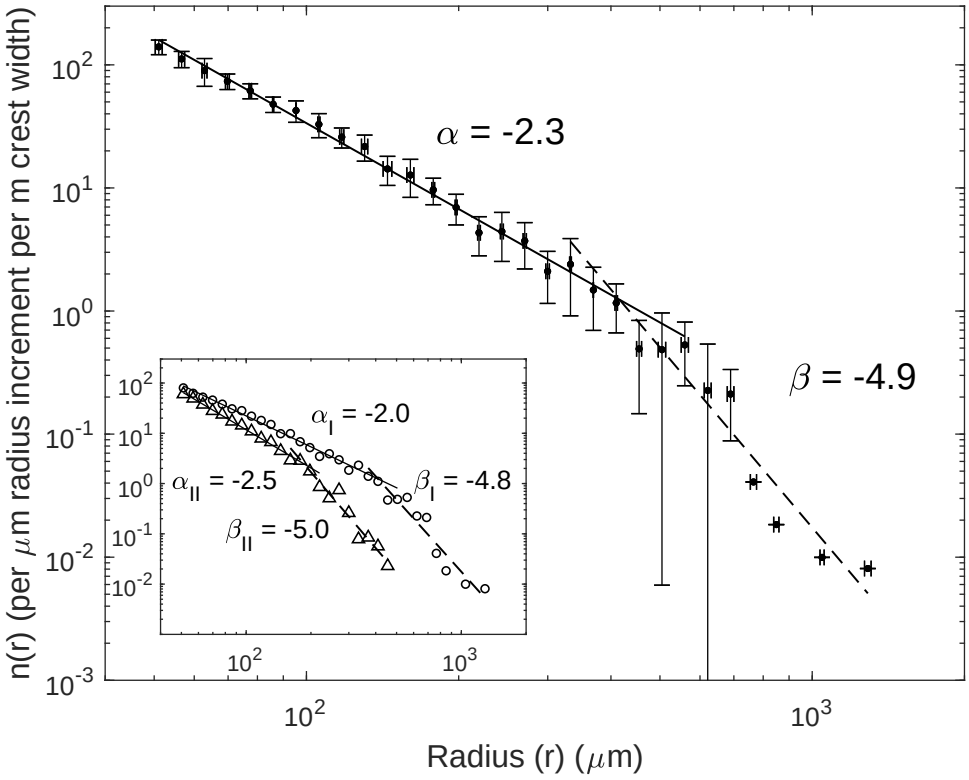

Figure 3.7: Drop radius probability distributions. Vertical error bars show ±1 standard deviation, while horizontal error bars show radius measurement error obtained from a calibration process. The main plot is for all of the drops produced by the breaker while the sub plot contains separate data sets for the drops produced during the jet impact phase (Region I, $0 < t < 0.8$ s, $\circ$) and during the bubble ascend and popping phase (Region II, $0.8 < t < 2$ s, $\times$). A Hinze-scale-like break in slope is identified in all three data sets. The slopes of the distributions for the larger and smaller bubbles in each data set are identified by α and β, respectively. For all the drops, break at $r = 273$ μm. This figure was originally published in Erinin et al. [2019].

cal error bars show ±1 standard deviation, while horizontal error bars show radius measurement error obtained from a calibration process. The four largest radius bins do not have error bars because only one drop was measured in each bin.

This calculation yields an estimate for the total number drops observed per breaking event per micron of radius per meter of crest length in each bin and in Figure 3.7 the result is plotted versus the mean radius for each bin. The probability distribution from all drops is shown in the main plot, while in the inset, separate distributions are plotted for the first (t $<$ 0.9 s) and second (t $\geq$ 0.9 s) drops production regions in Figure 3.2. In all three data sets, separate straight lines were fitted by least square error minimization to the smaller diameter and larger diameter drop data.

The boundary between the larger and smaller radius groups was determined by an iterative bisection-like routine outlined as follows: first, an initial guess for the break in slope, r_0, is estimated, the data is split into two distinct sets and a power law, of the form described above, is fitted to each set. The radius where the two lines intersect, r_i, is found. If the difference between r_0 and r_i does not fall within a specific tolerance (in this case $r_{tol} = 1$ μm), a new guess for r_0 half way between the previous values of r_0 and r_i is assigned and the processes is repeated until the tolerance is reached.

The break in slope occurred approximately at the Hinze scale Hinze [1955] that is computed using the turbulent dissipation rate to determine the velocity scale in the wind field. This indicates that the wind plays an important role during the drop generation, which is quite different from the drop generation mechanisms shown

herein with a mechanically generated breaking wave in the absence of wind.

It should be noted that this determination of the "Hinze" radius is inherently inaccurate because there are only a few drops in each bin at the larger radii. This is a classic problem in bubble and drop measurements and to emphasize this inadequacy, the line for the fit to the drops with larger radii is drawn as a dashed line. In a laboratory wind wave system, Wu et al. [1984] measured the drops size distribution at several heights above the mean water level. The measurements were made over long periods of time and no correlation with breaking events was attempted. The distribution has a shape that is qualitatively similar to the one shown here Erinin et al. [2019].

3.2 Comparison of Spray Generated by a Weak, Moderate, and Strong Intensity Plunging Breakers

In this section, mean breaking profiles and drops characteristics generated by the three plunging breaking waves are presented and discussed. For each of the three breakers, the mean breaker profiles are calculated from 10 breaker realizations at each instant in time. The three breakers are characterized by their mean geometric features, such as wave crest and jet impact speed (see Table 2.1). When aligned to the plunging jet impact location in space and time, the breaker profiles are found to be highly repeatable and share common features throughout the non-linear wave breaking process. Drop statistics, including the spatio-temporal distribution of drops, number of drops produced per breaking event, and drop probability distri-

butions are reported and discussed for the three breakers. Surface profile and drop data presented in this section are shown in red for the weak, blue for the moderate, and green for the strong breaker. The weak breaker drop data presented in this section is the same as the one reported in the previous section.

3.2.1 Surface Profile Measurements

The surface profile histories are first used to characterize the three breakers as they approach the point of jet impact. To this end, two quantities were extracted from the profiles: the horizontal speed of the highest point on the wave crest profile at the time when the plunging jet begins to form and the speed of the plunging jet just before impact, denoted as c and V_{jet}, respectively. These quantities are taken from the derivatives of the trajectories of the vertical and horizontal positions of the highest point on the crest (called the crest point), as determined quantitatively from the profiles, and of the jet tip location, as determined by eye from the profiles and images. A sample measurement of the wave crest point (marked by green square) and jet tip location (marked by red triangle) from a single realization of the moderate breaker is shown in Figure 3.8.

The trajectories of the horizontal and vertical coordinates of the crest points, denoted as x_c and y_c, were obtained from the 10 runs for each of the three breakers over the time of jet formation. The individual crest point trajectories ($x_c(t)$ and $y_c(t)$) from the 10 runs are shown in Figure 3.9 (a) and (c), respectively, and the trajectories of the average values ($\overline{x}_c(t)$ and $\overline{y}_c(t)$) are shown in Figure 3.9 (b) and

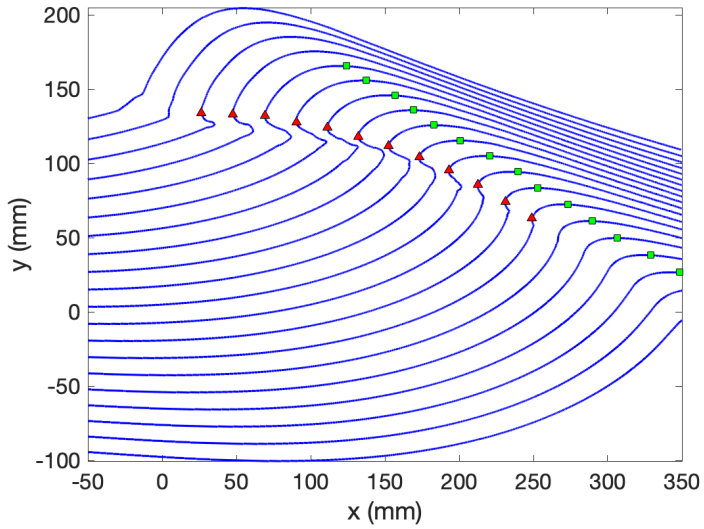

Figure 3.8: Sample measurements of wave crest point, (green square) and jet tip location (red triangle) from one run of the moderate breaker. Each surface profile, shown in blue, is obtained from one LIF image, similar to the ones shown in Figure 2.13. Each successive profile is separated by a time interval of $\Delta t = 0.0123$ s and plotted 10 mm above the previous for clarity. The wave crest and jet tip trajectories form 10 runs for each of the three breakers are shown in Figures 3.9 and 3.10, respectively.

(d). The colored vertical dashed lines in (a-d) were obtained by averaging the time of jet impact over the 10 runs for each breaker, respectively; while vertical error bars in subplots (b) and (d) show ± 1 standard deviation (in mm) of $\overline{x}_c$ and $\overline{y}_c$ from run to run, respectively. The wave crest point trajectories were collected over the time period starting just before the jet starts to form, $t \approx 0.32$ s, and ending shortly after jet impact. This time period is referred to as the jet formation phase in the subsequent paragraphs.

The slope of the trajectory of $\overline{x}_c(t)$ remains nearly constant during the jet formation phase for all three waves, indicating the horizontal speed of the wave crest point (c) is constant. In each time interval, the average and standard deviation is computed over the 10 runs. Averaging these quantities over the 24 time intervals in the plots, yields an average horizontal displacement and standard deviation of $\overline{x}_c(t)$ 16.6 $\pm$ 0.309, 16.4 $\pm$ 0.426, 16.3 $\pm$ 0.596 mm for the weak, moderate, and strong breakers, respectively.

The motion of the wave crest during the jet formation phase is assessed in detail by fitting a second order polynomial to $\overline{x}_c(t)$ using least-squares linear regression. The second order polynomial has the form: $x_c(t) = p_1 t^2 + p_2 t + p_3$ where p_1, p_2, and p_3 are the regression coefficients determined by the fitting. The speed of the wave crest point at time t is given by the first derivative of $\overline{x}_c(t)$, $\overline{c}(t) = \mathrm{d}(x_c(t))/\mathrm{d}t = 2p_1 t + p_2$ and the acceleration (assumed to be constant) by the second derivative of $\overline{c}(t)$, $\overline{a}_c = \mathrm{d}^2(x_c(t))/\mathrm{d}t^2 = 2p_1$. The regression coefficient fits of $\overline{x}_c(t)$ for the three breakers are given in Table 3.1.

The average speed of the wave crest point and standard deviation during the

Table 3.1: The values for the regression coefficients, p_1, p_2, and p_3, used for the second order polynomial fit to $\overline{x}_c(t)$, the position of the wave crest point, for the weak, moderate, and strong breakers. The second order polynomial has the following form $x_c(t) = p_1 t^2 + p_2 t + p_3$. The function fit $x_c(t)$ is used to obtain the velocity and acceleration of the wave crest during the jet formation phase.

Fit coefficient	Weak	Moderate	Strong
p_1	445	348	325
p_2	-1174	-1658	-1635
p_3	887	835	811

jet formation phase is reported in Table 3.3 and was nearly the same for all three waves, measuring at 1.33 ± 0.003 m/s, 1.33 ± 0.002 m/s, and 1.36 ± 0.002 m/s for the weak, moderate, and strong breakers respectively. These measurements can be compared to the wave phase speed predicted by linear deep water wave theory:

$$c_p = \frac{g}{2\pi f} \tag{3.7}$$

where c_p is the wave phase speed, g is the gravitational acceleration constant, and f is the wave frequency. Taking $g = 9.81$ m/s^2, $f = f_0 = 1.15$ Hz the wave phase speed is calculated to be $c_p = 1.357$ m/s. The measured value of the crest point speed (see Table 3.3) are lower than the value obtained by linear wave theory. The measured and theoretical values are not expected to match since Equations 3.7 is from a linear theory for a deep water infinitely long wave train of permanent shape, where as the experiments involve a highly nonlinear temporally evolving wave packet with 32 wave components.

The slope of the trajectory of $\overline{y}_c(t)$, shown in Figure 3.9 (d), is initially constant and upwards from $t = 0.33$ to 0.43 s, displacing vertically by approximately 8 mm for all three waves. During this phase, the speed of $y_c(t)$, measured by the same method

used to measure c_p, is 0.103 m/s, 0.107 m/s, and 0.110 m/s for the weak, moderate, and strong breakers, respectively. Shortly after the start of the formation of the jet, at $t \approx 0.37$ s, $\overline{y}_c(t)$ reaches a local maxima for all three breakers at ≈ 0.43 s. After reaching the local maxima, $\overline{y}_c(t)$ starts to decrease, eventually exhibiting irregular motion shortly after jet impact. The irregular vertical motion of the wave crest point can partly be explained by the fact that shortly after jet impact, the wave motion begins a rapid loss of energy due to energy transfer to turbulent fluid motions.

The trajectories of the horizontal and vertical coordinates of the jet tip point, denoted as x_j and y_j, were obtained from 10 runs of each breaker from moment of jet formation until jet impact. The jet initially forms from a small region on the front face of the wave near the crest as the face there becomes vertical. This condition can be seen in Figure 3.8 just before the first measurement of the jet tip location (red triangle). The time elapsed from jet formation, $t_{j,0} \approx 0.37$ s, to jet impact, $t_{j,i} \approx 0.53$ s is ≈ 0.16 s. The individual positions of the jet tip are determined by eye from the images and measurements of the breaker profiles. Jet tip trajectories, $\rho(x_j(t), y_j(t))$, for from the 10 runs are given in Figure 3.10. It should also be noted that the jet trajectories shown in Figure 3.10 are not adjusted spatially or temporally, and thus the variability of the profiles indicates the repeatability of the breaking event from run to run. The standard deviation of the streamwise jet impact location, where the mean streamwise jet impact location is located at $x = 0$ mm, monotonically increases for the three breakers, from 5.05 mm, 5.63 mm, and 6.66 mm for the weak, moderate, and strong breakers, respectively.

The average horizontal and vertical displacement of the jet tip from jet forma-

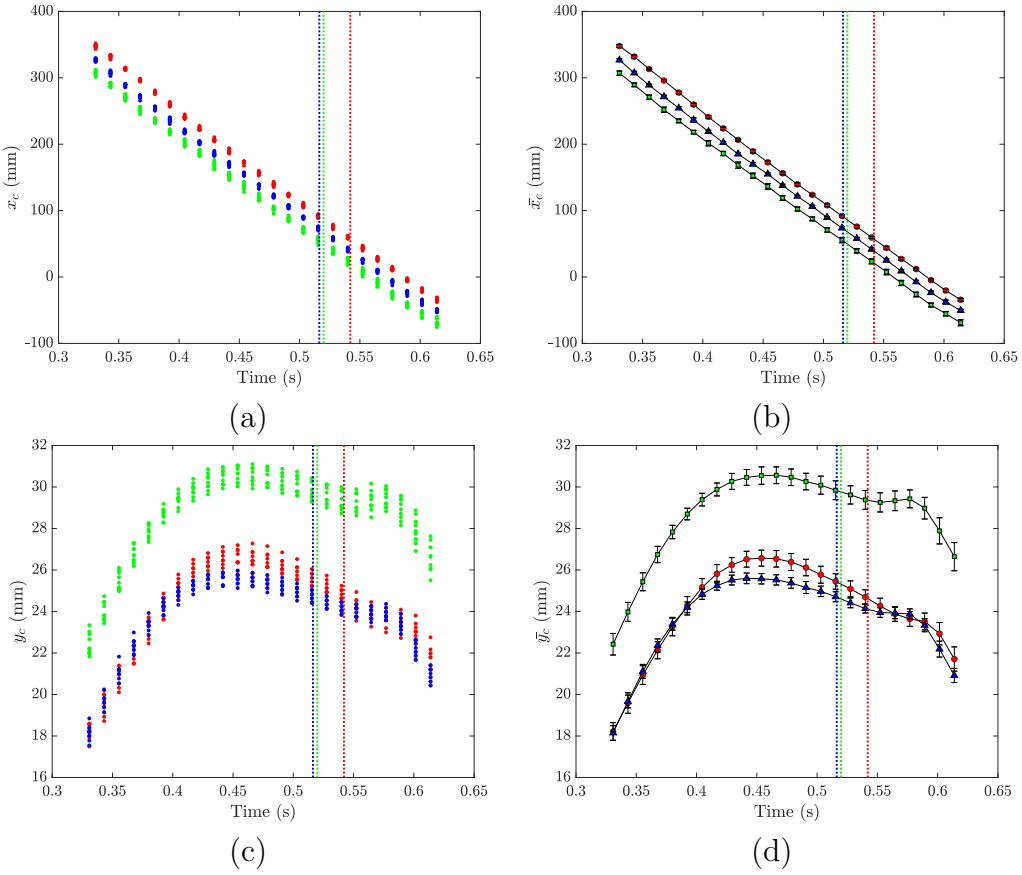

Figure 3.9: The x and y positions vs. time of the wave crest point during the plunging jet formation from 10 runs for the weak, moderate, and strong plunging breakers. The vertical dashed lines indicated the average time of jet impact from the 10 runs for the three waves. The weak breaker is shown in red, the moderate in blue, and the strong in green. The maximum wave crest height from 10 runs for $x_c(t)$ and $y_c(t)$ are shown in (a) and (c) respectively, while (b) and (d) show the averaged position of the wave crest point $\overline{x}_c(t)$ and $\overline{y}_c(t)$ respectively. The vertical error bars in (b) and (d) show ± 1 standard deviation of the x_c and y_c over the 10 runs (which are too small to see in (b)). The wave crest speed reported in Table 3.3 is measured by taking the derivative of $x_c(t)$.

tion to jet impact can be measured from the jet tip trajectories. The total horizontal displacement of the jet tip point is 197 mm, 217 mm, and 257 mm for the weak, moderate, and strong breakers, respectively; while vertical displacement of the jets during the same interval of time is 50 mm, 58 mm, and 61 mm for the weak, moderate, and strong breakers, respectively. During jet impact, a tube of air is entrained by the plunging jet and this tube of air is broken up by the underlying fluid motion, creating bubbles that eventually reach the free surface, pop, and generate drops. The volume of the entrained air cavity is determined by geometric parameters of the jet as described above. Qualitatively speaking, these numbers are consistent with the idea that as the breaker height increases, the jet travels a longer horizontal and vertical distance before impact and entrains a larger cavity of air.

Similar to the analysis carried out for the trajectory of the wave crest point, the motion of the jet tip is assessed by fitting a second order polynomial to the average jet tip position, $\overline{x_j}$ and $\overline{y_j}$ vs. time using least-squares linear regression. The polynomial has a form $x_j(t) = xp_1t^2 + xp_2t + xp_3$ and $y_j(t) = yp_1t^2 + yp_2t + yp_3$ for the x and y jet tip trajectories, where xp_1, xp_2, xp_3, yp_1, yp_2, and yp_3 are the regression coefficients determined by fitting, shown in Table 3.2. The velocity, $u_j(t)$ and $v_j(t)$, and accelerations a_x and a_y, are given by the first and second derivative of $x_j(t)$ and $y_j(t)$ with respect to time, respectively.

The horizontal speed of the jet tip, u_j, moments after the jet begins to form, $u_j(0.33 < t < 0.36s)$, are 1.36 m/s, 1.38 m/s, and 1.34 m/s for the weak, moderate, and strong breakers respectively. The horizontal and vertical components of the jet tip velocity, (u_{impact},v_{impact}), at the moment of jet impact are (1.38, 0.77) m/s, (1.49,

Table 3.2: The values for the regression coefficients, xp_1, xp_2, xp_3, yp_1, yp_2, and yp_3, from second order polynomials which are fitted to the $x_j(t)$ and $y_j(t)$ motion of the jet tip point. The second order polynomials have the following form; $x_j(t) = xp_1t^2 + xp_2t + xp_3$ and $y_j(t) = yp_1t^2 + yp_2t + yp_3$ for x and y motion, respectively.

Fit coefficient	Weak	Moderate	Strong
xp_1	-104	-311	-508
xp_2	-1313	-1182	-1028
xp_3	775	727	675
yp_1	-3177	-3367	-2976
yp_2	2655	2617	2223
yp_3	-506	-451	-353

0.84) m/s, and (1.52, 0.82) m/s for the weak, moderate, and strong breakers respectively. The corresponding jet impact speed, taken to be $V_{jet} = \sqrt{u_{impact}^2 + v_{impact}^2}$, monotonically increases with breaker intensity from 1.60, 1.69, 1.75 m/s for the three breakers respectively. The average wave crest speed and jet impact speeds are reported in Table 3.3.

The vertical component of the jet tip acceleration, a_y, (assuming constant acceleration) is given by the second derivative of $y_j(t)$, $\overline{a}_y = d^2(y_j(t))/dt^2 = 2yp_1$. The x component of acceleration of the jet tip is measured to be 6.5 m/s^2, 6.7 m/s^2 and 5.95 m/s^2 for the weak, moderate, and strong breakers respectively. These accelerations are about 20% lower than the constant acceleration due to gravity, $g = 9.81$ m/s^2, and could indicate the effects of surface tension or aerodynamic forces influence the motion of the jet just before impact significantly. Similarly, the horizontal component of acceleration for the jet tip is given by $\overline{a}_x = d^2(x_j(t))/dt^2 = 2xp_1$. The horizontal acceleration, a_y, for the weak, moderate and strong breakers are 0.2 m/s^2, 0.6 m/s^2, 1.0 m/s^2. The horizontal component of acceleration is found to increase with breaker intensity.

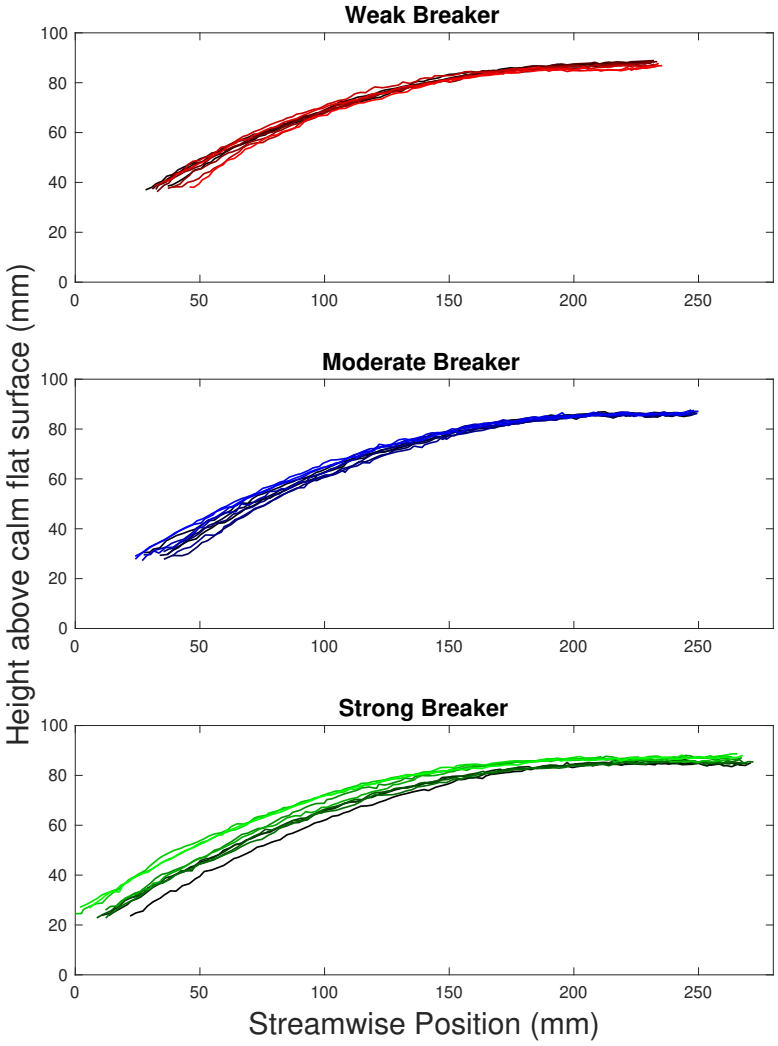

Figure 3.10: Jet tip trajectories for the three plunging breakers measured from 10 individual runs. The time interval between each measurement point is $\Delta t = 0.0015$ s (1/650 s). The wave is moving from right to left and the first point is measured just as the jet tip starts to form from the wave crest and the last point is measured when the jet impacts the free surface. The jet trajectories are not adjusted spatially or temporally, and therefore indicate the repeatability of the experiment from run to run for the three waves.

Figures 3.11, 3.12, and 3.13 (referred to as the three figures in the subsequent paragraphs) show the surface profile evolution during the active phase of wave breaking for the weak, moderate, and strong plunging breakers respectively. The surface profiles are phase averaged over 10 repeated runs of the same breaker and are adjusted spatially (in x) and temporally (in t) so that the point of jet impact occurs at the same x and t for all three breakers. The surface profiles are plotted in the reference frame of the wave crest speed as reported in Table 3.3. The gradient of color along each profile indicates the value of the standard deviation of surface height at each streamwise position over the 10 runs. Each profile is plotted 10 mm above the previous and is separated in time by Δt = 0.0123 s. Because the profiles are plotted in the reference frame of the wave crest, features that move to the left are moving faster than the wave crest speed and features moving to the right are moving slower than the wave crest speed.

Despite the fact that wave breaking is a highly non-linear process, common small-scale and large-scale features are present in the three figures. The first of these features is the motion of the leading edge of the splash region, which is initially formed by the jet impact. Moments before the formation of the splash region, the breaker profile is characterized by high variation in surface height associated with the time of jet impact, seen along surface profile (i) between $x + c * t = 50$ to 100 (mm). After jet impact, the leading edge of the splash region accelerates in all three figures and goes through cycles of accelerating and decelerating between profiles (ii) and (iv). The speed of the front splash region is close to the inital phase speed of the wave, between surface profile (iv) and (v), and eventually decelerates by the time it

reaches surface profile (vi).

Another common feature between the three waves is the sharp indent that forms between the initial jet splash-up and the upper surface of the jet, appearing just before surface profile (ii) at around $x = 50$ mm in the three figures. In images taken with the camera positioned to examine the crater in more detail, one can see this indent is actually a narrow crater that extends below the apparent free surface that closes off rapidly, ejecting a wall of drops into the air. Following the indent in time, it begins to slow down after surface profile (ii), just as the wave crest passes through the feature. Between surface profiles (iii) and (iv) the feature appears to diminish, when a violent air bubble explosion occurs just after surface profile (iv) and $x = 250$ mm. The violent bubble bursting was identified as one of the primary drop producing regions in Section 3.1.

The initial indent seems to form a boundary between the irrotational water fluid motion to the right of the indent and the vortical region on the left generated by the splash up from the jet impact. From a qualitative analysis, the jet impact and subsequent splash could generate a vortex pair, one vortex to the right of the indent and another to the left, with both vortices rotating counter clockwise. A similar vortex pair was observed just after jet impact in 2D simulations of wave breaking by Iafrati [2009], Figure 2 (d). The induced motion of the vortex pair would be in the direction of the wave crest travel and the vortex decay and diffusion could be responsible for the diminishing of the intent feature.

Similar secondary and tertiary indents form just before surface profile (iv) at $x = 70$ mm and surface profile (v) at $x = 80$ mm, respectively. The standard

Table 3.3: Table comparing physical wave parameters for the weak, moderate, and strong plunging breakers. The average phase speed of the wave $\bar{c}$ is measured just before the jet starts to form on the wave, see Figure 3.9. The average jet impact speed, $\bar{v_{jet}}$, is measured just before jet impact (see Figure 3.10) and the total number of drops indicates the number of drops produced per breaking event per crest width whose $D > 100$ μm, measured in section 3.2.2.

Plunging Breaker Type	A/λ_0	$\bar{c}$ (m/s)	$\bar{V}_{jet}$ (m/s)	# of drops
Weak	0.070	1.33 ± 0.003	1.60 ± 0.022	696
Moderate	0.074	1.33 ± 0.002	1.69 ± 0.018	860
Strong	0.076	1.36 ± 0.002	1.75 ± 0.016	1173

deviation of the free surface height is higher in these two regions, similar to the initial indent. The time difference between the formation of the primary and secondary and secondary and tertiary indents are 0.22 s and 0.15 s respectively. One possible formation mechanism for the secondary and tertiary indents could be the rebounding of the jet.

3.2.2 Drop Measurements

The spatio-temporal distribution of drops, introduced in Section 3.1 as $N(x,t)$, the number of drops moving up across the measurement plane per crest width per breaking event per unit time (Δt) per unit streamwise direction (Δx), is measured experimentally and shown in Figures 3.14, 3.15, and 3.16 for the weak, moderate, and strong plunging breakers respectively. Figures 3.14, 3.15, and 3.16 are collectively referred to as the three figures in the following paragraphs. Figure 3.14 is the same as Figure 3.3 except the color scale for the number of drops in Figure 3.14 matches that of 3.15 and 3.16.

In the three figures, there are two large spatio-temporal regions of drop pro-

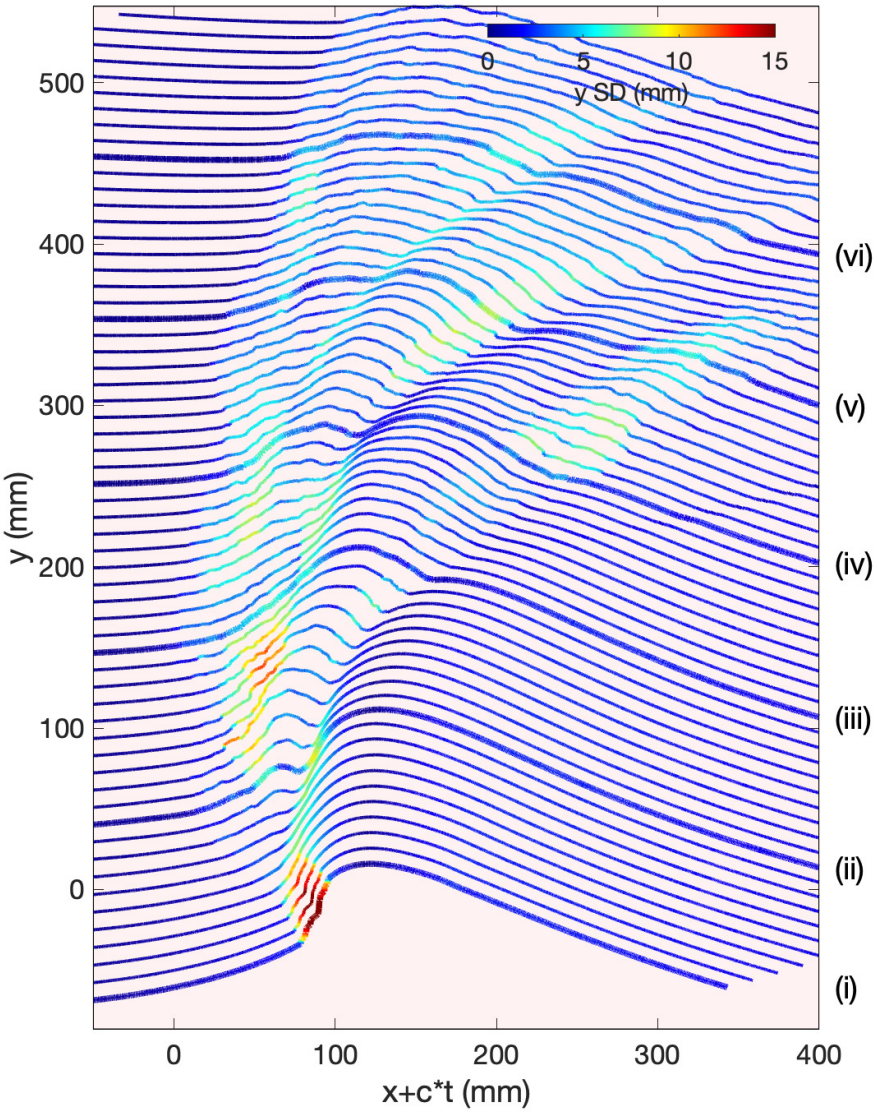

Figure 3.11: Mean surface profiles for the weak breaker ($f_0 = 1.15$ Hz, A $= 0.070\lambda_0$) averaged over 10 unique runs. The range of color along each profile indicates the standard deviation of surface height at each streamwise position over the 10 runs. Each successive profile is plotted 10 mm above the previous with a temporal separation of Δt $= 0.0123$ s between each profile, with breaker profile (i) occurring at $t = 0.0031$ s. The surface profiles are shown in a reference frame fixed to the wave crest measured before the jet is formed ($c = 1330$ mm/s).

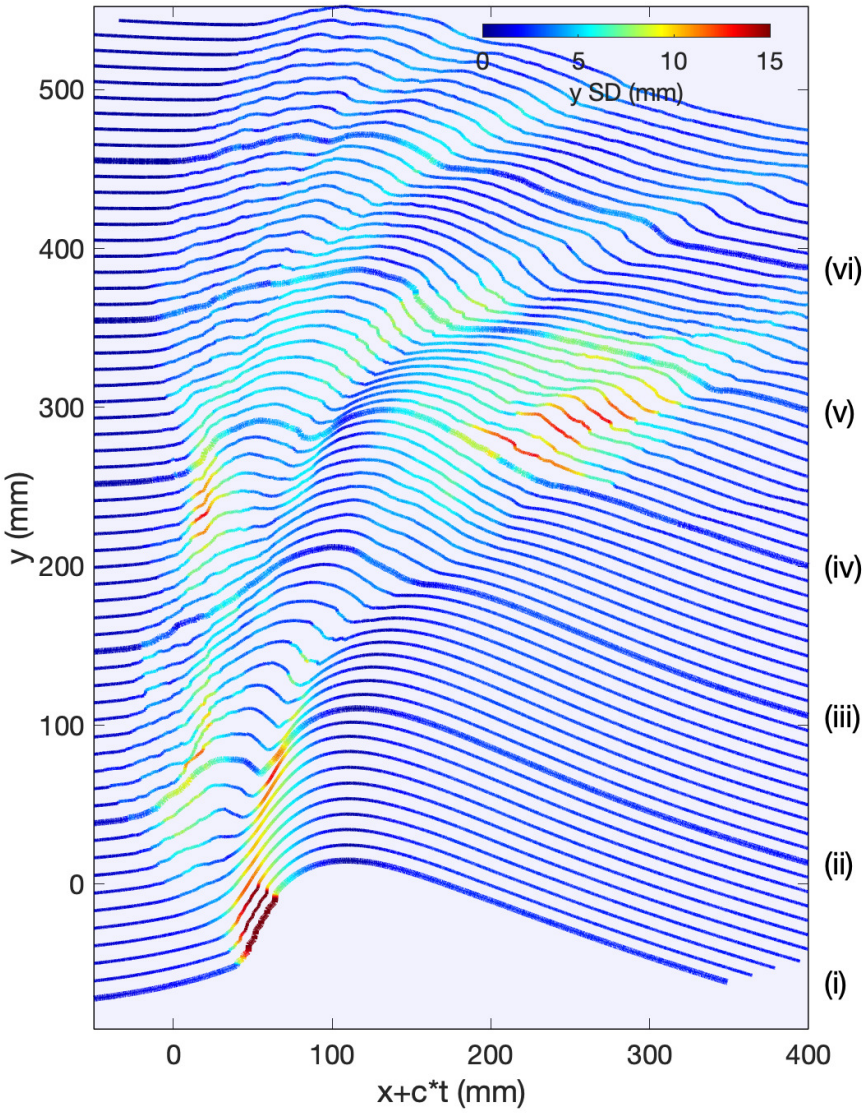

Figure 3.12: Mean surface profiles for the moderate breaker (f_0 = 1.15 Hz, A = $0.074\lambda_0$) averaged over 10 unique runs. The range of color along each profile indicates the standard deviation of surface height at each streamwise position over the 10 runs. Each successive profile is plotted 10 mm above the previous with a temporal separation of Δt = 0.0123 s between each profile, with breaker profile (i) occurring at t = 0.0031 s. The surface profiles are shown in a reference frame fixed to the wave crest measured before the jet is formed (c = 1330 mm/s).

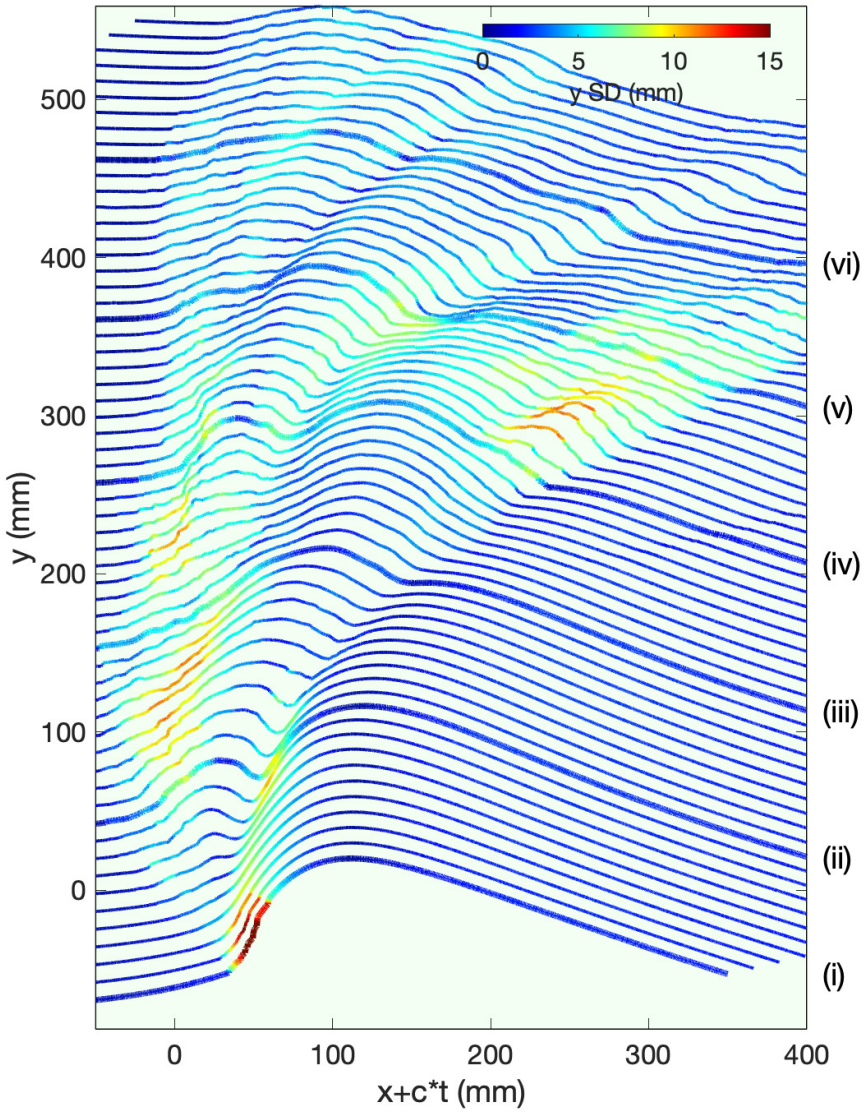

Figure 3.13: Mean surface profiles for the strong breaker ($f_0 = 1.15$ Hz, A $= 0.076\lambda_0$) averaged over 10 unique runs. The range of color along each profile indicates the standard deviation of surface height at each streamwise position over the 10 runs. Each successive profile is plotted 10 mm above the previous with a temporal separation of Δt $= 0.0123$ s between each profile, with breaker profile (i) occurring at $t = 0.0031$ s. The surface profiles are shown in a reference frame fixed to the wave crest measured before the jet is formed ($c = 1360$ mm/s).

duction measuring about 600-800 mm long and 0.6 s high. These regions were previously identified as Region I and II in Section 3.1. In region I for the weakest breaker, three prominent features, identified by a local maxima in $N(x,t)$, were identified in Section 3.1. The first of these prominent features is a local maxima around $(x,t) = (140$ mm,0.18 s) and corresponds to the approximate location and time of jet impact. The second maxima is located around $(x,t) = (325$ mm,0.275 s) and is associated with the second jet impact and splashing. Finally, the third local maxima is located at $(x,t) = (275$ mm,0.38 s) and is associated with the bursting of large air bubbles, initially entrained by the plunging jet.

In contrast, region I for the moderate breaker contains only two prominent local maxima. The first maxima is located around $(x,t) = (190$ mm,0.20 s) and is associated with the region of the indent formed by the jet impact and first splash region, between breaker profile (ii) and (iii) in Figure 3.12. Drops produced in this region are confined to a narrow spatial and temporal location. The second local maxima occurs in the vicinity of $(x,t) = (390$ mm,0.30 s) and is associated with diminishing of the impact crater and the sudden eruption of large air bubbles, just before profile (iv) in Figure 3.12.

Similarly, the spatio-temporal distribution of N in region I for the strong breaker has two pronounced local maxima at similar spatial and temporal locations. The first local maxima is located at $(x,t) = (200$ mm,0.30 s) and is associated with the location of the indent formed by the jet impact and front splash region, between breaker profile (iii) and (iv) in Figure 3.13. The second local maxima is located at $(x,t) = (420$ mm,0.40 s) is associated with large bubble bursting event, seen just

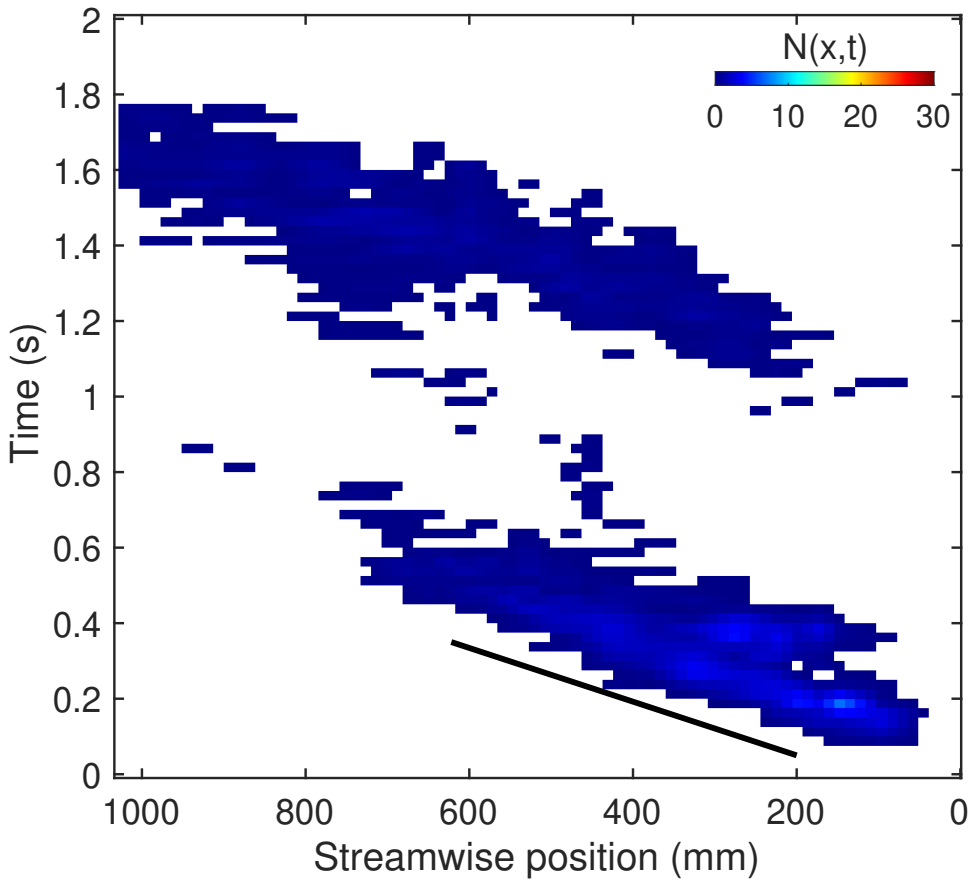

Figure 3.14: Contours of $N(x,t)$, the number of drops with $d \geq 100$ μm generated per breaking event, per $\Delta t = 0.025$ s, per $\Delta x = 13.02$ mm, per crest length, plotted on an x-t plane for the **weak breaker**. The black line is drawn with a slope of 1.7 m/s, indicating the drop ejection front. This plot is identical to Figure 3.2 except that it is plotted using the same colorbar as Figures 3.15 and 3.16.

after breaker profile (iv) in Figure 3.13. The second local maxima in region I for the weak breaker (Figure 3.14), identified as the region of the second jet impact and splashing, is no longer noticeable in the plots of $N(x,t)$ for the moderate, and strong breakers.

Similar to the analysis carried out in Section 3.1, the measured function $N(x,t)$ was spatially and temporally integrated separately over all x and t to obtain number of droplets generated per unit time per unit crest length, $N_x(t)$, and the number of

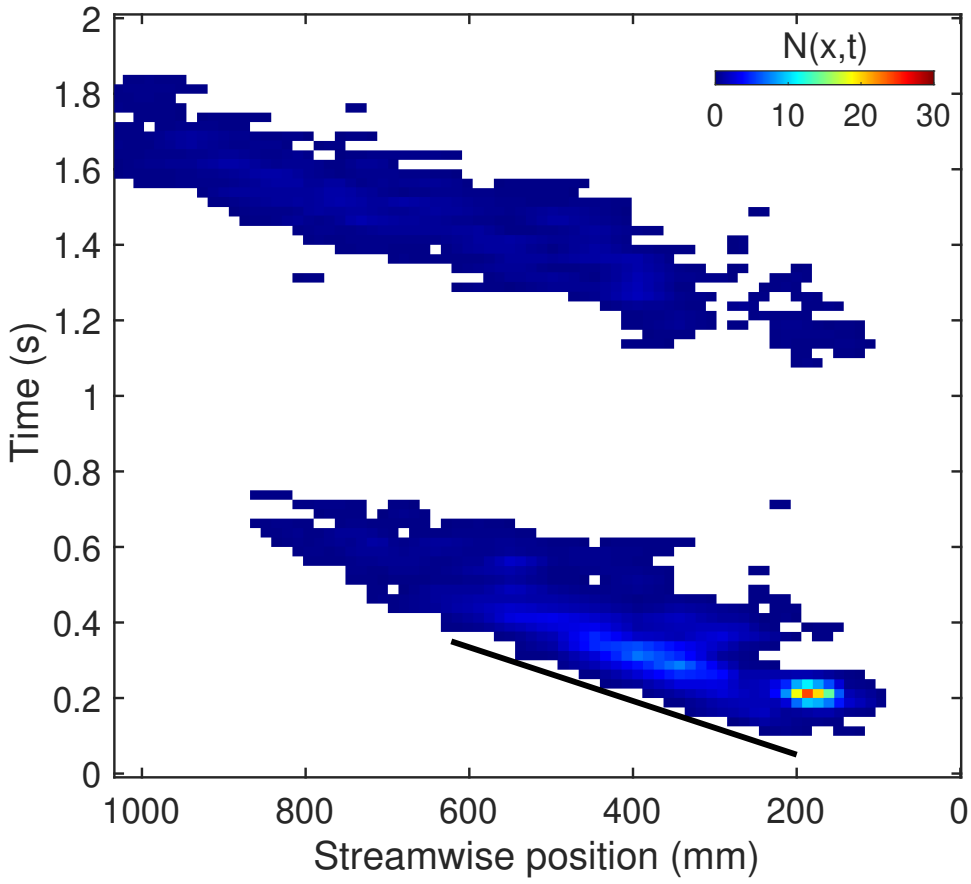

Figure 3.15: Contours of $N(x,t)$, the number of drops with $d \geq 100$ μm generated per breaking event, per $\Delta t = 0.025$ s, per $\Delta x = 13.02$ mm, per crest length, plotted on an x-t plane for the **moderate breaker**. The black line is drawn with a slope of 1.7 m/s, indicating the drop ejection front.

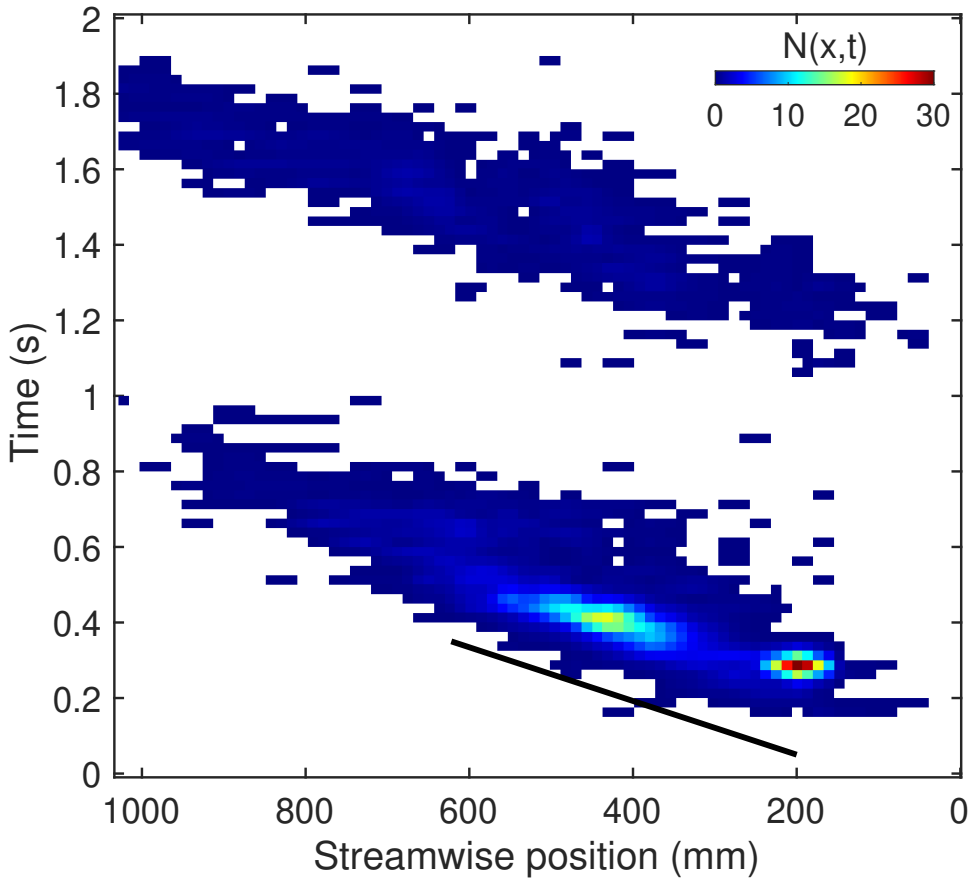

Figure 3.16: Contours of $N(x,t)$, the number of drops with $d \geq 100$ μm generated per breaking event, per $\Delta t = 0.025$ s, per $\Delta x = 13.02$ mm, per crest length, plotted on an x-t plane for the **strong breaker**. The black line is drawn with a slope of 1.7 m/s, indicating the drop ejection front.

droplets generated per unit x per unit crest length, $N_t(x)$, respectively. A plot of $N_x(t)$ for the weak, moderate, and strong breakers is presented in Figure 3.17. The three functions share similar features and local maxima, found at approximately $t = 0.20$, 0.40, and 1.50 s after initial jet impact. The first local maxima occurs between $t = 0.15$ and 0.30 s and was previously identified as the approximate time of jet impact. Comparing the maximum value of the first peak between the weak and moderate and the weak and strong breakers, it was found that the first peak is about 2.5 times larger for the moderate and 3.7 times larger for the strong breaker. The number of drops measured during the jet impact phase is shown in Table 3.4 and accounts for 14%, 19%, and 23% of the total number of drops produced in the weak, moderate, and strong breakers.

Shortly after the first peak, a second local maxima, associated with the large bubble popping region, occurs between $t = 0.30$ and 0.40 s. The number of drops measured during the large bubble bursting phase is 356, 456, 735 accounting for 52%, 53%, and 62% of the total number of drops produced between the weak, moderate, and strong breakers, respectively. The total number and proportion of drops generated in region I increases with breaker intensity.

For the weak breaker, the second local maxima is slightly larger, measuring at $N_x(0.175) = 1374$ for the first peak and $N_x(0.375) = 1812$ for the second peak. However, in the case of the moderate and strong breakers the first peak is more intense than the second peak. The third and final local maxima is associated with small bubbles rising to the free surface and popping, from about $t = 1$ to 2 seconds. The temporal range and maximum peak of the third local maxima is similar between

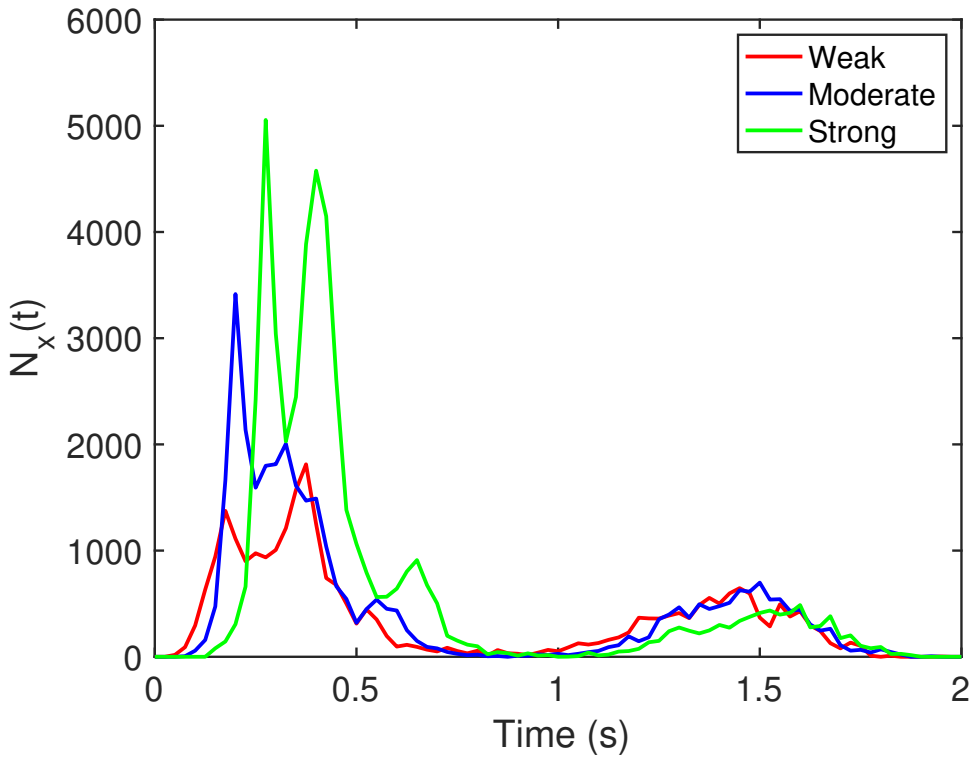

Figure 3.17: A comparison of the number of drops generated per time interval per crest length vs. time, $N_x(t)$ for the weak (in red), moderate (in blue), and strong breaker (in green). Three pronounced peaks are present in the curves from all three waves. The first associated with jet impact, the second with the large bubble popping region and the third with the smaller bubbles coming to the free surface later in time. The three curves were generated by spatially integrating the data in Figures 3.14, 3.15, and 3.16.

the three breakers.

Figure 3.18 shows a plot of $N_t(x)$, the number of drops generated per unit x per unit crest length, for the three breakers. Each data point (circle, triangle, or square) indicates the center location of a drop measurement window. The curve for the weak breaker (red circles) has a simple structure with a single local maxima at about $x = 200$ mm, which approximately corresponds to the jet impact location. Local features and maxima emerge in the curves of the moderate and strong breakers, becoming more pronounced with wave intensity. The first local maxima in the

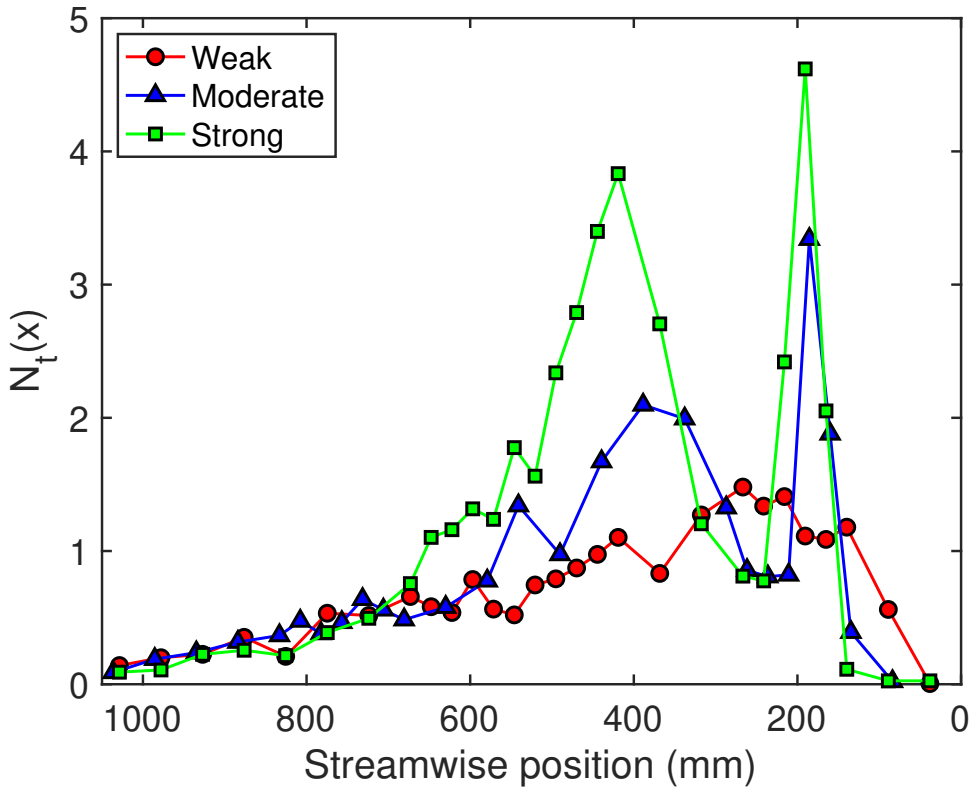

Figure 3.18: A comparison of the number of drops generated per mm in the streamwise direction per crest length vs. streamwise position, $N_t(x)$, for the weak (red circles), moderate (blue triangles), and strong breakers (green squares). The weak breaker has a simple spatial distribution of drops that increases at the jet impact location and gradually decreases. In contrast, the moderate and strong breakers have pronounced peaks and features at the locations of jet impact and large bubble popping. These three curves were generated by temporally integrating $N(x,t)$, shown in Figures 3.14, 3.15, and 3.16.

moderate and strong breakers occurs at $x = 200$ mm and is associated with the approximate location of jet impact. A second local maxima is present at $x = 400$ mm for the moderate and $x = 450$ mm for the strong breaker associated with the large bubble bursting event.

Table 3.4 compares the number of drops measured per breaking event per unit crest length for the three breakers during the different stages of breaking. The total number of measured drops over all t and x, reported in the last column, is 696,

Table 3.4: Table comparing the number drops produced per breaking event per crest width (whose $d > 100$ μm) during the different stages of breaking for the weak, moderate, and strong plunging breakers. The jet impact and large bubble bursting regions are defined spatially and temporally (see text for full description) while the late bubble bursting region is defined from $1 < t < 2$ seconds.

Region	Weak Breaker	Moderate Breaker	Strong Breaker
Jet Impact	100 (14%)	166 (19%)	265 (23%)
Large Bubble Burst	356 (52%)	456 (53%)	735 (62%)
Late Time Bubbles	240 (34%)	238 (28%)	172 (15%)
Total	696	860	1173

860, and 1173 drops for the weak, moderate, and strong breakers respectively. The number of drops generated during jet impact is also reported. The jet impact region is defined as (x, t) = (0 - 200 mm, 0.00 - 0.30 s), (x, t) = (0 - 250 mm, 0.00 - 0.30 s), and (x, t) = (0 - 250 mm, 0.00 - 0.35 s) for the weak, moderate, and strong breakers, respectively. During this phase of wave breaking the number of drops generated were 100, 166, and 265 accounting for 14%, 19%, and 23% of the total drops for the weak, moderate and strong breakers.

The drops attributed to large bubble bursting region are taken as those passing through the measurement plane before $t < 1$ s, excluding drops generated by the jet impact in the spatio-temporal region above. The number of drops generated during this phase of wave breaking are 356, 456, and 735 accounting for 52%, 53%, and 62% of the total drops generated by the three breakers. Finally, the number of drops generated in the late time bubble popping, after the active phase of wave breaking, are 240, 238, 172 drops and accounting for 34%, 28%, and 15% for the three breakers. The number of drops produced during the late time bubble popping is similar for the three breakers, although slightly lower for the stronger breaker.

A comparison of the normalized distributions of drop radii from the three breakers is shown on a log-log plot in Figure 3.19. The probability distributions were obtained in the same manner as for the distributions in Figure 3.7, see section 3.1 for details, except, in the present case, a total of 32 logarithmically spaced bins ranging from $r = 50$ to 1500 μm are used. The break in slope is calculated using the same bisection method described in section 3.1. Separate straight lines were fit, by least squares error minimization, to the smaller and larger diameter data. The slopes of the line fits for the small and large drops are represented by α and β, respectively. It should be noted that the determination of r_i and β is inherently inaccurate because there are only a few drops in each bin for the larger radii. This is a classic problem in bubble and drop measurements, and to emphasize this inadequacy, dashed lines are used to represent the fitted functions in the larger radii region of each plot. The α and β slope coefficents and r_i for the three waves are shown in Table 3.5.

For the large drops, β = -5.4 to -6.1 with no noticeable trend as the intensity of the wave increases. From Figure 3.19, it is evident that the bins containing large drop data from the weak breaker is noisy, with some bins containing only a single drop. Comparatively, the moderate and strong breaker data is progressively less noisy since more large drops are produced by these breakers; therefore, each bin is averaged over more drops. It is possible that the bimodal nature of the radius probability distribution is an artifact of the lack of bin convergence for the large drops.

The break in slope, r_i, grows as the intensity of the wave increase from $r_i =$

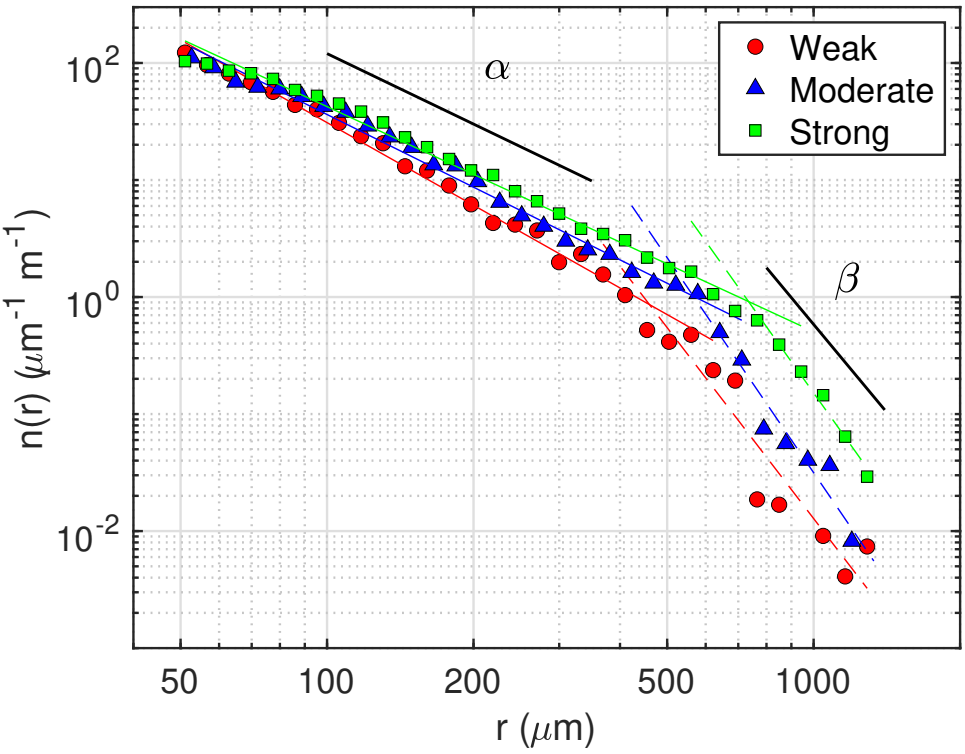

Figure 3.19: Drop probability distributions for weak (red circles), moderate (blue triangles), and strong breakers (green squares) for drops generated through out the entire breaking event $0 < t < 2$ seconds. A break in slope is identified in all three data sets and function fitting parameters and break in slope radii are shown in Table 3.5.

460 to 570 to 740 μm between the three breakers. Using the computed values of r_i, it is possible to calculate a corresponding Weber number, $We_i = v_j^2 r_i/\gamma$ where v_j is the impact speed of the jet, and $\gamma = 73$ dynes/cm. The calculated values of We are 16.1, 22.3, and 31.4 respectively. For the small drops, α decrease with wave intensity from -2.4 to -2.1 to -1.9, indicating that as breaker intensity increases, the average drop radius increases. This result is consistent with the idea and the observed trend that as more large drops are produced, the break in slope r_i would shift to the right.

Table 3.5: The fit parameters to drop size distributions from Figures 3.19 for the three waves. Where α and β are the slope of the line fits for the small and large drops respectively and r_i identifies the drop radius (in μm) where the two lines intersect.

Variable	Weak Breaker	Moderate Breaker	Strong Breaker
α	-2.4	-2.1	-1.9
β	-5.4	-6.1	-5.8
r_i (μm)	460	570	740

Chapter 4: Summary and Conclusions

Drop generation by breaking water waves is an important problem which has a significant impact on air-sea interaction. The mechanisms by which drops are generated are poorly understood. Previous studies of drop generation have mainly focused on average distributions and fluxes of drops in wind-wave tanks, wind-wave systems in the field, and more recently, numerical simulations. Though there is a qualitative understanding of how droplets are produced during a wave breaking event, there is little quantitative data to back up these assertions.

In this dissertation, the generation and dynamics of drops produced by breaking water waves were studied in laboratory-scale experiments. The breakers were generated by a programmable wavemaker using a dispersively focused wave packet technique. The wave maker motions for the three breakers differ in the values chosen for the breaking distance from the wavemaker, x_b/λ_0, and the overall wavemaker amplitude, A/λ_0. The three plunging breakers are characterized (and referred to) as weak, moderate, and strong, based on their overall wavemaker amplitude, where the weak breaker corresponds to the smallest, the moderate breaker to the middle, and strongest breaker to the largest A/λ_0.

For each of the three breakers, the breaker profile and the spatio-temporal

distribution of drops are measured using highly resolved spatial and temporal measurement techniques. The two-dimensional profile evolution at the center plane of the wave tank is measured using a laser induced fluorescence technique. Drop radii, trajectories, and the spatio-temporal distribution of drop numbers are measured using in-line holography. The two measurements are taken simultaneously at 650 frames per second. As discussed in more detail below, the measurements of the breaker profile evolution and the spatio-temporal distribution of drop generation are used to identify spray generation mechanisms during wave breaking. Also, the breaker profile measurements are used to explore the dynamics of the breaking process through examination of ensemble averaged breaker profiles for the three breakers. Finally, the number and size distribution of drops generated by the three breakers are related to the previously identified spray generation mechanism and breaker characteristics such as jet impact speed.

The evolution of breaker profiles were measured over 10 unique realizations for each of the three breakers. Using the data from these 10 runs, the mean profile and the standard deviation of the breaker profiles were computed at each instant in time. The mean breaker profiles were used to measure a set of pre-breaking geometrical parameters of the wave crest shape and plunging jet with the purpose of determining independent variables to characterize the breaker. The speed of the wave crest point, $\overline{c}$, was defined as the highest point on the wave crest profile and is measured during the formation of the plunging jet. It was found that $\overline{c}$ was nearly the same for the three waves during the jet formation phase, and was measured to be 1.33, 1.33, and 1.36 m/s for the three breakers. These values are close to the

phase speed of a linear uniform wave train with a frequency equal to the average frequency of the wave packet used to generate the breakers (f_0 = 1.15 Hz). The jet impact speed, $\overline{V}_{jet}$, was defined as the jet speed just before jet impact with the front face of the wave. The measured values of $\overline{V}_{jet}$ are 1.60, 1.69, and 1.75 m/s for the three breakers, where $\overline{V}_{jet}$ increases with breaker strength. The difference in average jet impact speed between the weak and strong plunging breakers is 9.3% while the difference in maximum wave crest height, y_{max}, is 15% (y_{max} = 26.5 mm for the weak and 30.5 mm for the strong breaker).

When the breaker profiles are aligned horizontally relative to their streamwise jet impact locations and averaged over 10 realization, the mean breaker profiles produce many common surface features between the three breakers. Despite the fact that wave breaking is a highly non-linear event, large-scale and small-scale breaker features are preserved between the three breakers. These common features take the form of ripples with rounded crests and sharp troughs that slow down and, in the reference frame of the breaking crest, propagate over the crest of the wave. The first of these features to appear is a sharp trough, or indent, formed between the initial jet splash-up and the upper surface of the plunging jet and referred to herein as the impact crater. The impact crater slows down relative to the wave crest speed and diminishes in time; eventually, a large bubble bursting event, takes place just upstream of the impact crater. The standard deviation of surface profile height is higher in the region of the large bubble bursting event and increases with breaker intensity.

The results of the spatio-temporal distribution of drops indicate that for me-

chanically generated plunging breakers, drop generation occurs in two regions of space and time. The first region (I) is associated with the active phase of wave breaking and begins with the plunging jet impact. In this region, drops are generated by the jet impact and splashing events, and by the bursting of the large air bubbles that are entrained during the initial jet impact. The second region (II) is separated from region (I) and occurs after the active phase of wave breaking following jet impact. In this region, drops are generated by small air bubbles, initially entrained by the plunging breaker, which rise to the free surface and burst.

Breaker intensity is related to drop production from the two breaking regions identified in the previous paragraph as regions (I) and (II) and their associated sub-processes. In region (I), drops are produced by two sub-processes, jet impact and large bubble bursting and splashing. During these two sub-processes, the average number of drops increases with breaker intensity and range from 100 in the weak breaker to 265 in the strong breaker for jet impact and 456 for the weak breaker to 735 for the large breaker drops for the large bubble bursting. In region (II) the number of drops measured per breaking event decreases from 240 for the weak breaker 172 for the strong breaker. When plotted on a semi-log plot, the total number of drops generated during wave breaking and the number of drops generated by jet impact is found to scale exponentially with jet impact speed.

The drop radius probability distribution is reported for each the three breakers. When plotted on a log-log plot, the small and large radius data is found to follow separate inverse power law scalings, with power law exponents represented by α and β, respectively. The small drop scaling exponent is found to decrease with wave

intensity from -2.4 for the weak to -1.9 for the strong breaker. The large drop power law exponent, β, does not follow a trend with increasing breaker intensity. It should be noted that determination of β is inherently inaccurate because there are few drops in each radius bin at larger radii. The break in slope, r_i is determined by the intersection point of the two straight lines fits by an iterative bisection method. As breaker intensity increases, r_i increases monotonically from 460 μm for the weak breaker to 740 μm for the strong breaker. The increase in r_i indicates that more large drops are produced as breaker intensity increases. Drop radii distributions with two linear regions have been previously found in natural wind-wave system (at $U_{10m} \approx 10$ m/s) by Wu et al. [1984] and in laboratory wind-wave experiments (at $U_{10m} > 30$ m/s) by Veron et al. [2012].

4.1 Future Directions

In future work, the effects of wavelength, surfactants, and wind on droplet characteristics and breaking sub-processes can be studied in a set of experiments similar to the ones presented in this dissertation. Studying the effects of wavelength on drop generation can aid in the development of scaling laws that extend the results presented in this dissertation. Particularly, parameterizing droplet production to wavelength may be of practical interest since the wavelength is an easier wave characteristic to measure in the field than jet impact speed or volume of air entrained.

Surfactants are ubiquitous on natural water surfaces and their concentration

and properties vary broadly. Previously, the effects of surfactants on drops produced by bursting bubbles has been studied in laboratory scale experiments where the droplet size distribution was found to shift to smaller sizes when compared to the clean water case [Sellegri et al., 2006] (see Chapter 1). However, the effects of surfactants on drop production by plunging breaking waves has not been related to the breaking sub-processes identified in this dissertation.

Finally, it would be desirable to study how low to moderate wind speed conditions influence drop generation and transport. This problem is of particular interest since wind is often present in the field and is one of the primary mechanisms by which water waves are generated. Studying how wind modifies the spatio-temporal distribution of drops for a range of wind speeds would lead to a better understating of how droplets are transported into the marine atmospheric boundary layer, which would lead to improved parameterization of air-sea fluxes.

Bibliography

Edgar L Andreas. Thermal and size evolution of sea spray droplets. Technical report, Cold Regions Research and Engineering Lab Hanover NH, 1989.

Fabrice Veron. Ocean spray. *Annual Review of Fluid Mechanics*, 47(1):507–538, 2015. doi: 10.1146/annurev-fluid-010814-014651.

Jin Wu. Spray in the atmospheric surface layer: Laboratory study. *Journal of Geophysical Research (1896-1977)*, 78(3):511–519, 1973. doi: 10.1029/JC078i003p00511. URL `https://agupubs.onlinelibrary.wiley.com/doi/abs/10.1029/JC078i003p00511`.

Jin Wu, John J. Murray, and Ronald J. Lai. Production and distributions of sea spray. *Journal of Geophysical Research: Oceans*, 89(C5):8163–8169, 1984. doi: 10.1029/JC089iC05p08163.

F. Veron, C. Hopkins, E. L. Harrison, and J. A. Mueller. Sea spray spume droplet production in high wind speeds. *Geophysical Research Letters*, 39(16):L16602, 2012. doi: 10.1029/2012GL052603.

Chris Fairall, Jeffrey Kepert, and Greg Holland. The effect of sea spray on surface energy transports over the ocean. *The Global Atmosphere and Ocean System*, 2: 121–142, 01 1995.

James A. Mueller and Fabrice Veron. A sea state–dependent spume generation function. *Journal of Physical Oceanography*, 39(9):2363–2372, 2009. doi: 10.1175/2009JPO4113.1.

Zhaoyuan Wang, Jianming Yang, and Frederick Stern. High-fidelity simulations of bubble, droplet and spray formation in breaking waves. *Journal of Fluid Mechanics*, 792:307–327, 2016. doi: 10.1017/jfm.2016.87.

L. Deike, W. K. Melville, and S. Popinet. Air entrainment and bubble statistics in breaking waves. *Journal of Fluid Mechanics*, 801:91–129, 2016. doi: 10.1017/jfm.2016.372.

S. Tang, Z. Yang, C. Liu, Y. Dong, and L. Shen. Numerical study on the generation and transport of spume droplets in wind over breaking waves. *Atmosphere*, 8(12): 248, 2017.

M. A. Erinin, S. D. Wang, R. Liu, D. Towle, X. Liu, and J. H. Duncan. Spray generation by a plunging breaker. *Geophysical Research Letters*, 46(14):8244–8251, 2019. doi: 10.1029/2019GL082831. URL `https://agupubs.onlinelibrary.wiley.com/doi/abs/10.1029/2019GL082831`.

M. Brocchini and D.H. Peregrine. The dynamics of strong turbulence at free surfaces. part 1. description. *Journal of Fluid Mechanics*, 449(1):225–254, 2001.

Nathan J. Washuta. *Air Entrainment in the Turbulent Ship Hull Boundary Layer*. PhD thesis, University of Maryland College Park, 2016.

Naeem Masnadi, Martin A Erinin, Nathan Washuta, Farshad Nasiri, Elias Balaras, and James H Duncan. Air entrainment and surface fluctuations in a turbulent ship hull boundary layer. *Journal of Ship Research*, 2019.

C. D. O'Dowd and G. de Leeuw. Marine aerosol production: a review of the current knowledge. *Philosophical Transactions of the Royal Society A: Mathematical, Physical and Engineering Sciences*, 365(1856):1753–1774, 2007.

E. L. Andreas. Fallacies of the enthalpy transfer coefficient over the ocean in high winds. *Journal of the Atmospheric Sciences*, 68(7):1435–1445, 2011. doi: 10.1175/2011JAS3714.1.

J.-W. Bao, C. W. Fairall, S. A. Michelson, and L. Bianco. Parameterizations of sea-spray impact on the air–sea momentum and heat fluxes. *Monthly Weather Review*, 139(12):3781–3797, 2011. doi: 10.1175/MWR-D-11-00007.1.

L. Bianco, J.-W. Bao, C. W. Fairall, and S. A. Michelson. Impact of sea-spray on the atmospheric surface layer. *Boundary-Layer Meteorology*, 140(3):361, 5 2011. doi: 10.1007/s10546-011-9617-1.

J. A. Mueller and F. Veron. Impact of Sea Spray on Air-Sea Fluxes. Part I: Results. *Journal Of Physical Oceanography*, 44(11):2817–2834, November 2014a.

J. A. Mueller and F. Veron. Impact of Sea Spray on Air-Sea Fluxes. Part II: Feedback Effects. *Journal Of Physical Oceanography*, 44(11):2835–2853, November 2014b.

Magdalena Anguelova, Richard P. Barber, and Jin Wu. Spume drops produced by the wind tearing of wave crests. *Journal of Physical Oceanography*, 29(6):1156–1165, 1999a. doi: 10.1175/1520-0485(1999)029⟨1156:SDPBTW⟩2.0.CO;2.

Momoki Koga. Direct production of droplets from breaking wind-waves — its observation by a multi-colored overlapping exposure photographing technique. *Tellus*, 33(6):552–563, 1981. doi: 10.1111/j.2153-3490.1981.tb01781.x.

Edgar L. Andreas and Kerry A. Emanuel. Effects of sea spray on tropical cyclone intensity. *Journal of the Atmospheric Sciences*, 58(24):3741–3751, 2001. doi: 10.1175/1520-0469(2001)058⟨3741:EOSSOT⟩2.0.CO;2.

Y. Q. Wang, J. D. Kepert, and G. J. Holland. The effect of sea spray evaporation on tropical cyclone boundary layer structure and intensity. *Monthly Weather Review*, 129(10):2481–2500, 2001.

D. C. Blanchard and L. D. Syzdek. Concentration of bacteria in jet drops from bursting bubbles. *Journal of Geophysical Research*, 77(27):5087–5099, 1972.

A. R. Ravishankara. Heterogeneous and multiphase chemistry in the troposphere. *Science*, 276(5315):1058–1065, 1997.

G. de Leeuw, E. L. Andreas, M. D. Anguelova, C. W. Fairall, E. R. Lewis, C. O'Dowd, M. Schulz, and S. E. Schwartz. Production flux of sea spray aerosol. *Reviews of Geophysics*, 49(2), 2011. doi: 10.1029/2010RG000349.

E. C. Monahan, D. E. Spiel, and K. L. Davidson. A model of marine aerosol generation via whitecaps and wave disruption. In *Oceanic Whitecaps*, pages 167–174. Springer, 1986.

G. de Leeuw. Vertical profiles of giant particles close above the sea surface. *Tellus B*, 38(1):51–61, 1986. doi: 10.3402/tellusb.v38i1.15070.

M. H. Smith, P. M. Park, and I. E. Consterdine. Marine aerosol concentrations and estimated fluxes over the sea. *Quarterly Journal of the Royal Meteorological Society*, 119(512):809–824, 1993. doi: 10.1002/qj.49711951211.

J. S. Reid, H. H. Jonsson, M. H. Smith, and A. Smirnov. Evolution of the vertical profile and flux of large sea-salt particles in a coastal zone. *Journal of Geophysical Research: Atmospheres*, 106(D11):12039–12053, 2001. doi: 10.1029/2000JD900848.

E. L. Andreas. A new sea spray generation function for wind speeds up to 32 m s^{-1}. *Journal of Physical Oceanography*, 28(11):2175–2184, 1998. doi: 10.1175/1520-0485(1998)028⟨2175:ANSSGF⟩2.0.CO;2.

C. F. Kientzler, A. B. Arons, D. C. Blanchard, and A. H. Woodcock. Photographic investigation of the projection of droplets by bubbles bursting at a water surface. *Tellus*, 6(1):1–7, 1954. doi: 10.1111/j.2153-3490.1954.tb01085.x.

D. E. Spiel. On the births of jet drops from bubbles bursting on water surfaces. *Journal of Geophysical Research*, 100(C3):4995–5006, 1995. doi: 10.1029/94JC03055.

D. E. Spiel. On the births of film drops from bubbles bursting on seawater surfaces. *Journal of Geophysical Research-Oceans*, 103(C11):24907–24918, 1998. doi: 10.1029/98JC02233.

F. Resch. Oceanic air bubbles as generators of marine aerosols. In *Oceanic Whitecaps*, pages 101–112. Springer, 1986. doi: 10.1007/978-94-009-4668-2_10.

F. Resch and G. Afeti. Film drop distributions from bubbles bursting in seawater. *Journal of Geophysical Research: Oceans*, 96(C6):10681–10688, 1991. doi: 10.1029/91JC00433.

R. J. Cipriano and D. C. Blanchard. Bubble and aerosol spectra produced by a laboratory 'breaking wave'. *Journal of Geophysical Research: Oceans*, 86(C9): 8085–8092, 1981. doi: 10.1029/JC086iC09p08085.

A. M. Gañán Calvo. Revision of bubble bursting: universal scaling laws of top jet drop size and speed. *Physical Review Letters*, 119:204502, 2017. doi: 10.1103/PhysRevLett.119.204502.

L. Deike, E. Ghabache, G. Liger-Belair, A. K. Das, S. Zaleski, S. Popinet, and T. Séon. Dynamics of jets produced by bursting bubbles. *Physical Review Fluids*, 3:013603, 2018. doi: 10.1103/PhysRevFluids.3.013603.

C. F. Brasz, C. T. Bartlett, P. L. L. Walls, E. G. Flynn, Y. E. Yu, and J. C. Bird. Minimum size for the top jet drop from a bursting bubble. *Physical Review Fluids*, 3:074001, 2018. doi: 10.1103/PhysRevFluids.3.074001.

K. Sellegri, C. D. O'Dowd, Y. J. Yoon, S. G. Jennings, and G. de Leeuw. Surfactants and submicron sea spray generation. *Journal of Geophysical Research: Atmospheres*, 111(D22), 2006.

R. L. Modini, L. M. Russell, G. B. Deane, and M. D. Stokes. Effect of soluble surfactant on bubble persistence and bubble-produced aerosol particles. *Journal of Geophysical Research: Atmospheres*, 118(3):1388–1400, 2013.

A. H. Callaghan, M. D. Stokes, and G. B. Deane. The effect of water temperature on air entrainment, bubble plumes, and surface foam in a laboratory breaking-wave analog. *Journal of Geophysical Research: Oceans*, 119(11):7463–7482, 2014.

E. Lamarre and W. K. Melville. Air entrainment and dissipation in breaking waves. *Nature*, 351(6326):469, 1991. doi: 10.1038/351469a0.

G. B. Deane and M. D. Stokes. Scale dependence of bubble creation mechanisms in breaking waves. *Nature*, 418(6900):839, 2002. doi: 10.1038/nature00967.

P. Lubin and S. Glockner. Numerical simulations of three-dimensional plunging breaking waves: generation and evolution of aerated vortex filaments. *Journal of Fluid Mechanics*, 767:364–393, 2015. doi: 10.1017/jfm.2015.62.

X. Liu and J. H. Duncan. The effects of surfactants on spilling breaking waves. *Nature*, 421(6922):520–523, 2003.

X. Liu and J. H. Duncan. An experimental study of surfactant effects on spilling breakers. *Journal of Fluid Mechanics*, 567:433–455, 2006.

X. Liu. A laboratory study of spilling breakers in the presence of light-wind and surfactants. *Journal of Geophysical Research: Oceans*, 121(3):1846–1865, 2016.

J. Wu. On parameterization of sea spray. *Journal of Geophysical Research: Oceans*, 95(C10):18269–18279, 1990. doi: 10.1029/JC095iC10p18269.

E. L. Andreas. Sea spray and the turbulent air-sea heat fluxes. *Journal of Geophysical Research: Oceans*, 97(C7):11429–11441, 1992. doi: 10.1029/92JC00876.

E. L. Andreas, J. B. Edson, E. C. Monahan, M. P. Rouault, and S. D. Smith. The spray contribution to net evaporation from the sea: A review of recent progress. *Boundary-Layer Meteorology*, 72(1-2):3–52, 1995. doi: 10.1007/BF00712389.

R. J. Lai and O. H. Shemdin. Laboratory study of the generation of spray over water. *Journal of Geophysical Research*, 79(21):3055–3063, 1974. doi: 10.1029/JC079i021p03055.

E. C. Monahan, K. L. Davidson, and D. E. Spiel. Whitecap aerosol productivity deduced from simulation tank measurements. *Journal of Geophysical Research: Oceans*, 87(C11):8898–8904, 1982. doi: 10.1029/JC087iC11p08898.

E. C. Monahan, C. W. Fairall, K. L. Davidson, and P. J. Boyle. Observed interrelations between 10m winds, ocean whitecaps and marine aerosols. *Quarterly Journal of the Royal Meteorological Society*, 109(460):379–392, 1983.

M. Koga. Dispersal of droplets over breaking wind waves under the direct action of wind. *Journal of the Oceanographical Society of Japan*, 40(1):29–38, 1984. doi: 10.1007/BF02071206.

M. Anguelova, R. P. Barber, and J. Wu. Spume drops produced by the wind tearing of wave crests. *Journal of Physical Oceanography*, 29(6):1156–1165, 1999b. doi: 10.1175/1520-0485(1999)029⟨1156:SDPBTW⟩2.0.CO;2.

C. W. Fairall, M. L. Banner, W. L. Peirson, W. Asher, and R. P. Morison. Investigation of the physical scaling of sea spray spume droplet production. *Journal of Geophysical Research: Oceans*, 114(C10), 2009. doi: 10.1029/2008JC004918.

M. D. Stokes, G. B. Deane, K. Prather, T. H. Bertram, M. J. Ruppel, O. S. Ryder, J. M. Brady, and D. Zhao. A marine aerosol reference tank system as a breaking wave analogue for the production of foam and sea-spray aerosols. *Atmospheric Measurement Techniques*, 6(4):1085–1094, 2013. doi: 10.5194/amt-6-1085-2013.

S. J. Norris, I. M. Brooks, B. I. Moat, M. J. Yelland, G. De Leeuw, R. W. Pascal, and B Brooks. Near-surface measurements of sea spray aerosol production over whitecaps in the open ocean. *Ocean Science*, 9(1):133–145, 2013. doi: 10.5194/os-9-133-2013.

Sophie Dan Wang. Laboratory measurements of spray droplets generated by breaking water waves. Master's thesis, University of Maryland College Park, 2012.

J. H. Duncan, H. Qiao, V. Philomin, and A. Wenz. Gentle spilling breakers: crest profile evolution. *Journal of Fluid Mechanics*, 379:191–222, 1999.

An Wang, Christine M. Ikeda-Gilbert, James H. Duncan, Daniel P. Lathrop, Mark J. Cooker, and Anne M. Fullerton. The impact of a deep-water plunging breaker on a wall with its bottom edge close to the mean water surface. *Journal of Fluid Mechanics*, 843:680–721, 2018. doi: 10.1017/jfm.2018.109.

R. J. Rapp and W. K. Melville. Laboratory measurements of deep-water breaking waves. *Philosophical Transactions of the Royal Society of London A: Mathematical, Physical and Engineering Sciences*, 331(1622):735–800, 1990. doi: 10.1098/rsta.1990.0098.

M. S. Longuet-Higgins. Breaking waves in deep or shallow water. *Proc. 10th Symp. on Naval Hydrodynamics*, pages 597–605, 1976.

Joseph Katz and Jian Sheng. Applications of holography in fluid mechanics and particle dynamics. *Annual Review of Fluid Mechanics*, 42(1):531–555, 2010. doi: 10.1146/annurev-fluid-121108-145508.

Daniel R. Guildenbecher, Jian Gao, Phillip L. Reu, and Jun Chen. Digital holography simulations and experiments to quantify the accuracy of 3d particle location and 2d sizing using a proposed hybrid method. *Appl. Opt.*, 52(16):3790–3801, 6 2013. doi: 10.1364/AO.52.003790.

John C. Crocker and David G. Grier. Methods of digital video microscopy for colloidal studies. *Journal of Colloid and Interface Science*, 179(1):298 – 310, 1996. ISSN 0021-9797. doi: https://doi.org/10.1006/jcis.1996.0217. URL `http://www.sciencedirect.com/science/article/pii/S0021979796902179`.

An Wang. *On the Impact Between a Water Free Surface and a Rigid Structure*. PhD thesis, University of Maryland College Park, 2017.

Nian-Sheng Cheng. Comparison of formulas for drag coefficient and settling velocity of spherical particles. *Powder Technology*, 189(3):395 – 398, 2009. ISSN 0032-5910. doi: 10.1016/j.powtec.2008.07.006.

J.D. Klett H.R. Pruppacher. *Microphysics of Clouds and Precipitation*. Springer, 1978.

J. O. Hinze. Fundamentals of the Hydrodynamic Mechanism of Splitting in Dispersion Processes. *Aiche Journal*, 1(3):289–295, 1955. doi: 10.1002/aic.690010303.

A. Iafrati. Numerical study of the effects of the breaking intensity on wave breaking flows. *Journal of Fluid Mechanics*, 622:371–411, 2009. doi: 10.1017/S0022112008005302.

F Stern, WS Hwang, and SY Jaw. Effects of Waves on the Boundary Layer of a Surface-Piercing Flat Plate: Experiment and Theory. *Journal of Ship Research*, 33(1):63–80, MAR 1989. ISSN 0022-4502.

J Longo, HP Huang, and F Stern. Solid/free-surface juncture boundary layer and wake. *Experiments in Fluids*, 25(4):283–297, SEP 1998. ISSN 0723-4864. doi: {10.1007/s003480050232}.

M Sreedhar and F Stern. Prediction of solid/free-surface juncture boundary layer and wake of a surface-piercing flat plate at low Froude number. *Journal of Fluids Engineering*, 120(2):354–362, JUN 1998. ISSN 0098-2202. doi: {10.1115/1.2820655}.

F Stern, JE Choi, and WS Hwang. Effects of Waves on the Wake of a Surface-Piercing Flat Plate: Experiment and Theory. *Journal of Ship Research*, 37(2): 102–118, JUN 1993. ISSN 0022-4502.

P. M. Carrica, D. Drew, F. Bonetto, and R. T. Lahey. A polydisperse model for bubbly two-phase flow around surface ship. *International Journal of Multiphase Flow*, 25(2):257–305, 1999. doi: 10.1016/S0301-9322(98)00047-0.

F. J. Moraga, P. M. Carrica, D. A. Drew, and R. T. Lahey. A sub-grid air entrainment model for breaking bow waves and naval surface ships. *Computers and Fluids*, 37(3):281–298, 2008. doi: 10.1016/j.compfluid.2007.06.003.

Matias Perret and Pablo M. Carrica. Bubble-wall interaction and two-phase flow parameters on a full-scale boat boundary layer. *International Journal of Multiphase Flow*, 73:289–308, 2015. doi: 10.1016/j.ijmultiphaseflow.2015.03.013.

Alejandro M. Castro, Jiajia Li, and Pablo M. Carrica. A mechanistic model of bubble entrainment in turbulent free surface flows. *International Journal of Multiphase Flow*, 86:33–55, 2016. doi: 10.1016/j.ijmultiphaseflow.2016.07.005.

J. Li, A. M. Castro, and P. M. Carrica. Progress on Prediction of Bubbly Flows Around Ships. In *Volume 1B, Symposia: Fluid Mechanics*, number V01BT30A001, page 7665, July 2016.

R. R. Dong, J. Katz, and T. T. Huang. On the structure of bow waves on a ship model. *J. Fluid Mech.*, 346:77 – 115, 1997.

T. A. Waniewski, C. E. Brennen, and F. Raichlen. Measurements of air entrainment by bow waves. *J. Fluids Eng.*, 123:57 – 63, 2001.

T. A. Waniewski, C. E. Brennen, and F. Raichlen. Bow wave dynamics. *J. Ship Res.*, 46:1 – 15, 2002.

L Shen and DKP Yue. Large-eddy simulation of free-surface turbulence. *Journal of Fluid Mechanics*, 440:75–116, AUG 10 2001. ISSN 0022-1120.

Xin Guo and Lian Shen. On the generation and maintenance of waves and turbulence in simulations of free-surface turbulence. *Journal of Computational Physics*, 228 (19):7313–7332, OCT 20 2009. ISSN 0021-9991. doi: {10.1016/j.jcp.2009.06.030}.

D. Kim, A. Mani, and P. Moin. Numerical simulation of bubble formation by breaking waves in turbulent two-phase couette flow. *CTR Ann. Res. Brief*, pages 37–46, 2013.

H. Schlichting. *Boundary-Layer Theory*. McGraw-Hill Book Company, 7 edition, 1979.

P Spalart. Direct simulation of a turbulent boundary layer up to $Re_\theta = 1410$. *Journal of Fluid Mechanics*, 187:61–98, 1988.

N. Washuta, N. Masnadi, and J. H. Duncan. Near-surface boundary layer turbulence along a horizontally-moving, surface-piercing vertical wall. In *31st Symposium on Naval Hydrodynamics*, 2016.

P. C. Duineveld. The rise velocity and shape of bubbles in pure water at high reynolds number. *Journal of Fluid Mechanics*, 292:325 – 332, 1995.